UC Berkeley
UC Berkeley Electronic Theses and Dissertations

Title
All Inkjet-Printed SnO2/ZrO2 Transistors

Permalink
https://escholarship.org/uc/item/4rk7w7m7

Author
Jang, Jaewon

Publication Date
2013

Peer reviewed|Thesis/dissertation

All Inkjet-Printed SnO_2/ZrO_2 Transistors

by

Jaewon Jang

A dissertation submitted in partial satisfaction of the

requirements for the degree of

Doctor of Philosophy

in

Engineering - Electrical Engineering and Computer Sciences

in the

Graduate Division

of the

University of California, Berkeley

Committee in charge:

Professor Vivek Subramanian, Chair

Professor Tsu-Jae King Liu

Professor John Clarke

Fall 2013

Abstract

All Inkjet-Printed SnO_2/ZrO_2 Transistors

by

Jaewon Jang

Doctor of Philosophy in Engineering - Electrical Engineering and Computer Sciences

University of California, Berkeley

Professor Vivek Subramanian, Chair

Transparent electronics has been considered as a critical key to solve problems exhibited by virtually all flat panel displays and solar cells. Transparent electronics is expected to allow for the realization of displays with high aperture ratio for high brightness. This will enable the embedding of system-level electronics directly onto the display glass. The minimization of light lost when going through multi-layer stack structures is a major opportunity for solar cells and particularly for transparent solar cells consisting of transparent photovoltaic units. Over the last decade, amorphous phase and poly crystalline metal oxides, including ZnO, In_2O_3, and SnO_2 and their ternary and quaternary alloys, have been considered as candidates for transparent electronics. Using conventional vacuum-based deposition techniques and lithography technology, metal oxide based transistors with field effect mobility values high enough for the simultaneous operation of integrated circuits, pixel drivers and peripheral drivers have been demonstrated. In addition, by combining transparent source, drain, and gate electrodes with a transparent insulator, fully transparent circuits can be fabricated. Normally, hetero-junction solar cells consist of an absorber layer, its metal contacts, window layers, and their metal contacts. Transparent metal oxide n-type conducting window layers can be fabricated with the aforementioned semiconductors (ZnO, In_2O_3 or SnO_2). These layers provide a large band gap, excellent electronic transport properties, and easy metal contact formation. Among the aforementioned metal oxides SnO_2 has its own promising characteristics. It has a larger band-gap, lower melting point and higher bulk mobility Thus, a high-quality SnO_2 layer can potentially be created at a relatively low sintering temperature resulting in high performance transistor characteristics.

The main goals of this field are to improve process throughput for large area panels, to lower fabrication cost and to improve device performance. Combining the aforementioned attractive properties of SnO_2 with the process benefits of inkjet printing, fully ink-jet printed SnO_2 TFTs were demonstrated as a good candidate to achieve these main goals. To realize this, SnO_2, ZrO_2, and Sb-doped SnO_2 were selected for the transparent semiconductor, the insulator and the electrodes respectively. Solution phase

sol-gel precursors were used as inks for inkjet printing to form these materials. To fabricate uniform and coffee ring less layers, the spreading speed and evaporation rate were controlled by addition of a high-viscosity solvent mixture and with increased substrate temperatures. Using these innovations, transparent metal-oxide-based transistors were fabricated on glass substrates. These devices consisted of a SnO_2 semiconductor layer, a ZrO_2 insulator layer and Sb-doped SnO_2 electrodes formed through ink-jet printing. They exhibited excellent transistor characteristics, and thus represent a promising step towards making printed transparent electronic systems a reality.

Acknowledgements

Table of Contents

Chapter 1 Introduction

Transparent electronics are expected to solve a significant problem with virtually all flat panel displays and solar cells. Current display technologies emit light through a transparent glass substrate, but the pixel-driving transistors are opaque; as a result, there is a near-universal tradeoff between transistor sizing and the display aperture ratio. Wide, high-current transistors or multi-transistor pixel circuits are desirable for high-brightness and high-performance flat panel displays, but such components cannot be used without sacrificing the display aperture ratio, resulting in degraded display brightness and contrast. A major opportunity for solar cells, and particularly for transparent solar cells consisting of transparent photovoltaic units, is to minimize the loss of light through absorption when the light goes through a multi-layer stack structure. In addition, a multi-layer stack structure can expand the field of application for photovoltaics. For example, energy can be generated using the outside window of a building or the outside of a car. We can cover a larger area of the building or structure with transparent solar cells without loss of transparency or deterioration of the original appearance. We can also charge the batteries of mobile electric devices, such as cell phones or tablet PCs, through transparent solar cells on the top surface of a display while watching a video or checking e-mail in the sunshine at the same time. In winter, we can also imagine a transparent defroster or transparent heater on the front windshield or rear window of a car.

With regard to productivity and cost, intensive efforts over the last decade have targeted the production of low-cost integrated devices on large-area substrates, such as large-area transparent and flexible displays and solar cells [1-7]. However, large-area substrates are still expensive and are not cost competitive due to the high cost of conventional semiconductor manufacturing methods, such as vacuum-based deposition and photolithography. These processes are difficult to scale to large-area fabrication flows, and thus, there has been an emphasis within the display industry on the development of more scalable low-cost fabrication processes based on solution-processable material systems [8, 9] that are amenable to printing. Another example is the attempt by IBM and Nanosolar to fabricate a solar cell system with copper indium gallium selenide to reduce costs using a non-vacuum solution process. In addition, other types of semiconductors are in development, such as inorganic nanoparticles, wires, carbon nanotubes, and solution-phase organic materials.

Clearly, new candidate materials for electronic and optic applications are required to replace the conventional silicon. Additionally, a new technology for low-cost and transparent large-area applications must be developed to overcome the limitations of conventional silicon-based processing techniques. For these reasons, a solution-processable (e.g., spin casting and printing process) metal oxide system is one candidate to achieve these aims using a bottom-up strategy.

1.1. Thin film transistor technology

Thin film transistors (TFTs) are the most critical components in display backplane electronics. The operation and structure of TFTs are similar to those of conventional MOSFETs. The structures and operation mechanisms were first suggested in 1925 [10].

Commercialization of TFTs advanced significantly with the introduction of amorphous silicon devices. In 1979, the first TFT consisting of hydrogenated amorphous silicon (a-Si:H) on a silicon nitride gate dielectric layer was introduced [11]. The mobility of this a-Si:H-based TFT was approximately 1.0 cm^2/Vs. This was sufficient for pixel switching but was too low for applications that required high speeds and large currents, such as the row and column driving transistors in displays (versus the pixel transistors for LCDs, which required lower currents). Progress has continued unabated since then. Recently, TFTs on large area glass substrates (10th generation: 2.88 m X 3.15 m) were successfully fabricated.

A poly-Si-based technology has also been developed. The crystallinity and gain size are critical factors that impact the film quality, so, normally crystallization processes are needed, which often involve relatively high temperatures and long process times [12, 13]. However, using laser techniques, the thermal budgets can be controlled and laser sintered poly-Si based driver transistors and integrated circuits were demonstrated, successfully [14, 15]. The aforementioned amorphous and poly-Si based TFTs are suitable for use in large area liquid crystal displays (LCDs). Figure 1.1 shows a schematic of a TFT liquid crystal display structure. We can see the major parts of a TFT LCD herein. Specifically, on the back panel, each pixel consists of a TFT and storage capacitor. Figure 1.2 shows representations of the common tri- and bi-layer structures used in industry. Figure 1.3 shows the coplanar structure of a poly-Si-based TFT.
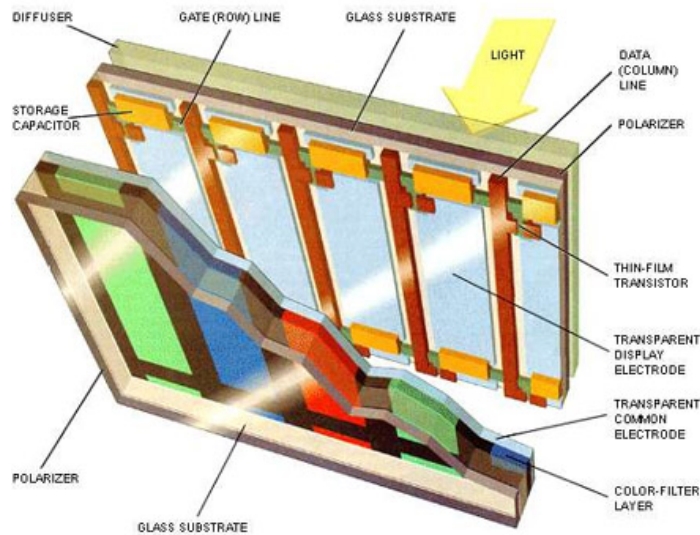
Figure 1.1 Schematics of the TFT liquid crystal display structure [16].
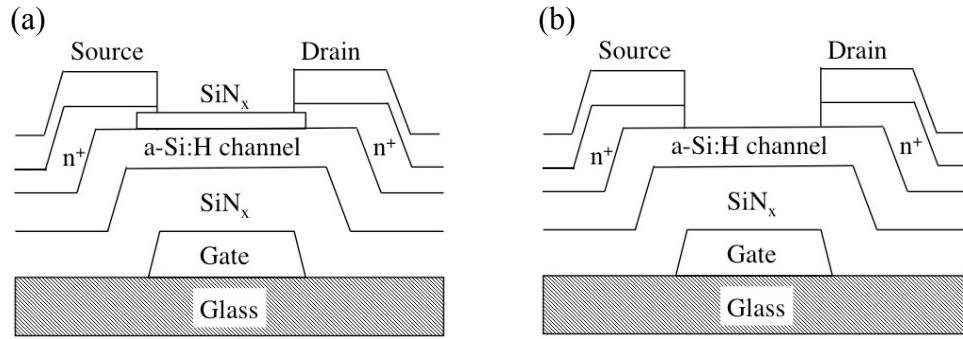
Figure 1.2 Inverted staggered (a) tri-layer and (b) bi-layer structures.
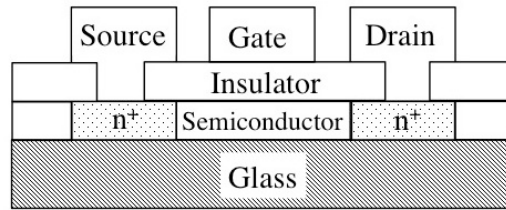
Figure 1.3 The coplanar structure of a poly-Si-based TFT.

Other types of semiconductor materials have been suggested as replacements for a-Si:H and poly Si. An organic material based TFT (OTFT) is one candidate. An organic semiconductor channel layer can be formed using conventional vacuum equipment, as well as using low-cost techniques such as spin-coating, dipping, and printing. Some OTFTs show better performance compared to a-Si:H TFTs. However, the viability of OTFTs has largely been limited by their poor stability in air and the large driving voltages required for their operation.

Recently, amorphous phase- and poly crystalline-based metal oxide TFTs have been considered as candidates as well. Even though the off-current of oxide TFTs are relatively high (~ 10^{-11} A), field effect mobility values high enough for simultaneous operation of integrated circuits, pixel drivers and peripheral drivers have been demonstrated. In addition, by combining transparent source, drain, and gate electrodes with a transparent insulator, fully transparent circuits can be fabricated.

The main goals of this field are to lower the cost, to improve yield, performance, and the throughput associated with large area panel fabrication. To achieve these goals, an understanding of the fundamental chemical and physical properties of the associated materials is required. In addition, new approaches involving non-vacuum-based deposition techniques and cheap plastic substrates, are required to lower the production costs. Thus, organic and metal oxide TFTs are under intensive investigation as replacements for Si-based FTFs, However, these new TFTs still have some disadvantages.

Many promising strategies have been suggested to overcome these advantages. Thus, in the future, it is expected that high performance and reliable TFTs and displays based on these can be successfully fabricated with these materials on different types of substrates.

1.2. Solution-based thin-film transistors

1.2.1. Solution-processable II-VI semiconductor nanoparticles

Thin-film deposition may be achieved by conventional vacuum based deposition technique and patterned using a photolithography process. However, depositing high-quality thin films on substrates via a solution process has challenged the field over the last decade. Recently, the major focus has been on solution-based organic materials. In particular, there has a significant emphasis on the use of organic semiconductors for this application. For example, among high-mobility organic semiconductors, Dithioperylene [17] or organic single crystal nano-ribbon [18] result in field effect mobilities of approximately 0.45 and 2.0 cm^2/Vs, respectively. These materials have been used for optoelectronic devices and radio-frequency identification tags. However, the low field effect mobility of these TFTs is not suitable for applications in display drivers and active matrix backplanes for high-resolution displays. When compared to organic materials, inorganic materials, such as Si-, GaAs-, or InP-based transistors, result in a higher field effect mobility and chemical stability. Unfortunately, aside from using the conventional vacuum-based deposition technique, it has been difficult to form the layers with a solution phase for large-area and low-cost processes. Promising inorganic materials have been introduced for a bottom-up fabrication strategy to overcome these limitations. First, intensive efforts have targeted on the deposition of high-quality films with nanoparticles (NPs) for electronic and optoelectronic applications. This approach decreases the sintering temperature because of the particle size and because high-crystallinity thin films can be formed easily on different types of substrates, including glass or plastic substrates. This property plays a critical role in the attractiveness of these materials for use as the main channel layer for devices. Devices based on the aforementioned films consisting of sintered NPs have displayed high performance. For example, a NP-based thin-film transistor was demonstrated in 1999, and it is considered to have the potential to overcome the disadvantages of organic- and silicon-based electronic devices. Figure 1.4 presents a TEM image of the synthesized CdSe NP and the electrical characteristics of a CdSe NC-based thin-film transistor by a printing system [19]. The fabricated TFT exhibits a mobility of approximately 1.0 cm^2/Vs.

Additionally, PbSe NC-based p- and n-type thin-film transistors have been realized that achieve hole and electron mobilities of 0.2 and 0.9 cm^2/Vs, respectively, in Figure 1.5 [20]. Recently, high-performance thin-film transistors with inorganic n-type HgSe NC [21] and p-type HgTe [22] NC-based transistors were demonstrated on plastic substrates, as shown in Fig. 1.6, with field effect mobilities of 3.9 and 4.0 cm^2/Vs,

respectively. Unfortunately, the synthesis process is complex, and these material systems are binary or ternary material systems that include toxic heavy metals, such as mercury, cadmium, or lead. Furthermore, it is still difficult to dope these NCs to control the electrical and physical characteristics required to tune the device.

(a)   (b)
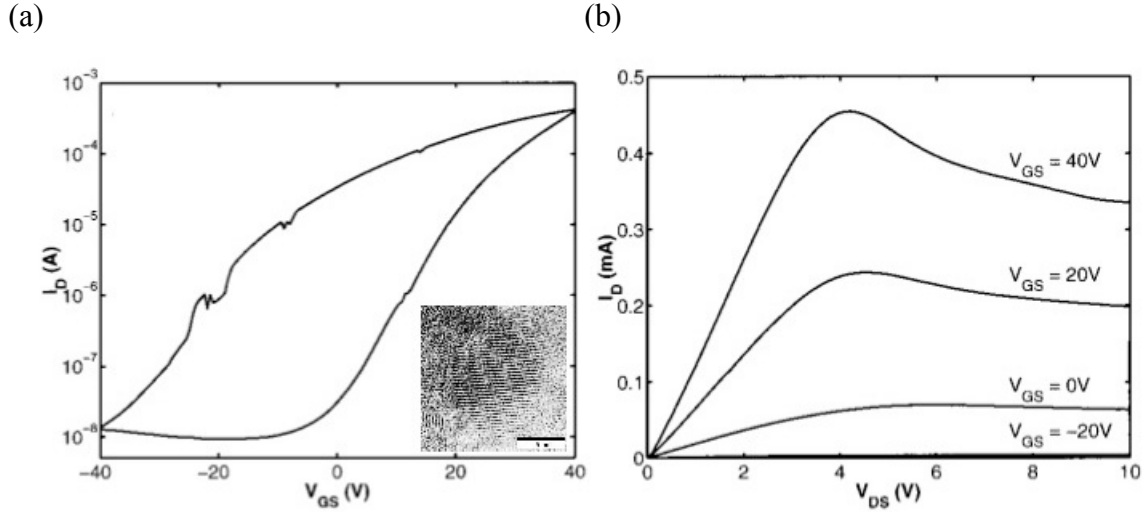
Figure 1.4 Drain current versus gate source voltage (I_D-V_{GS}) and drain current versus drain source voltage (I_D-I_{DS}) characteristics of a TFT. The inset presents the TEM image of the synthesized CdSe NP after a 30 min heat treatment at 350°C [19].
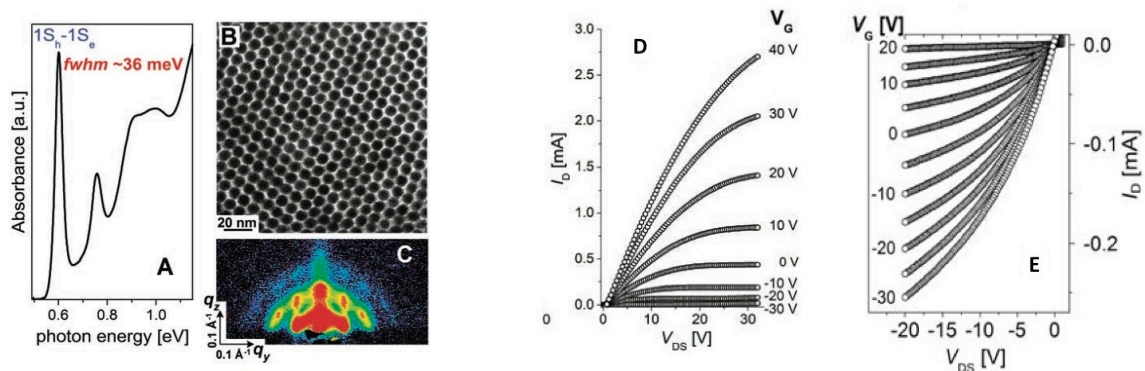
Figure 1.5 (A) Optical absorption spectrum of a colloidal solution of 8 nm PbSe NPs. (B) TEM image of an array of 8 nm PbSe NPs. (C) GISAXS patterns of a PbSe NP thin film. (D) Characteristics of an n-channel thin-film transistor and (E) characteristics of a p-channel thin-film transistor [20].
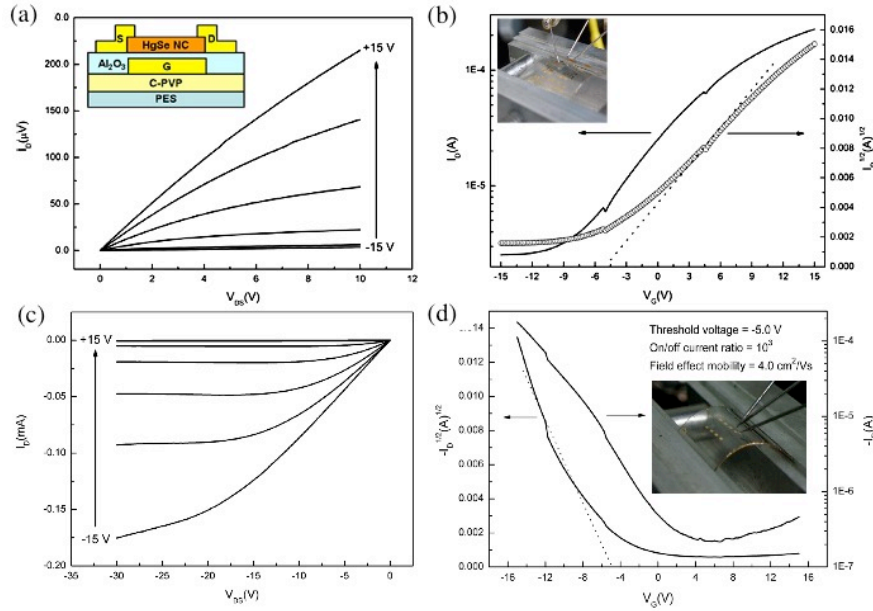
Figure 1.6 (a) and (b): Drain current versus drain source voltage (I_D-I_{DS}) characteristics and drain current versus gate source voltage (I_D-V_{GS}) of a HgSe NP-based n-channel flexible TFT [21]. (c) and (d): Drain current versus drain source voltage (I_D-I_{DS}) characteristics and drain current versus gate source voltage (I_D-V_{GS}) of a HgHe NP-based p-channel flexible TFT [22].

1.2.2. Sol-gel processing

Sol-gel processing is another representative method to fabricate thin films without using the conventional vacuum-based deposition technique. A sol is composed of colloidal particles in solvent, and a gel is a porous one- or three-dimensional interconnected solid network. The prepared sol or gel in solvent can be easily transformed into various types of structures, such as powders, fibers, thin films, monoliths, or ordered pores, by treating it with conventional processing techniques, such as cold pressing, hot pressing, or sintering. Sol-gel processing possesses several advantages over the aforementioned NP synthesis and NP-based fabrication processing methods (i.e, the complex and toxic heavy metal based synthesis processes, and difficulties of doping NPs).

The products obtained via sol-gel processing are highly pure, originating from a simple process that minimizes the number of fabrication steps. For example, the first step of the sol-gel process is performed at a relatively low temperature, which leads to the minimization of the chemical interaction between the prepared precursors and container walls. In addition, the colloidal sols are in a solvent, which prevents additional pollution by the dust dispersion. The shape, size, and size distribution of the final products can be controlled by modulating the process temperature or adding specific chemicals. The final

materials consist of several components (i.e., when several metal oxides are binary or ternary) and can be easily formed using a combination of precursors and processing steps. The three major components for transistors (electrodes, semiconductors, and insulators) are easily fabricated by selecting the appropriate metal salt precursors.

The sol-gel process has become widely used in recent years due to the transparent characteristics of metal oxides. Using the sol-gel process, we can make many different metal oxides that have different chemical, physical, and electrical characteristics. Some example applications include antireflective coatings with index gradation [23], optical or infrared-absorbing coatings [24], protective coatings for scratch, oxidation, and erosion resistance, electrochromics for smart windows [25], and transparent electrodes [26, 27].

With regard to the fabrication process, the phase of the prepared precursor is liquid and can be used as inks for spin-coatings, spray techniques, and printing systems. We can easily deposit thin films without using conventional vacuum-based deposition tools with this process. When combined with an ink-jet printing system, printed electronics with sol-gel systems has the potential to fulfill the requirements for large-area and low-cost applications and will be a promising candidate for producing next-generation transparent electronics.

1.3. Ink-jet printing

The conventional IC fabrication method for electronic devices includes a series of vacuum-based deposition techniques and lithography processes that include a spin-coating process, exposure with masks, development, and an etching process to make patterned thin films. The facilities for these processes normally require expensive and time consuming high vacuum systems, and the size of substrates is limited by the chamber size. The printing technologies employed by the newspaper and graphic art industries have been considered as possible methods to overcome these issues. Several classes of printing platforms exist, including gravure, screen, stencil, and ink-jet. Among these printing techniques, gravure and ink-jet printing are the most promising techniques to implement printed electronics due to their high throughput and high printing resolution.

Figure 1.7(a) presents the typical gravure printing system. It consists primarily of a layout-engraved plate cylinder, a doctor blade, and impression cylinder. The ink is carried from the ink tray by the engraving depressions. The excess ink is stripped off by a fixed doctor blade. Finally, the impression roller presses and inks are transferred from the engraved plate cylinder to the substrate. Compared to the gravure printing system, ink-jet printing is a 100% non-contact printing system. As illustrated in Figure 1.7(b), ink-jet printing consists of a reservoir and ink-jet nozzle. The mechanism to form the droplet in the ink-jet printing system is simple. There is an actuator consisting of a piezoelectric plate inside a nozzle chamber that is filled with ink. A voltage pulse is applied to the piezoelectric plate, triggering an acoustic wave that propagates inside the chamber to form the droplet. The ejected droplet falls by external factors, such as gravity (tends to be unimportant for small drops), the generated pressure pulse, the influence of an

electrostatic field (e.g., in electrohydrodynamic printing) and the air resistance, until it lands on the substrate and spreads. The manner in which the drop spreads, and the final shape of the droplet are strongly influenced by the droplet velocity, its diameter, the ink viscosity, and the surface tension.

(a)   (b)
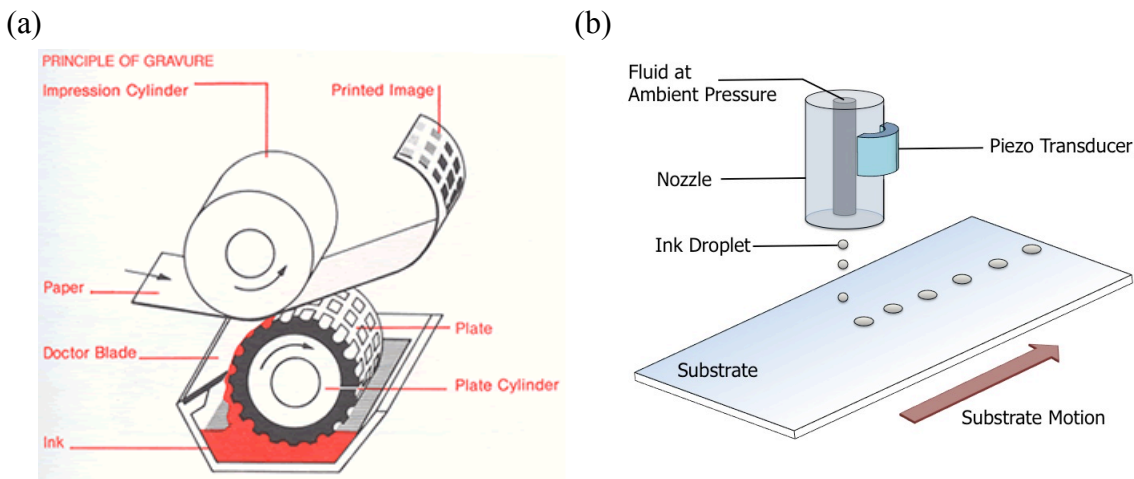
Figure 1.7 (a) The principle of gravure printing (image courtesy of Prism Pak, Inc.); (b) an ink-jet printing system.

Ink-jet printing technology has several attractive features: it reduces waste; requires less contact; and uses a wide range of solution-phase materials, such as liquid-phase organic materials, nano-sized materials [28-32] (e.g., NPs, nanowire, CNTs, and graphene) in a specific solvent, or precursors for the sol-gel process [33]. Additionally, ink-jet printing allows for flexibility in pattern customization, has a high throughput, and is scalable to large-area applications on many different substrates.

Understanding the flow properties of a droplet is important for the development of the ink-jet printing process. To date, research on the fabrication of printed electrical devices using inorganic materials has only reported the use of metal NCs, such as non-transparent silver or gold NCs, to produce single dots and continuous lines. Several attempts have been made to use sol-gel to produce transparent conductive electrodes or semiconductors; however, these reports lack information regarding the morphological control required to produce uniform layers or a single separate device.

One challenging issue is to make uniform films by controlling the movement of drops. Controlling the behavior of liquid phase drops on substrates is not easy and there are some well-known problems. The most well-known issue is the coffee ring effect, resulting in non-uniform film formation. Higher evaporation rates at the droplet rims intensify the outward radical flow to make up for the loss of solvent at the rims. This results in relatively thicker films at the rims of deposited droplets compared to the center areas. Significant insulator or semiconductor sidewalls, originate from the coffee ring effects, may be not critical issues for single separated devices if we fabricate a single device on flat thin central areas of each layer However, the coffee ring effect must be

avoided when fabricating integrated circuits connected to each unit transistor through interconnection lines or three-dimensional stacked structures because uniform layers are required. In this thesis, this issue was resolved by adding an additional solvent, and by controlling the surface energy and evaporation rates by controlling substrate temperatures, as discussed in Chapter 4.

1.4. SnO_2 semiconductor

SnO_2 belongs to a promising family of oxide materials that have both low electrical resistance and high optical transparency in the visible range. These characteristics are critical factors for use as an active channel layers for sensors, thin film transistor, transparent electrode in solar cells, light-emitting diodes, flat-panel displays, and other electric devices in which a transparent semiconductor or electrode is needed [27, 28]. In addition, SnO_2 is transparent in the visible light spectrum originally. However, it is also possible to make infrared reflective films by a doping process like other metal oxides [34, 35]. The Sb or F doped SnO_2 property can be used to make energy conservation materials [36]. When deposited on a window, SnO_2 can trap heat to save the energy needed to increase the temperature inside of a building. Furthermore, by combining SnO_2 with transparent electrochromic materials, such as WO_2 or NiO_2, the color or transparency of windows can be changed by biasing a voltage across the films.

There are many transparent conducting oxides, including binary and ternary materials. The most common binary materials are ZnO, In_2O_3, and SnO_2. Among these, SnO_2 has its own promising characteristics. It has a larger band-gap, lower melting point, and higher bulk mobility [37]; a summary of the characteristics of common binary materials is provided in Table 1.1. Thus, a high-quality SnO_2 layer can potentially be created at a relatively lower sintering temperature, resulting in higher performance.

SnO_2 possesses a rutile (tetragonal) structure, and the lattice constants are a = b = 0.474 nm and c = 0.319 nm. The surface energy of low-index SnO_2 surfaces has been calculated. Based on this result, the (110) surface is the lowest-energy surface. Therefore the majority of the surface area of pure bulk SnO_2 is (110) surface and the first major XRD peak of the formed SnO_2 driven by the sol-gel process verifies this result. Figure 1.8 presents the ball-and-stick models of the SnO_2 structure corresponding to different lattice directions [38].

The understanding of the band structure of SnO_2 is helpful in determining the suitability of SnO_2 for use as a transparent active channel layer. Figure 1.9 presents the band diagram of SnO_2. First of all, the phonon transition can occur at the τ point (direct transition), corresponding to the energy gap (~ 3.6 eV) and no inter-band electron excitation paths. These properties ensure transparency even for large charge carrier concentrations. In addition, the increased charge carriers increase the optical band-gap by promoting the minimum energy for the phonon transition, due to the significant s-type conduction dispersion with a low effective mass.

Property	In_2O_3	SnO_2	ZnO	Si [84]
Mineral name	—	cassiterite	zincite	silicon
Average amount of the metal in the earth's crust (ppm)	0.1	40	132	2.58×10^5
Band gap E_g (300 K) (eV)	2.7 (indir) 3.75 (dir)	3.6 (dir)	3.4 (dir)	1.12 (indir) 4.18 (dir)
Pressure coefficient dE_g/dp (meV kbar^{-1})			2.33	-1.41
Static dielectric constant ε_r	≈ 9	$\parallel c$: 9.6 $\perp c$: 13.5	$\parallel c$: 8.75 $\perp c$: 7.8	11.9
Effective electron mass m^*/m_e	0.35	$\parallel c$: 0.23 $\perp c$: 0.3	0.28	0.337
Non-parabolicity parameter α (eV^{-1})		0.96 [97]	0.29 1.04 [23]	0.27 [101] 0.5 [9]
Effective conduction band density of states (300 K) N_C (cm^{-3})	4.1×10^{18}	3.7×10^{18}	3.7×10^{18}	4.9×10^{18}
Extrinsic dopants	Sn, Ti, Zr, F, Cl, Sb, Ge, Zn, Pb, Si	Sb, (As, P) F, Cl	B, Al, Ga, In, Si, Ge, Sn, Y, Sc, Ti, Zr, Hf F, Cl	B, Al, Ga, In P, As, Sb
Other phases in the dopant–host system (heat of formation (eV))	$In_4Sn_3O_{12}$ SnO (2.9) SnO_2 (6.0) TiO_2 (9.8) ZrO_2 (11.2) GeO_2 (5.6) SiO_2 (8.8) ZnO (3.6) Sb_2O_3 (7.2) Sb_2O_5 (10.0)	As_2O_3 (6.7) As_2O_5 (9.5) Sb_2O_3 (7.2) Sb_2O_5 (10.0) P_2O_5 (15.6)	ZnO_2 B_2O_3 (6.6) Al_2O_3 (8.7) Ga_2O_3 (5.7) In_2O_3 (4.8) TiO_2 (9.8) Y_2O_3 (19.8) HfO_2 (11.8) ZrO_2 (11.2) $ZnAl_2O_4$ (21.4) $ZnGa_2O_4$ (15.3)	SiB_3 SiB_6 SiP SiAs $SiAs_2$
Crystal structure	cubic, bixbyite	tetragonal, rutile	hexagonal, wurtzite	cubic, diamond
Space group (number)	$I2_13$ (no199)	$P4_2mnm$ (no 136)	$P6_3mc$ (no 186)	Fd3m (no 227)
Lattice parameter(s) (nm)	a: 1.012	a: 0.474 c: 0.319	a: 0.325 c: 0.5207	a: 0.5431
Density ρ (g cm^{-3})	7.12	6.99	5.67	2.33
Thermal expansion α (300 K) (10^{-6} K^{-1})	6.7	$\parallel c$: 3.7 $\perp c$: 4.0	$\parallel c$: 2.92 $\perp c$: 4.75	2.59
Melting point (°C)	2190	>1900^a	2240	1415
Melting point of the metal (°C)	157	232	420	1415
Heat of formation (eV)	9.7	6.0	3.6	—

^{a}Decomposition into SnO and O_2 at 1500 °C.

Table 1.1 Properties of zinc oxide and other TCO materials compared to those of Si [37].
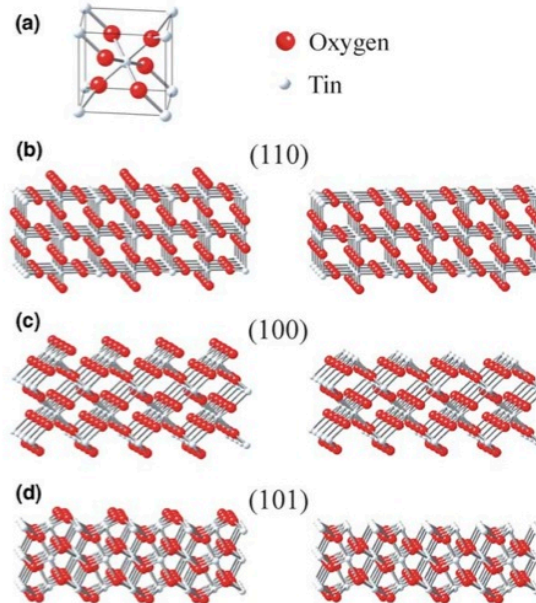
Figure 1.8 Ball-and-stick models of the low-index surfaces of SnO_2: (a) the bulk rutile unit cell; (b), (c), and (d) present the (110), (100), and (101) surfaces, respectively [38].
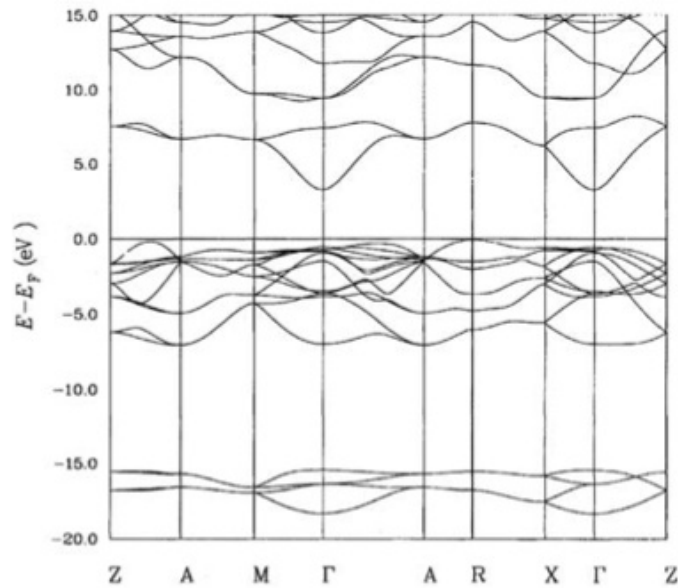
Figure 1.9 Band structure calculation for SnO_2 [38].

SnO_2 can be used as a gas sensor active channel, similar to other metal oxides such as ZnO and In_2O_3. The mechanism causing a gas response is that of trapping the electrons of absorbed molecules and inducing band bending. The molecules result in a change in conductivity [39, 40]. The absorbed molecules at the surface result in a net charge and cause an additional electric field. This additional electric field results in band bending in the SnO_2. The depletion region is formed due to the band bending, reducing the carrier concentration. This effect is illustrated in Figure 1.10.
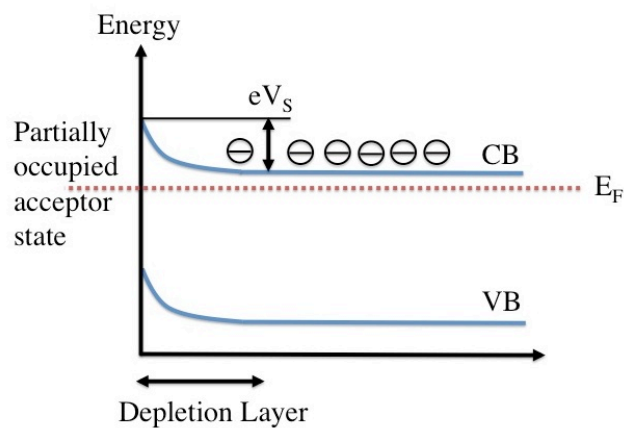
Figure 1.10 The formation of a depletion area in the near surface area, originating from absorbed molecules at a surface [38].

Another important factor of the gas response is the barriers between grains [41]. Figure 1.11 presents a schematic of the situation in polycrystalline active layers. Upward band bending resulting from surface charges induces a barrier to current flow and increases the resistance of active channel layers.
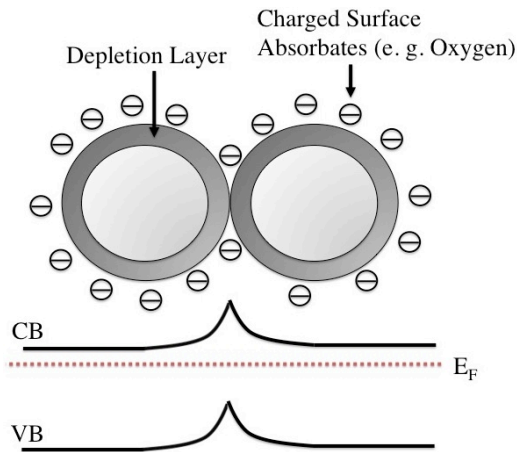
Figure 1.11 Schematic of absorbed molecules. Negatively charged oxygen molecules lead to upward band bending and result in a depletion zone between the grain boundaries. This depletion zone leads to a Schottky-like barrier [38].

A variety of dopants have been investigated to improve the properties of SnO_2 for specific applications. The first major application is to use as transparent electrodes by increasing the conductivity. This investigation included Mo [42], Ta [43], Sb [44-46], Li [47], and F [48]. Among these dopants, Sb is a common n-type dopant in SnO_2. An increase in the weight percent of Sb results in a significant increase in the free carrier concentration, and the optical bandgap is increased by 0.35 eV for heavily Sb-doped SnO_2 compared to pure SnO_2. The conductivity of Sb-doped SnO_2 is dependent on the antimony content and oxidation state in the tin oxide lattice. The Sb^{5+} ion acts as the electron donor, and the Sb^{3+} ion acts as the electron acceptor inside the SnO_2. The conductivity increases considerably when the effective donor Sb^{5+} concentration exceeds that of the electron acceptor, Sb^{3+} [44].

1.5. Thesis organization

This thesis is organized in the following manner. In chapter 2, the inkjet printing system will be introduced. The fundamental basics of sol gel processes and the ink

behavior on surfaces are explained. Thin film transistor operation and transport mechanisms are also introduced. Chapter 3 will introduce and discuss the tin oxide thin film properties, and n-type tin oxide based thin film transistor characteristics. In addition, sol-gel processed ZrO_2 insulator characteristics will be also discussed. Chapter 4 will introduce antimony doped tin oxide for transparent electrodes. Major solvent change techniques, to deposition coffee ring less printed layers for a stack structure such as fully printed thin film transistors, will be suggested. Chapter 5 will conclude the thesis and outline the potential future work.

1.6. References

[1] Q. Cao, H. –S. Kim, N. Pimparkar, J. P. Kulkarni, C. Wang, M. Shim, K. Roy, M. A. Alam, J. A. Rogers, "Medium-scale carbon nanotube thin-film integrated circuits on flexible plastic substrates," *Nature*, vol. 454, 495-500, 2008.

[2] G. H. Gelinck, H. E. A. Huitema, E. van Veenendaal, E. Cantatore, L. Schrijnemakers, J. B. P. H. van der Putten, T. C. T. Geuns, M. Beenhakkers, J. B. Giesbers, B. H. Huisman, E. J. Meijer, E. M. Benito, F. J. Touwslager, A. W. Marsman, B. J. E. van Rens, D. M. de Leeuw, "Flexible active-matrix displays and shift registers based on solution-processed organic transistors," *Nat. Mater.*, vol. 3, 106–110, 2004.

[3] T. Sekitani, T. Yokota, U. Zschieschang, H. Klauk, S. Bauer, K. Takeuchi, M. Takamiya, T. Sakurai, T. Someya, "Organic Nonvolatile Memory Transistors for Flexible Sensor Arrays," *Science*, vol. 326, 1516–1519, 2009.

[4] K. Myny, S. Steudel, P. Vicca, M. J. Beenhakkers, N. A. J. M. van Aerle, G. H. Gelinck, J. Genoe, W. Dehaene, P. Heremans, "Plastic circuits and tags for 13.56 MHz radio-frequency communication," *Solid State Electron*, vol. 53, 1220–1226, 2009.

[5] C. G. Granqvist, "Transparent conductors as solar energy materials: A panoramic review," *Sol. Energy Mater. Sol. Cells*, vol. 91, 1529–1598, 2007.

[6] H. T. Han, Y. Lee, M. R. Choi, S. H. Woo, S. H. Bae, B. H. Hong, J. H. Ahn, T. W. Lee, "Extremely efficient flexible organic light-emitting diodes with modified graphene anode," *Nat. Photonics*, vol. 6, 105–110, 2012.

[7] B. Schmied, J. Gunther, C. Klatt, H. Kober, E. Raemaekers, "STELLA-STretchable ELectronics for Large Area Applications -A New Technology for Smart Textiles," *Smart Textiles*, vol. 60, 67–73, 2009.

[8] H. Minemawari, T. Yamada, H. Matsui, J. Tsutsumi, S. Haas, R. Chiba, R. Kumai, T. Hasegawa, "Inkjet printing of single-crystal films," *Nature*, vol. 475, 364–367, 2011.

[9] Y. H. Yang, S. S. Yang, C. Y. Kao, K. S. Chou, "Chemical and Electrical Properties of Low-Temperature Solution-Processed In–Ga–Zn-O Thin-Film Transistors," *IEEE Electron Device Lett.*, vol. 31, 329–331, 2010.

[10] R. G. Arns, "The other transistor: early history of the metal-oxide-semiconductor field-effect transistor, " *Eng. Sci. Edu. J.*, vol. 7, pp. 233, 1998.

[11] P. G. LeComber, W. E. Spear, A. Ghaith, "Amorphous-silicon field-effect devices and possible application," *Electron. Lett.*, vol. 15, pp. 179, 1979.

[12] J. Jang, "Polycrystalline silicon thin film transistors," *Kluwer Academic Publishers*, pp. 230, 2004.

[13] Y. Kuo, P. M. Kozlowiski, "Polycrystalline silicon formation by pulse rapid thermal annealing of amorphous silicon," *Appl. Phys. Lett.*, vol. 69, pp. 2091, 1996.

[14] M. Hatano, M. Matsumura, Y. Toyota, M. Tai, H. Hamamura, T. Miyazawa, M. Ohkura, "High reliability and performance poly-Si TFTs for system in display," *ECS Trans.*, vol. 3, pp. 35, 2006.

[15] Y. Yamamoto, A. T. Voutsas, "Technology trend of AMLCDs for mobile application," *ECS Trans.*, vol. 3, pp. 11, 2006.

[16] S. W. Depp, W. E. Howard, "Flat panel displays," *Scientific America*, vol. 266, pp. 90, 1993.

[17] W. Jiang, Y. Zhou, H. Geng, S. Jiand, S. Yan, W. Hu, Z. Wnag, Z. Shuai, J. Pei, "Solution processed, high performance nanoribbon transistor based on dithioperylene," J. Am. Chem. Soc., vol. 133, pp. 1-3, 2011.

[18] Y. Zhou, T. Lei, L. Wnag, J. Pei, Y. Cao, J. Wang,"High-performance organic field effect transistor from organic single crystal microribbons formed by a solution process," Adv. Mater., vol. 22, pp. 1484-1487, 2010.

[19] B. A. Ridley, B. Nivi, J. M. Jacobson, "All-inorganic field effect transistors fabricated by printing," *Science*, vol. 286, 746, 1999.

[20] D. V. Talapin, C. B. Murray, "PbSe nanocrystal solids for n- and p-channel thin film field effect transistors," *Science*, vol. 310, 86-89, 2005.

[21] J. Jang, K. Cho, J. Yun, S. Kim, "N-channel thin-film transistors constructed on plastic by solution processes of HgSe nanocrystals," *Journal of microelectronic Engineering*, vol. 86, 2030-2033, 2009.

[22] J. Jang, K. Cho, S. H. Lee, S. Kim, "Transparent and flexible thin film transistors with channel layers composed of sintered HgTe nanocrystals," *Nanotechnology*, vol. 19, 015204, 2008.

[23] G. S. Vicente, A. Morales, S. Suarez, B. Sánchez, N. Germán, "SiO$_2$/TiO$_2$ antireflective coatings with photocatalytic properties prepared by sol-gel for solar glass covers," *J. Sol. Energy Eng.*, vol. 134, 041001-041005, 2012.

[24] A. Makishima, H. Kubo, K. Wada, Y. Kitami, T. Shimohira, "Yellow Coatings Produced on Glasses and Aluminum by the Sol-Gel Process," *J. Am. Ceram. Soc.*, vol. 69, C127-129, 1986.

[25] G. A. Niklasson, C. G. Granqvist, "Electrochromics for smart window: thin films of tungsten oxide and nickel oxide, and devices based on these," *J. Mater. Chem.*, vol. 17, 127-156, 2007.

[26] D. Zhang, L. Tao, Z. Deng, J. Zhang, L. Chen, "Surface morphologies and properties of pure and antimony-doped tin oxide films derived by sol-gel dip coating processing." *Materials Chemistry and Physics*, vol. 100, 275-280, 2006.

[27] B. Benrabah, A. Bouaza, S. Hamzaoui, A. Dehbi, "Sol-gel preparation and characterization of antimony doped thin oxide (ATO) powders and thin films," *Eur. Phys. J. Appl. Phys.*, vol. 48, 30301, 2009.

[28] Y. Y. Noh, X. Cheng, H. Sirringhaus, J. I. Sohn, M. E. Welland, D. J. Kang, "Ink-jet printed ZnO nanowire field effect transistors," *Appl. Phys. Lett.,* vol. 91, 043109, 2007.

[29] P. Beecher, P. Servati, A. Rozhin, A. Colli, V. Scardaci, S. Pisana, T. Hasan, A. J. Flewitt, J. Robertson, G. W. Hsieh, F. M. Li, A. Nathan, A. C. Ferrari, W. I. Milne, "Ink-jet printing of carbon nanotube thin film transistors," *J. Appl. Phys.,* vol. 102, 043710, 2007.

[30] G. W. Hsieh, F. M. Li, P. Beecher, A. Nathan, Y. Wu, B. S. Ong, W. I. Milne, "High performance nanocomposite thin film transistors with bilayer carbon nanotube-polythiophene active channel by ink-jet printing," *J. Appl. Phys.*, vol. 106, 123706, 2009.

[31] T. Shimoda, Y. Matsuki, M. Furusawa, T. Aoki, I. Yudasaka, H. Tanaka, H. Iwasawa, D. Wang, M. Miyasaka, Y. Takeuchi, "Solution-processed silicon films and transistors," *Nature*, vol. 440, 783-786, 2006.

[32] F. Torrisi, T. Hasan, W. Wu, Z. Sun, A. Lombardo, T. S. Kulmala, G. W. Hsieh, S. Jung, F. Bonaccorso, P. J. Paul, D. Chu, A. C. Ferrari, "Inkjet-printed graphene electronics," *ACS Nano*, vol. 6, 2992-3006, 2012.

[33] D. Kim, Y. Jeong, C. Y. Koo, K. Song, J. Moon, "Thin Film Transistors with Ink-Jet Printed Amorphous Oxide Semiconductors," *Jpn. J. Appl. Phys.*, vol. 49, 05EB06, 2010.

[34] Y. Okuhara, H. Matsubara, C. Numako, M. Takata, "Effective doping Al in ZnO films by multi target reactive sputtering for near-infrared reflection," *Journal of the Australian ceramic society*, vol. 49, pp. 15-20, 2013.

[35] R. Das, S. Ray," Zinc oxide-a transparent, conducting IR-reflector prepared by rf-magnetron sputtering," *J. Phys. D: Appl. Phys.*, vol. 36, pp. 152-155, 2003.

[36] Z. Zhang, Y. Gao, H. Luo, L. Kang, Z. Chen, J. Du, M. Kanehira, Y. Zhang, Z. L. Wang, "Solution based fabrication of vanadium dioxide on F:SnO$_2$ substrates with largely enhanced thermochromism and low emissivity for energy saving applications," *Energy, Environ. Sci.*, vol.4, pp. 4290-4297, 2011.

[37] K. Ellmer, "Resistivity of polycrystalline zinc oxide films: current status and physical limit," *J. Phys, D: Appl. Phys.*, vol. 34, 3097-3108, 2001.

[38] M. Batzill, U. Diebold. "The surface and materials science of tin oxide," *Progress in Surface Science*, vol. 79, pp. 45-154, 2005.

[39] W. Gopel, "Chemisorption and charge transfer at ionic semiconductor surfaces: implications in designing gas sensors," *Prog. Surf. Sci.*, vol. 20, 9, 1985.

[40] M.J. Madou, S.R. Morrison, Chemical Sensing with Solid State Devices, Academic Press, Boston, 1989.

[41] C. Malagu, V. Guidi, M. Stefancich, M.C. Carotta, G. Mertinelli, "Model for Schottky barrier and surface states in nanostructured n-type semiconductors," *J. Appl. Phys.*, vol. 91, 808, 2002.

[42] E. Zampiceni, E. Bontempi, G. Sberveglieri, L.E. Depero, "Mo influence on SnO$_2$ thin film properties," *Thin Solid Films*, vol. 418, 16, 2002.

[43] S. W. Lee, Y.-W. Kim, H. Chen, "Electrical properties of Ta-doped SnO$_2$ thin films prepared by the metal- organic chemical-vapor deposition method", *Appl. Phys. Lett.*, vol. 78, 350, 2001.

[44] V. Muller, M. Rasp, G. Stefanic, J. Ba, S. Gunther, J. Rathousky, M. Niederberfer, D. Fattakhova-Rohlfing, "Highly conducting nanosized monodispersed antimoany-doped tin oxide particles synthesized via nonaqueous sol-gel procedure," *Chem. Mater.*, vol. 21, 5229-5236, 2009.

[45] C. Terrier, J. P. Chatelon, R. Berjoan, J. A. Roger, "Sb-doped SnO_2 transparent conducing oxide from the sol-gel dip-coating technique," *Thin Solid Films*, vol. 263, 37-41, 1995.

[46] S. Y. Lee, B. O. Park, "Structural, electrical and optical characteristics of SnO_2:Sb thin films by ultrasonic spray pyrolysis," *Thin Solid Films*, vol. 510, 154-158, 2006.

[47] M.-M. Bagheri-Mohagheghi, M. Shokooh-Saremi, "Electrical, optical and structural properties of Li-doped SnO_2 trasnparent conducting films deposited by spray pyrolysis technique: a carrier-type conversion study," *Semicond. Sci. Technol.*, vol. 764, 2004.19 (2004) 764.

[48] M. C. Esteves, D. Gouvea, P. T. A. Sumodjo, "Effect of fluorine doping on the properties of tin oxide based powders prepared via Pechini's method," *Appl. Surf. Sci.*, vol. 229, 24, 2004.

Chapter 2 Ink-jet Printed Transistors: The Basics

As discussed in the previous chapter, ink-jet printing technology has several attractive features; it reduces waste, requires less contact, and uses a wide range of solution-phase materials, such as liquid-phase organic materials and nano-sized materials (e.g., NPs, nanowire, CNTs, and graphene) in a specific solvent. Additionally, it allows for flexibility in pattern customization, has a high throughput, and is scalable to large-area applications on many different substrates. For these reasons, there have been investigations into printed devices using the ink-jet method [1–4]. Simultaneously, many different types of solution phase inks have been proposed for use as inks for ink-jet printing systems. The solution-phase precursor for the sol-gel process has been suggested for an ink-jet printing system due to ease of preparation and the higher performance expected compared to organic solution-phase materials. Compared to liquid phase organic semiconductor, NP, or sol gel processed semiconductor based TFTs, single crystalline nanowire and CNT based TFTs have shown high performance and promising results. However, significant issues remain, including those associated with the alignment, etc.

In this chapter, we will first introduce the sol-gel process and the basic theory used for the sol-gel process in this thesis work. Next, the ink-jet printing system will be introduced. In addition, the surface morphology of drops and how this morphology is influenced by several parameters will be explained. Finally, the basics of thin-film transistors will be discussed based on the conventional model and additional non-ideal transport models will be introduced.

2.1. Sol-gel processed metal oxide inks for ink-jet printing

In this thesis, the prepared solution phase inks for the sol-gel process are suggested as the inks for inkjet-printed device fabrication. After conducting a sintering process, the deposited precursor will convert into metal oxides. However, corresponding to different precursors and sintering conditions, we will obtain different phases and different converted thin films. To achieve the goal that we expect, a critical understanding of this process is needed. The mechanism of the sol-gel process is introduced and discussed in this chapter.

2.1.1. Sols, gels, and gelation

A sol is a stable colloidal particle in solvent. A high concentration of sols should be present inside the solvent for stability. Furthermore, each sol should be sufficiently small or exhibit adequate electrical charge to stay dispersed in solvent stable. If the sol is too large, its dynamic motion in solvent is governed by the force of gravity. Normally, the sizes of sols are between 1 nm to several hundred nanometers. The solvent containing the stable sols is pure water, a solution composed mostly of water, or other solvents for specific properties, such as organic solvents and alcohol.

A gel is the one- or three-dimensional interconnected solid network phase consisting of the unit sol. The properties of the gel are established according to the coexistence between the networks originating from different prepared precursors, the polarity of the precursor, or the liquid medium. The solvent between networks that composes the gels should be in thermodynamic equilibrium with the networks. The gels are called aqua gels or hydrogels if the solvent is either pure water or composed largely of water. In contrast, an alcogel is formed if the major solvent is alcohol. After removing most of the solvent, it can also be called an aerogel, xerogel, or dry gel. The gelation process occurs when the stable sols convert into a uniform one- or three-dimensional gel form. This gelation minimizes the inhomogeneity in this system.

2.1.2. Overview of sol-gel processing

The output of the sol-gel process differs based on the precursors, liquid medium, surfactants, and sintering conditions. The schematic process flow is illustrated in Figure 2.1. The first step of the sol-gel process is selecting the precursors and solvents. In addition, the use of a combination of different precursors enhances the different chemical reactions and different products to make binary, ternary, or doped materials. The sol size of the sol, the pore size, and the crystallinity of the final products can be controlled by changing the precursor concentration, using specific surfactants, controlling sintering process conditions, or changing the ratio between two or three different precursors. The formation of sols in the solvents proceeds through four steps: hydrolysis, condensation, nucleation and growth. Increased concentrations of precursors often increase the nucleation and growth rates, leading to larger sols [5]. By adding surfactants, such as polyvinlypyrrolidone or ethylene glycol [6], the sol can be encapsulated to suppress the grain growth, resulting in small sols, with narrow size distributions, and more spherical shaped sols. Increasing process temperature accelerates the chemical reactions, leading to larger sols. The addition of acids and bases generates H^+ and OH^- that attacks one of the hydrogen atoms of water molecules bound to the metal complexes, favoring grain growth [5].

18
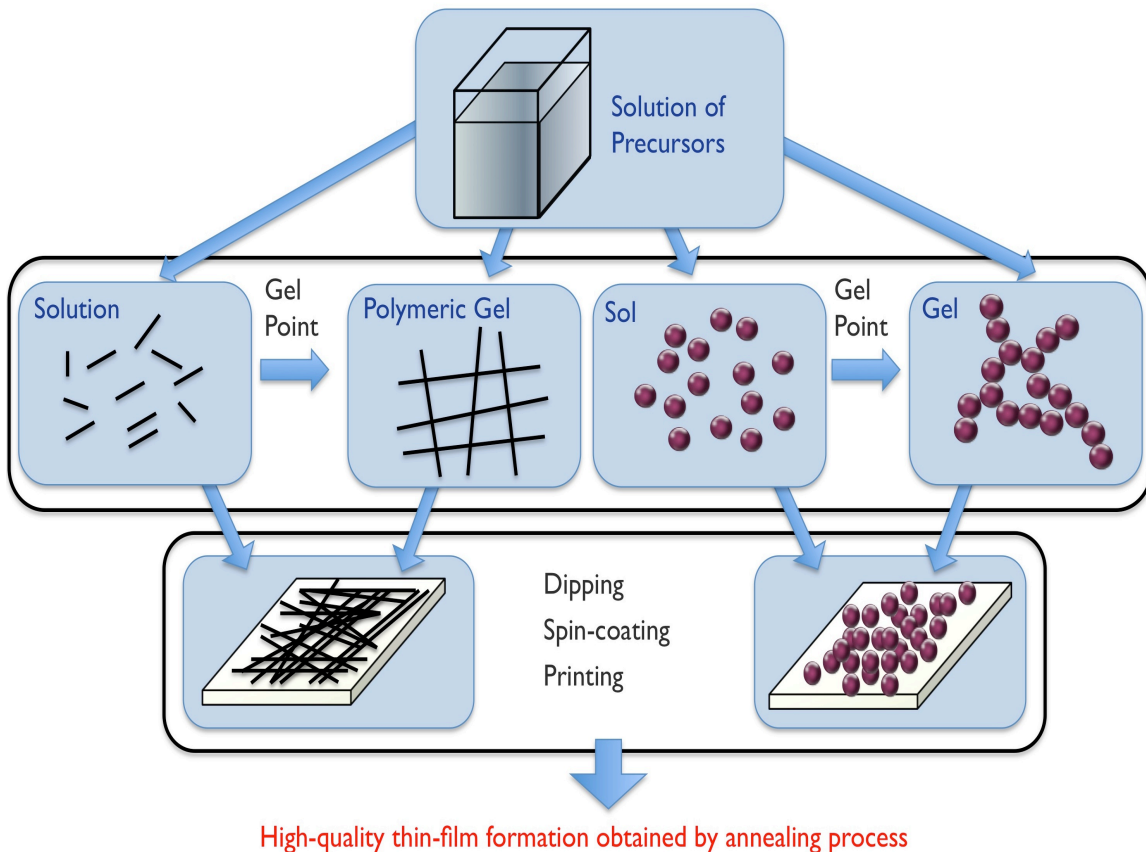
Figure 2.1 Simplified chart of the sol-gel process.

2.1.3. Chemistry of precursor solutions

To use the liquid phase precursor as the inks for inkjet printing, a stable sol is needed. To do that, as the first step, we have to choose the suitable solution for each solid phase precursors. The polarity of solvents can be decided based on a molecular structure. A permanent dipole moment, a relative dielectric constant, and a molecule polarizability determine the characteristics of the molecular structure of polar non-aqueous solvents. A higher relative dielectric constant means that we can dissolve more polar solute due to the permanent dipole moment. In contrast, solvents with a low relative dielectric constant (< 20), can dissolve less polar solute. Table 2.1 presents the relative dielectric properties of frequently used solvents.

Solvent	ε_r	Dipole moment	Type
Acetone (C_3H_6O)	20.7	3.00	Aprotic
Acetic acid ($C_2H_4O_2$)	6.2	$0.99 \sim 1.50$	Protic
Water (H_2O)	78.5	1.85	Protic
Methanol (CH_3OH)	32.6	1.70	Protic
Ethanol (C_2H_5OH)	24.3	1.70	Protic
Diethyl ether ($C_4H_{10}O$)	4.3	1.15	Aprotic
Pyridine (C_5H_5N)	14.2	2.19	Aprotic

Table 2.1 List of frequently used solvents for sol-gel process
with their dielectric properties.

As observed in Table 2.1, many different solvents can be used as the major solvent for a sol-gel system. Here, ethanol is employed as the major solvent for all metal oxide systems. There is an intermediate phase, called alkoxide, where alcohol is used as the major solvent. Alkoxides are compounds with the chemical formula $M(OR)_z$; these compounds are the product of direct or indirect chemical reactions between a metal salt, M_mX_n, and an alcohol, ROH. In this system, the alkoxy group (-OH) contains oxygen, which can act as an electron pair donor for a neighboring metal, resulting in polymerization. In contrast to the solvation of a metal in pure water, the alkoxy group can form bridges easily between different metal atoms. Hydrolysis occurs if the chemical reaction proceeds in a wet environment or if water is added to the system. The chemical reaction can be expressed as

$$M(OR)_z + H_2O \rightarrow M(OH)(OR)_{z-1} + ROH \qquad (2.1)$$
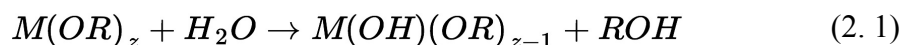
Another chemical reaction is condensation. Two complexes of M can chemically react with one another and form a polynuclear complex consisting of two metal atoms:

$$(-M-OH) + (-M-OR) \rightarrow M-O-M + ROH \qquad (2.2)$$

$$(-M-OR) + (-M-OR) \rightarrow M-O-M + ROR \qquad (2.3)$$
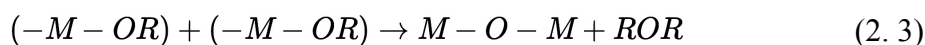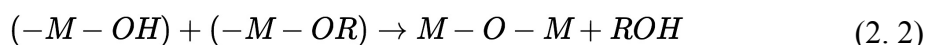
These two chemical reactions continuously proceed until one- or three-dimensional networks are formed. In the case of an alkoxide system, hydrolyzation and condensation processes occur so quickly that it is difficult to determine these intermediate phases. These intermediate phases precipitate if the rate of hydrolysis is extremely fast compared to the rate of condensation. The aforementioned intermediate phases, such as $M(OH)(OR)_{z-1}$, $(-M-O-M-)$ complexes or metal hydroxides $M(OH_m)$, can transform into desired M_xO_y by performing a high-temperature sintering process.

2.2. Ink-jet Printing Technology

As mentioned in the previous chapter, ink-jet printing technologies have several attractive features. They reduce waste, require less contact, use a wide range of solution-phase materials, and produce flexible and customizable patterns. As discussed above, metal oxide-based transparent electronics have been developed for next generation displays and solar cell systems. Additionally, the aforementioned liquid phase sol-gel precursors have been considered as the inks for printing, to take advantage of their properties, as well as for the large area and low cost of the process. To realize this vision, it is first necessary to understand the main mechanisms of stable droplet formation in inkjet systems. Secondly, the shapes of the deposited droplets should be predicted and controlled, based on the behavior of the droplets on the surfaces. These behaviors originate from several critical physical parameters, such as the droplet velocity, the ink viscosity, the surface tension, the boiling point, and the surface energy of the substrate. In this chapter, a representative ink-jet printing system will be introduced and the main mechanisms associated with the various printing-related phenomena will be explained. We will then discuss the conditions for the formation of stable droplets and the behaviors of the inks on the substrates.

2.2.1. Ink-jet printer nozzle technology

In ink-jet printing systems, the core part is the nozzle, generating drops by a pressure pulse. Depending on the method used to generate the pressure pulse, there are three alternatives for nozzle technologies: thermal bubble jets [7], electrostatic [8], and piezoelectric jets [9]. Thermal bubble jet method is the most successful technique used in desktop ink-jet printers and in industry. The schematics are illustrated in Figure 2.2. The There is a small heater inside the nozzle chamber. The temperature of this heater rises to 350-400°C, resulting in the vaporization of inks near this heater. This vaporization generates a bubble, inducing a pressure pulse that forces the drop though the nozzle. A very small drop size and a high nozzle density are achievable with this technique. However, the relatively high inner heater temperature leads to some disadvantages. In some cases, this higher temperature results in unexpected heated layers on top of the heater, leading to reduced efficiency and distorted ink fluids. In addition, all of the parts

and materials must tolerate the high temperatures.
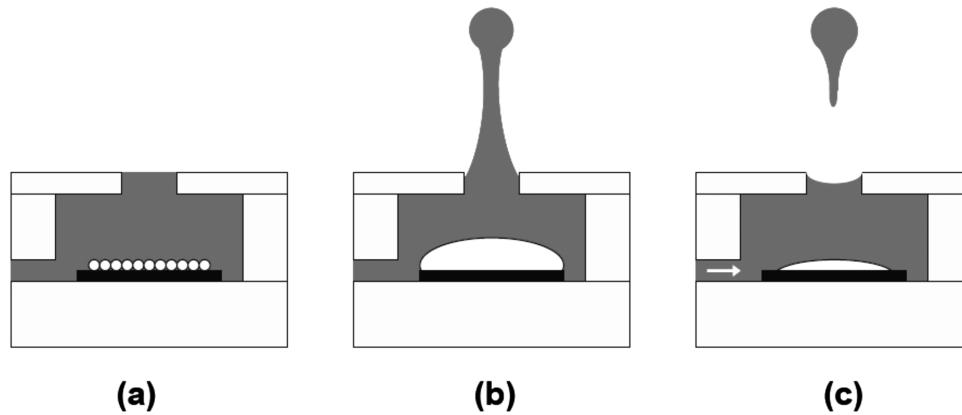

(a)   **(b)**   **(c)**

Figure 2.2 Operation cycle of a thermal bubble ink-jet device: nucleation occurs on the heater surface when the liquid temperature reaches a superheated temperature limit; bubble growth and liquid column ejected from ink-jet nozzle; and bubble collapse causes the droplet to break from the nozzle; at the same time, the chamber is refilled by capillary force [7].

The drop of ink can also be formed under the influence of an electrostatic field. The electrostatic force, exceeding the surface tension of the ink, forms a drop. These systems achieve a higher resolution than any other technique. The size of drops can be controlled by biasing voltages rather than by changing the real physical size of the orifice. However, the components are not inexpensive, and only conductive inks can be loaded inside the nozzle chamber. The setup is illustrated in Figure 2.3.

Finally, piezoelectric ink-jet technology is currently the most widely used system in this field. In this system, a small chamber is surrounded with a piezoelectric material. Applying an AC voltage to the piezo membrane produces a change in the volume of the chamber by mechanical distortion and creates the drop. The fast actuation of the piezoelectric materials (on the order of microseconds) means that the system can jet faster and is free from thermal stress on the inks. A wider range of inks can be used for an ink-jet printing system. For these reasons, all of the ink-jet printing investigations in this research were performed with piezoelectric nozzles loaded on an ink-jet printing system.
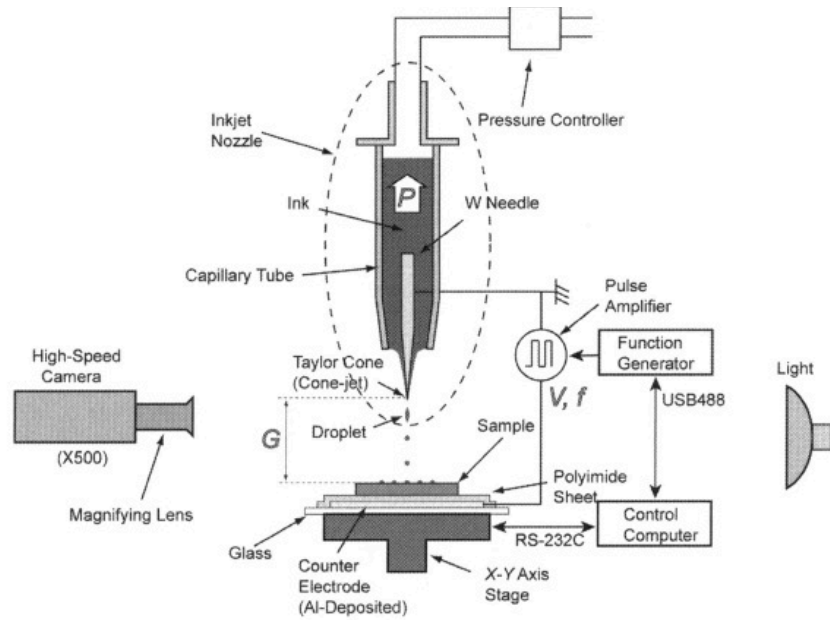
Figure 2.3 Set-up and schematic of the electrostatic ink-jet printing system [8].

2.2.2. Custom-built ink-jet printing system

Figure 2.4 presents a schematic and photograph of our custom ink-jet printer, consisting of a single Microfab piezoelectric ink-jet nozzle with a high-precision moving stage [9]. A side camera was installed to inspect the meniscus and drop stability and velocity. Another camera was used to monitor the patterns on the substrates. Most commercial ink-jet systems use water-based ink. Thus, a specific pressure control system is not critical. However, in this Microfab nozzle, a variety of different inks can be used with different wetting properties. Therefore, a specific pressure control system is needed to maintain the proper meniscus for jetting. Here, the installed main pressure regulator and the two needle values can control pressure from 2 to 40 psi.

This testbed also provides the ability to print on a variety of substrates, such as Si, glass rigid substrates, and flexible plastic substrates. The stage can be elevated to a temperature of 250°C and contains a water-cooling circulation system. Heater and water-cooling circulation systems are installed on the nozzle holder to control the viscosity of the loaded inks to maintain stable jetting. The high-temperature heating system is needed to control the morphology of drops to make a uniform pattern without the coffee ring effect. These issues are discussed below.

The patterns were formed based on a raster scan method in both the X and Y directions with a stage that has a precision of approximately 1 μm in both directions and a rotational stepper motor with an angular precision of 0.5 arc minutes. While printing, the distance between the nozzle and substrates can be controlled and nozzles with different orifice diameters can be used. The size of the orifice diameter is related to the volume of the drops. The drop volume is another parameter that controls the morphology of the dropped ink. The ink delivery path and glass nozzle were composed of chemically resistant materials, robust against several solvents, such as toluene, IPA, or ethanol, which is a major solvent used for sol-gel processed electrodes, semiconductors, and insulators.
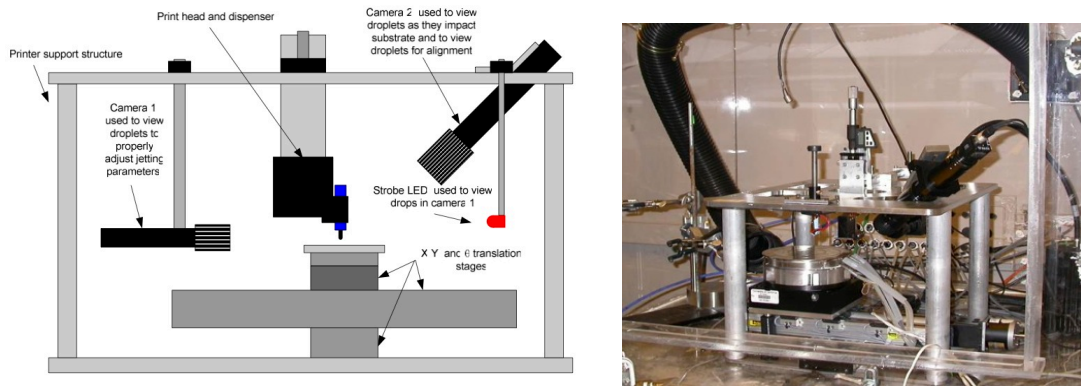

Figure 2.4 Schematic and photograph of the custom built ink-jet printer system, consisting of a single Microfab piezoelectric ink-jet nozzle with a high-precision moving stage [9].

Piezoelectric ink-jet dispensers typically use a unipolar or bipolar voltage waveform to form the drops. Figure 2.5 presents the bipolar wave, and Figure 2.6 presents an illustration of the pressure wave propagation in a piezoelectric dispenser. Firstly, the squeezed chamber induced by the positive voltage step results in a negative pressure (Figure 2.6(a)) and a split of the pressure wave (Figure 2.6(b)). As the pressure wave moves, it is reflected at the open side (supply) and at the closed end (nozzle), (Figure 2.6(c)). If the voltage steps down to zero, a new identical pressure distribution is formed, excepting for its sign (Figure 2.6(d). After $t_0+3l/2c$, where l is the length of chamber and c is the speed of sound in the fluid, the drop ejects (Figure 2.6(f)). The optimum time before biasing the negative voltage to eliminate the negative pressure wave or double the reflective positive pressure wave is the dwell time. If there is no more applied voltage step, sequential pressure waves will occur (Figure 2.6 (g-k)), resulting in unwanted periodic drop ejection. By generating additional negative pressure waves, it is possible to damp out with the final positive pressure wave so that it will not generate

additional drops after that point. The time between these negative and the last positive contractions is termed the echo time. In practice, a variety of different inks with different solvents can be used by controlling the parameters, such as the positive and negative biased voltages, dwell time, echo time, and ramp rates. Although it is an extremely flexible system, determining the optimized conditions for different ink systems requires considerable effort.
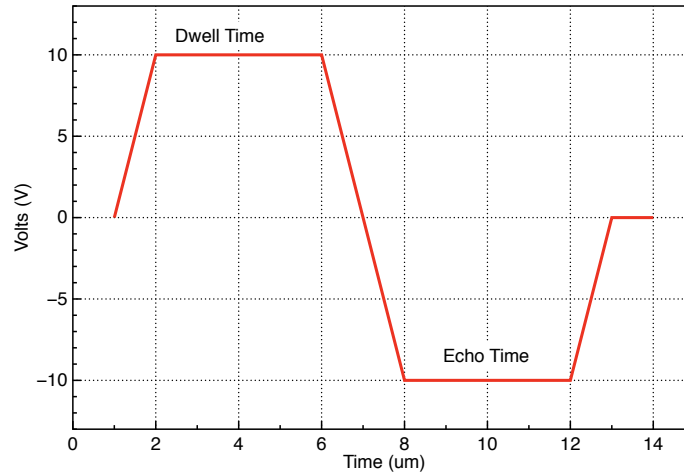

Figure 2.5 Example of the bipolar voltage waveform and definitions of dwell time and echo time.
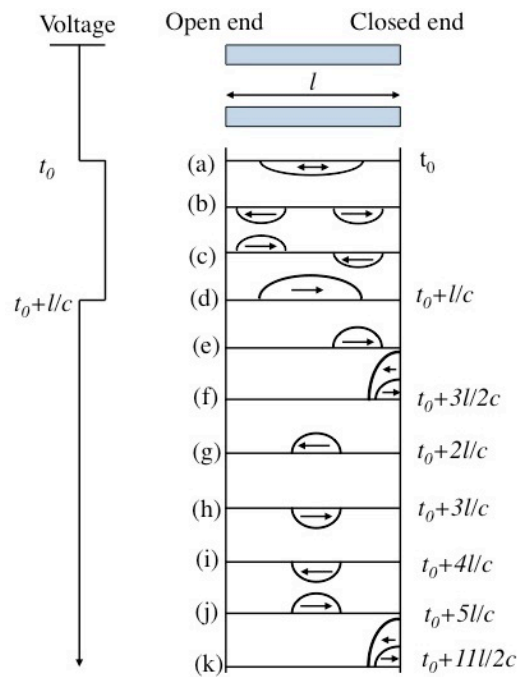

Figure 2.6 Illustration of pressure wave propagation in a piezoelectric dispenser.

25

2.3. Behavior of liquid drops

To generate the stable drops, several physical parameters, such as viscosity, orifice diameter, velocity, and biased voltages, are changed for different ink systems. The physics and fluid mechanics of the generated drops affect the initial drop shape when the drops make contact with the substrate. The behavior of the liquid drops can be explained with several dimensionless physical constants, such as the Reynolds (*Re*), Weber (*We*), and Ohnesorge (*Oh*) numbers:

$$Re = \frac{v\rho a}{\eta} \qquad (2.4)$$

$$We = \frac{v^2 \rho a}{\gamma} \qquad (2.5)$$

$$Oh = \frac{\sqrt{We}}{Re} = \frac{\eta}{\sqrt{\gamma \rho a}} \qquad (2.6)$$

where ρ, η, and Υ are the density, viscosity, and surface tension of the prepared inks, respectively. The term v is the velocity of the generated drops, and a is a characteristic length. Fromm, Reis, and Derby recently suggested a new parameter to confirm the stable jetting condition, Z ($Z=1/Oh$) [9, 10]. They suggested that the optimized Z number for stable jetting should lie within the following range: $1 < Z < 10$. The loaded inks are too viscous to generate the drops if the Z number is too low, whereas unwanted satellite drops are also generated around a major drop if the Z number is too high. Figure 2.7 presents the range of Z values that can be used in an ink-jet system. The validity of this predictable regime has been investigated with different ink systems [11]. In some cases, the optimized regime is near this regime but not contained in it. However, it is still helpful to narrow the conditions for ink property selection.

We also consider the dominant forces for the behavior of liquid drops to understand the main mechanism. There are three major forces that determine this behavior: gravitational force, inertial force, and capillary forces. The effect of gravitational force can be confirmed by calculating the Bond number, $B = \rho g a^2 / \Upsilon$, where g is the acceleration of gravity. Normally, this value is negligible an ink-jet printing system. We can ignore the gravitational force. Thus, the major forces are the inertial and capillary forces. There are two main regimes corresponding to the behavior of drops on impact. These regimes can be defined by the values of *We* numbers [12]. If the *We* number is larger than one, this regime is the inertial-force-dominant regime, originating from the high velocity of jetted drops. If the *We* number is smaller than one, this regime is the capillary-force-dominant regime. In the capillary-force-dominant regime, the velocity of jetted drops is not a critical factor. In addition, the physical parameter of

resistance to spreading is considered through the *Oh* number, defining the inviscid and highly viscous regimes. Figure 2.8 illustrates these relationships.
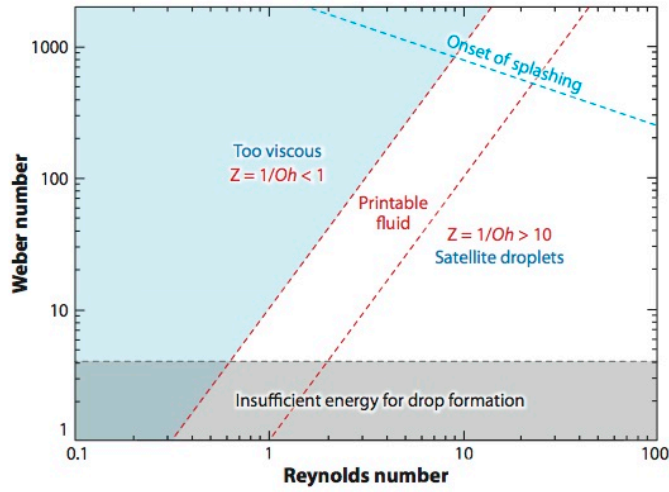

Figure 2.7 Regime of the fluid property for a stable ink-jet print system [13].
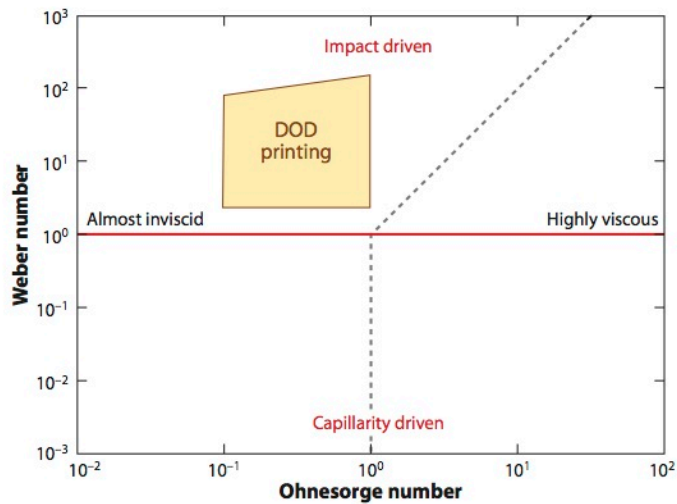

Figure 2.8 Major force for the behavior of liquid drops and the physical resistance factor to spring of dropped inks [12]

Jetted drops exhibit different behaviors land on the substrates corresponding to the aforementioned numbers and time, such as impact-driven spreading, recoil, or oscillation. These processes are illustrated in Figure 2.9. The spreading and oscillation behavior are initially limited by the viscosity, and the surface tension is a more dominant factor in controlling the behavior of liquid inks. Over time, the oscillation is dampened and the capillary forces begin to dominate. The size of the printed drop at the final stage can be taken as a part of a sphere:

$$d_{contact} = d_0 \sqrt[3]{\frac{8}{tan \frac{\theta_{eqm}}{2} (3 + tan^2(\frac{theta_{eqm}}{2}))}} \qquad (2.7)$$

Equation 2.7 indicates that the final feature and pattern shape are controlled by the contact angle, which is related to the wetting characteristics on the surface of the substrates. Figure 2.10 illustrates the two representative wetting cases (partial wetting and total wetting) [14]. When the spreading parameter, S, has a negative value, the deposited drops ideally form spherical caps on the substrates with an equilibrium contact angle θ_{eqm}. In contrast, when the spreading parameter has a positive value, the deposited drops spread completely to minimize the surface energy. This case is suitable for very thin insulators and semiconductors.
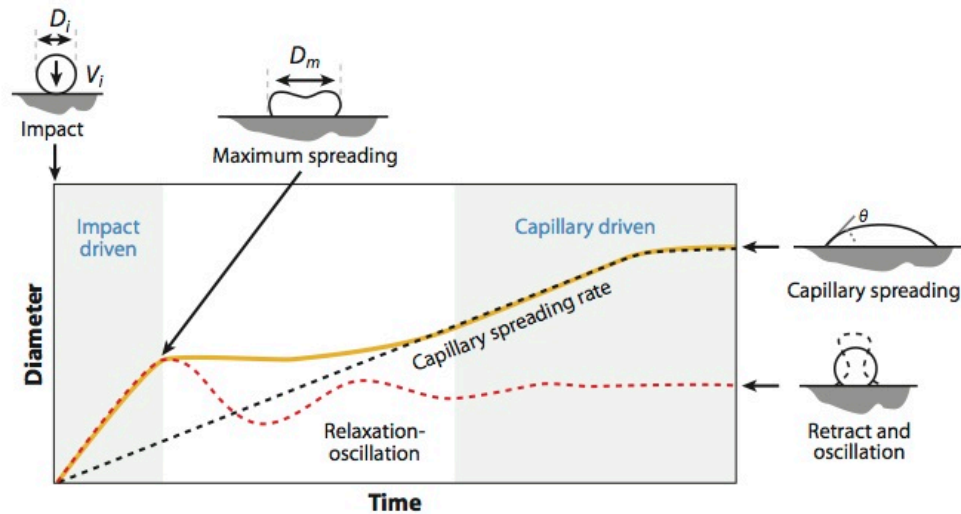

Figure 2.9 Schematic of the sequence of events that occur, after the drops land on the substrates [13].
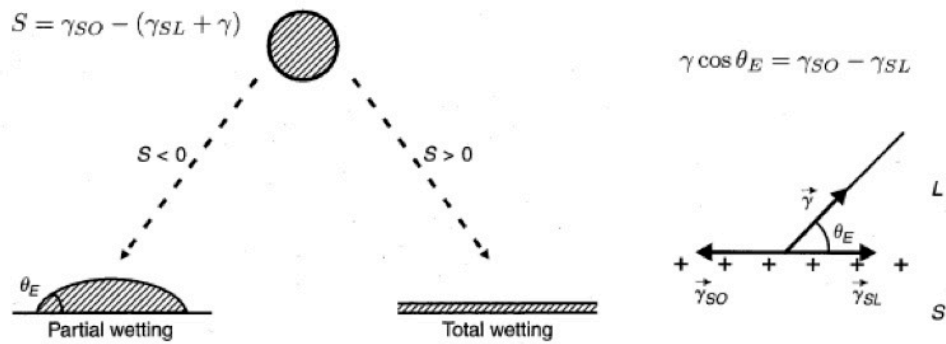
Figure 2.10 Two representative wetting conditions and the equilibrium contact angle equation based on Young's relationship [14].

However, the increased surface tension between the substrate and inks reduces the contact angle. This reduced contact angle leads to a decrease in the distance between the inks and substrates, resulting in faster evaporation at the rims. This process intensifies the outward radial flow to replenish the loss of the evaporated solvent. Finally, deposition occurs at the rims at the contact line. This phenomenon is known as the coffee ring effect [15]. The coffee ring effect must be avoided when fabricating integrated circuits connected to each unit transistor through interconnection lines or three-dimensional stacked structures because uniform layers are required. Several methods have been introduced to avoid the coffee ring effect. First, cooling the substrate can minimize the evaporation rate at the rim, more than that in the center area, thus delaying the outward flow [16]. Second, adding more solvent is also helpful to avoid the coffee ring effect. If the added solvent has a higher boiling point and lower surface tension than the major solvent, the solvent at the rim has a lower surface tension than in the center area. This lower surface tension at the rim causes a surface tension gradient, resulting in inward Marangoni flows [17]. The last effect is from increasing the substrate temperature. The increased substrate temperature can convert the pure liquid-phase inks into highly viscous gels. Such high viscosity reduces the spreading speed of the deposited inks, resulting in layers that do not exhibit the coffee ring effect [18].

2.4. Model for poly-crystalline TFTs

Thin-film transistors are typically analyzed based on the conventional single-

crystalline MOSFET theory. Several assumptions are required for such an analysis: (1) the channel mobility is constant; (2) the flat-band voltage is significantly smaller than the threshold voltage and can thus be neglected; (3) the distribution of the charge concentration is uniform along the channel; and (4) the thickness of the semiconductor is considerably less than the channel length.

A cross-sectional image of the simple basic structure of a thin-film transistor is presented in Figure 2.11. The channel length and width are in the y- and z-directions, respectively. The depth of the semiconductor channel is in the x-direction.
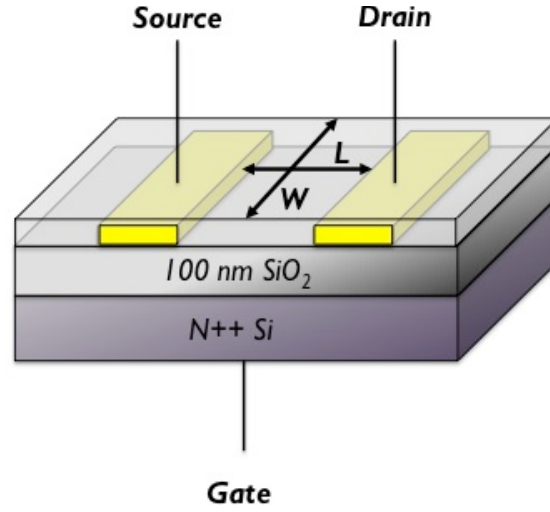
Figure 2.11 Cross-section of a typical bottom-gate TFT device.

There are two operation regimes: the linear regime (Vgs >> Vds) and the saturation regime (Vgs < Vds). In the linear regime, the channel resistance is expressed by

$$dR = \frac{1}{W\mu Q(y)}\, dy \tag{2.8}$$

where W is the channel width, μ is the mobility and $Q(x)$ is the surface charge density at y. In contrast to conventional MOSFET theory, Horowitz and co-workers recently introduced a new approach [19]. They defined two different charge factors (i.e., the bulk charge and the induced charge). The bulk charge is the surface charge density originating from the free charge carrier density inside the semiconductor material at equilibrium (n_0), where d_s is the thickness of the semiconductor.

$$Q_0 = qn_0d_s \tag{2.9}$$

When the gate voltage is biased, an accumulation layer is formed. At this moment, the induced charged in the accumulation layer is given by Equation 2.10.

30

$$Q_{induced} = C_i(Vg - V_{FB} - V(y)) \qquad (2.\,10)$$

where W and L are the channel width and length, respectively; C_i is the capacitance per unit area; V_{FB} is the flat band voltage and *V(y)* is the voltage drop through the channel area.

If the channel length is much larger than the thickness of the semiconductor (*L* >> d_s), a gradual channel approximation can be applied and *V(y)* is proportional to the distance between *y* and the source. The drain current (*Id*) is thus equal to *dV/dR*, and then *dV* can be express as follows:

$$dV = I_d dR = \frac{I_d}{W\mu(Q_{induced}(y) + Q_0)}\,dy \qquad (2.\,11)$$

By integrating Equation 2.11 (from the source to the drain) with Equations 2.9 and 2.10, we can derive Equation 2.11.

$$I_d \int_0^L dy = I_d L = W \int_0^{V_d} \mu(C_i(Vg - V_{FB} - V(y)) + qn_0 d_s)dV$$

$$I_d = \mu C_i \frac{W}{L}\left((Vg - V_0)V_d - \frac{V_d^2}{2}\right), V_0 = \frac{qn_0 d_s}{C_i} + V_{FB} \qquad (2.\,11)$$

Equation 2.11 is similar to the conventional MOSFET equation in the linear regime, excluding the V_0 term, which corresponds to *Vth*.

In the saturation regime, a depletion region is formed near the drain electrode. The depletion region decreases the effective channel thickness. The conductivity of depletion region can be estimated by the bulk conductivity, corresponding to the reduced effective channel thickness as follows:

$$I_d = Wqn_o\mu(d_s - W(y))dV \qquad (2.\,12)$$

The thickness of the depletion region is

$$W(V) = \frac{\varepsilon_s}{C_i}\left[\sqrt{1 + \frac{2C_i^2(V(y) - Vg)}{qN\varepsilon_s}} - 1\right] \qquad (2.\,13)$$

where ε_s is the dielectric constant of the semiconductor and N is the major carrier concentration. In the saturation regime (between the source and the drain), there are two regimes: an accumulation regime and a depletion regime near the drain electrode. Thus, Equation 2.11 is converted to the following equation.

$$I_d L = W \int_0^{V_g} \mu(C_i(Vg - V))dV + W\mu q n_0 \int_{V_g}^{V_{dsat}} (d_s - V_d(V))dV \quad (2.14)$$

If the depletion region at the drain is fully depleted and the insulator capacitance is much smaller than the capacitance of the semiconductor layer, the saturation current equation proposed by Horowitz and co-workers is as follows. Equation 2.15 is also similar to the conventional MOSFET equation in the saturation regime, excluding the V_0 term, which corresponds to *Vth*.

$$I_{dsat} = \frac{W}{2L} \mu C_i (Vg - V_0)^2 \quad (2.15)$$

Figure 2.12 presents sample TFT Id-Vds (a) and Id-Vgs (b) curves. The measured devices consist of printed Sb-doped SnO_2 electrodes and printed SnO_2 semiconductor on thermally grown 100 nm thick SiO_2/Si substrates. The specific fabrication process and electrical characteristics are discussed in chapter 4. Figure 2.12 (b) also shows the saturation drain current as a function of the gate bias. The threshold voltage was extrapolated, and the extracted threshold voltage is still ambiguous. Based on conventional MOSFET theory, the threshold voltage is the minimum required voltage to change into the on state. The extracted saturation field effect mobility is approximately 3.0 cm²/Vs; the threshold voltage is approximately -18 V based on Equation 2.2. Even though the threshold voltage can be extrapolated, the physical meaning of the extracted threshold voltage is still ambiguous. Based on the conventional MOSFET theory, the threshold voltage is the minimum required voltage to form conducting channels. The drain current of thin film transistors consisting of poly crystalline materials, is governed by defects. At low gate voltage (Von < Vg << Vth), the induced charges are almost entirely trapped by defects. As the gate bias voltage increases, some induced free carriers are partially trapped (interface trap states) and participate in conduction through thermionic processes, resulting in significant current (diffusion current). At higher Vg (Von << Vg < Vth), the electrons are released from deep strap states and following the power law compact model (drift current). Based on this reason, below Vth, the drain current is relatively significant, comparing to single crystal based conventional transistors.
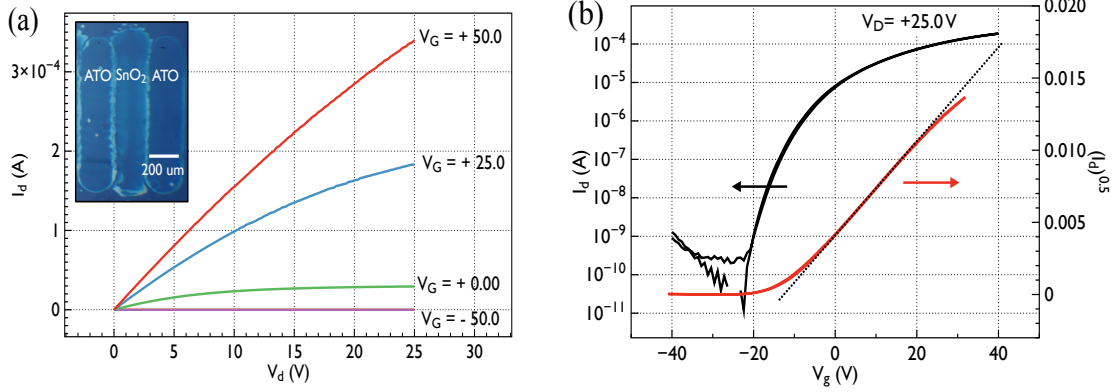
Figure 2.12 Representative electrical characteristics of the printed ATO S/D and the printed SnO$_2$-based devices on SiO$_2$/Si substrates: (a) I$_d$-V$_d$ and (b) I$_d$-V$_g$ (left axis) and I$_d^{0.5}$-V$_g$ (right axis).

The semiconductor thickness is one of the important parameters used to determine the performance of thin-film transistors. A considerably higher drain voltage is needed to obtain a thicker depletion region. These trends are similar to those of the thin-film transistors consisting of higher-carrier-concentration semiconductors. As the concentration increases, it provides more free carriers after filling the interface traps between the semiconductor and insulator. A more narrow depletion region is formed under the same conditions. A higher Vds is needed to achieve the saturation drain current. If the depletion layer does not extend over the whole semiconductor layer, near the drain, the off current is governed by the bulk conductivity originating from the reduced d_s. This can also be expressed by Equation 2.12. In contrast, if the depletion layer extends over the whole semiconductor, the I$_{off}$ is the drain current at V$_{on}$ = V$_{FB}$, I_{off} can be expressed as: [20]. We can use the new parameter, V$_{on}$, (abruptly increased drain current at V$_{on}$).

$$I_{off} = \mu\, \frac{kT}{q}\, \left(\frac{W}{L}\right)(qT_s n_{fi})(1 - exp(-\frac{qVd}{kT}))$$

(2. 16)

where T_s is the thickness of semiconductor, and n_{fi} is the electron density at V$_{FB}$.

2.5. Charge transport models: Extended state conduction mechanism

The effective field effect mobility in the extended state model is based on the ratio of free carriers and trapped carriers. The ratio of trapped carriers is established by the trap density and the intrinsic or injected charge carrier number. The trapped charges can be

activated easily into an extended state by thermal energy. Several extended transfer models were suggested to explain the transfer of the major carrier of a thin-film transistor. These models are presented below.

2.5.1. Mobility edge model

The mobility edge model was introduced by the paper from Salleo [21]. In this model, there are only two types of carriers: mobile carriers and trapped carriers. The mobile carriers are induced carriers due to the gate bias voltage that are formed inside defect free grains, and trapped carriers, which are carriers trapped by trap states located in grain boundary, assuming that all defects are localized inside the grain boundaries without considering the hopping process between trap states. As the gate bias voltage increases, more charge carriers are induced and move into the accumulation layer. The induced carrier in the accumulation layer fills up the trap, and then, the distribution of electrons changes into the conventional band-like DOS. The gate bias voltage and number of mobile charge carriers increase, resulting in high conductivity. The effective mobility can be expressed by

$$\mu_{eff}(Vg, T) = \mu_0 \frac{N_{mob}}{N_{tot}}$$
(2. 17)

where μ_0 is the constant intrinsic mobility, N_{mob} is the mobile charge carriers in the band, and N_{tot} is the total concentration of tail states. The drain current of a thin-film transistor in the linear regime can be expressed by

$$I_d = \frac{W}{L} \mu_{eff}(Vg, T) \cdot Vds \cdot N_{tot} = \frac{W}{L} \mu_{eff} C_i (Vg - Von)$$
(2. 18)

Based on Equations 2.17 and 2.18, the field effect mobility is affected by two parameters: the gate bias voltage and operation temperature. The shift of the Fermi energy level by biasing the gate voltage increases the carrier population in the conduction band. Additionally, with an increase in the operation temperature, a change in the Fermi-Dirac distribution width results in an increase in the probability of occupation. This model is simple and well matched with the experimental results [22]. Although temperature is an important parameter in Equation 2.18, there is no temperature term in the model. Definitely, there are two different types of traps: shallow and deep traps. Considering them, the equation used in the mobility edge model includes two exponential terms originates from shallow and deep traps. At a zero gate bias voltage, the Fermi energy level is located further in the band gap. The deep trap is a more important factor to make

current flow. Figure 2.13 presents one example of double exponential tails. Finally, the polaron property is also included in the aforementioned mobility edge model. The disorder polaron activation energy term is added based on the dynamic vibronic model [22], which assumes that the polaron effect is only related to the activation energy, resulting in a temperature-dependent mobility property. This effect does not affect the gate dependence of the mobility, which is affected by the disorder:

$$\mu_{eff}(Vg, T) = \mu_0 exp(\frac{-E_a}{K_b T}) \frac{N_{mob}(Vg, T)}{N_{tot}} \qquad (2.19)$$

where k_B is Boltzmann's constant.
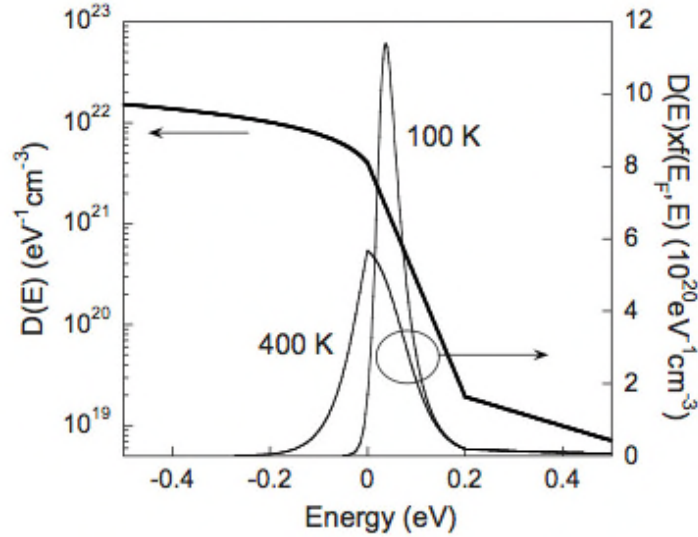
Figure 2.13 DOS of a polymer for the ME model and a carrier density at 400 K and 100 K extracted from fitting the p-type 270-kD P3HT transistor [22].

2.5.2. Multiple trapping and thermal release (MTR) model

In crystalline semiconductor, such as Si, the impurities generate localized states in the band gap. These states capture carriers frequently. The trapped carriers stay in there for relaxation time. The trapped carriers can be released by thermal energy or be

recombined. However, normally in amorphous silicon or organic materials, the carriers are trapped and de-trapped frequently, the density of localized states are relatively dominant, comparing to the carrier density. If there are only trap sites with one energy state, Et, and density, Nt, there are two pathways for carriers: trapped in trap sites or released into the conduction band by thermal energy. The carriers in the conduction band can be transferred by an externally biased electric field. The total induced carriers are partially trapped, and the remainder work as free carriers. The concentrations of free and trapped carriers are, respectively, expressed as

$$n_f = N_c exp(-\frac{E_c - E_f}{k_b T}) \tag{2.20}$$

$$n_t = N_t exp(-\frac{E_t - E_f}{k_b T}) \tag{2.21}$$

Using Equations 2.20 and 2.21, the field effect mobility is expressed as in Equation 2.22

$$\mu_{eff} = \mu_0 \frac{n_f}{n_f + n_t} = \mu_0 \frac{N_t}{N_c} exp(-\frac{E_c - E_t}{k_b T}) \tag{2.22}$$

Unfortunately, the gate-dependent field effect mobility of thin-film transistors cannot be explained using Equation 2.22. Thus, the energy distribution of traps should be considered and included as follows:

$$D(E) = \frac{N_t}{k_b T_C} exp(-\frac{E}{kT_c}), E > 0 \tag{2.23}$$

The total density of trap states is higher than the density of charge carriers by a biased gate voltage.

$$n_t = N_t exp(-\frac{E_f}{k_b T_c}) = \frac{C_i(V_g - V_o)}{q} \tag{2.24}$$

$$E_f = -k_b T_c(\frac{C_i(V_g - V_o)}{q N_t}) \tag{2.25}$$

The density of free charges is

$$n_f = \int_{E_f}^{\propto} D(E) exp\left(-\frac{E}{k_b T}\right) dE = \frac{N_t}{1+\frac{T_c}{T}} \left(\frac{C_i(V_g - V_o)}{qN_t}\right)^{\frac{T_c}{T}+1} \qquad (2.26)$$

Then, the effective mobility is expressed as follows for $n_t >> n_f$:

$$\mu_{eff} = \mu_o \frac{n_f}{n_t} = \mu_0 \frac{N_t}{1+\frac{T_c}{T}} \left(\frac{C_i(V_g - V_o)}{qN_t}\right)^{\frac{T_c}{T}-1} / \left(\frac{C_i(V_g - V_o)}{q}\right)$$

$$= \mu_0 \frac{N_t}{1+\frac{T_c}{T}} \left(\frac{C_i(V_g - V_o)}{qN_t}\right)^{\frac{T_c}{T}} \qquad (2.27)$$

The field effect mobility is affected by both the operation temperature and gate bias voltage.

The aforementioned suggested approaches are based on an organic material-based thin-film transistor. Similar approaches were conducted for amorphous, poly-silicon- and metal oxide-based thin-film transistors originating from the same theory [24, 25]. The AIM-Spice level 15 model is typically used for the above-threshold regime. In this model, the drain current in the linear and saturation regimes is expressed as

$$I_d = \frac{K/V_{AA}^{\gamma}}{1 + R(L/V_{AA}^{\gamma})(V_g - V_{th})^{1+\gamma}} \times \frac{(V_g - V_o)^{1+\gamma} V_d (1 + \gamma V_d)}{[1 + (V_d/V_{d_{sat}})^m /^{1/m}]} \qquad (2.28)$$

where $K=(W/L)C_i \mu_0$, W is the channel width, L is the channel length, μ_0 is the band mobility, R is the contact resistance, Υ and V_{AA} are empirical parameters, m is the sharpness of the knee region, and λ is the channel length modulation parameter.

For low V_d (the linear regime), the intrinsic channel conductance g_{chi} is expressed as

$$g_{chi} = \frac{W}{L} C_i \mu_{FET} (V_g - V_{th}) = \frac{W}{L} C_i \mu_0 \frac{1}{V_{AA}^{\gamma}} (V_g - V_{th})^{1+\gamma} \qquad (2.29)$$

37

For low Vd (the linear regime), the drain current can be written as

$$I_{dlin} = \frac{K}{V_{AA}^\gamma} (Vg - Vth)^{1+\gamma} Vd$$

(2. 30)

The series resistances are another voltage drop component in the linear regime. Including these resistance effects, the channel conductance is expressed as

$$g_{chi} = \frac{g_{chi}}{1 + (R_S + R_D)g_{chi}}$$

(2. 31)

From Equations 2.29, 2.30, and 2.31, the driven drain current including contact resistances is written as

$$I_{dlin} = \frac{K/V_{AA}^\gamma}{a + R(K/V_{AA}^\gamma)(Vg - Vth)^{1+\gamma}} (Vg - Vth)^{1+\gamma} Vd$$

(2. 32)

According to Equation 2.28, at high Vd (the saturation regime), the drain current in the saturation regime can be expressed as

$$I_{dsat} = \frac{K}{V_{AA}^\gamma} \alpha(Vg - Vth)^{2+\gamma}$$

(2. 33)

where α_s is the saturation modulation parameter and is less than one.

In these systems, the field effect mobility increases with increasing gate bias, and the relationship can be expressed as

$$\mu_{FET} = \mu_0 \left(\frac{Vg - Vth}{V_{AA}}\right)^\gamma$$

(2. 34)

γ is $2(V_{nt}/V_{th})-2$, where V_{nt} is the characteristic slope of the conduction band tail and V_{th} is the thermal voltage [22]. In addition, when compared to Equation 2.27, γ also

corresponds to the T_c/T parameter. This parameter can be used to establish the film quality. If the Υ is close to zero, the field effect mobility is more independent of the biased gate voltage. The output characteristics of thin-film transistors follow the conventional square law model.

We also applied this model to fit experimental data from metal oxide semiconductor transistors in this thesis to confirm the validity of this model. The results are also compared with the experiment results, which is discussed in chapter 3. With this model, we can extract useful parameters to understand this system, such as concentration of localized states and the characteristic temperature; these parameters are intimately related to the performances of TFTs. The profile of the density of states comprising interface and deep trap states can also be described in a simplistic manner using this framework. The aforementioned model for amorphous, poly crystalline organic and inorganic semiconductor based TFTs is the critical key to understand, and useful to describe the operation characteristics of sol-gel processed poly-crystalline TFTs.

2.6. Summary

In this chapter, we introduced the sol-gel process and the basic theory used for the sol-gel process in this thesis work. Next, we discussed three representative alternatives for inkjet nozzle technologies, categorized based on the method to generate the pressure pulse. Several dimensionless physical constants, such as the Reynolds (*Re*), Weber (*We*), and Ohnesorge (*Oh*) numbers were introduced to explain the behavior of the drops during jetting. The surface morphology of drops and how this morphology is influenced by several parameters were explained, based on established theories. Finally, the basics of thin-film transistors were discussed. In addition, non-ideal transport models were also introduced, such as the mobility edge model and the MTR model for amorphous, poly crystalline organic and inorganic semiconductor based TFTs.

2.7. References

[1] S. E. Molesa, S. K. Volkman, D. R. Redinger, A. F. Vornbrock, and V. Subramanian, "A high-performance all-inkjetted organic transistor technology," in Electron Devices Meeting, 2004. IEDM Technical Digest. IEEE International, 2004, pp. 1072- 1074.

[2] J. Vaillancourt et al., "All ink-jet-printed carbon nanotube thin-film transistor on a polyimide substrate with an ultrahigh operating frequency of over 5 GHz," Applied Physics Letters, vol. 93, no. 24, p. 243301, 2008.

[3] S. Chung, J. Jang, J. Cho, C. Lee, S.-K. Kwon, and Y. Hong, "All-Inkjet-Printed Organic Thin-Film Transistors with Silver Gate, Source/Drain Electrodes," Japanese Journal of Applied Physics, vol. 50, no. 3, p. 03CB05, Mar. 2011.

[4] D. Redinger, S. Molesa, S. Yin, R. Farschi, and V. Subramanian, "An ink-jet-deposited passive component process for RFID," Electron Devices, IEEE Transactions on, vol. 51, no. 12, pp. 1978-1983, 2004.

[5] S. Suwanboon, S. Chukamnerd, U. Anglong, "Morphological control and optical properties of nanocrystalline ZnO powder from precipitation method," *J. Sci. Technol.*, vol. 29, pp. 1563-1570, 2007.

[6] T. Thirugnanam, "Effect of polymers (PEG and PVP) on sol-gel synthesis of microsized zinc oxide," Journal of nanomaterials, vol. 2013, pp. 1-7, 2013.

[7] Y. Wang, J. Bokor, "Ultra-high resolution monolithic thermal bubble inkjet print head," *J. Micro/Nanolith. MEMS MOEMS*, vol. 6, 043009, 2007.

[8] Y. Ishida, K. Sogabe, S. Kai, T. Asano, "Droplet election behavior in electrostatic inkjet driving," *Microprocesses and nanotechnology, 2007 digest of papers*, 384-385, 2007.

[9] S. E. Molesa, "Ultra los cost printed electronics," *Ph. D. Thesis*, University of California, Berkeley, 2006.

[9] J. E. Fromm, "Numnerical calculation of the fluid dynamics of drop-on-demand jets," *IBM J. Res. Dev.*, vol. 28, 322-333, 1984.

[10] N. Reis, B. Derby, " Ink jet deposition of ceramic suspensions: modeling and experiments of droplet formation," *MRS Symp. Proc.*, vol. 624, 65-70, 2000.

[11] B. Derby, N. Reis, "Inkjet printing of highly loaded particulate suspension, "*MRS Bull.*, vol. 28, 815-818, 2003.

[12] S. Schiaffino, A. A. Sonin, "Molten droplet deposition and solidification at low Weber number," *Phys. Fluids*, vol. 9, 3172-3187, 1997.

[13] B. Derby, "Inkjet printing of functional and structural materials: Fluid property requirements, feature stability, and resolution." *Annu. Rev. Mater. Res.*, vol. 40, 395-414, 2010.

[14] P. G. de Gennes, F. Brochard-Wyart, and D. Quéré, "Capillarity and wetting phenomena:drops, bubbles, pearls, waves", p. 16, Springer, 2004.

[15] R. D. Deegan, O. Bakajin, T. F. Dupont, G. Huber, S. R. Nagel, T. A. Witten, "Capilary flow as the cause of ring stains from dried liquid drops," *Nature*, vol. 389, 827-829, 1997.

[16] D. Soltman and V. Subramanian, "Inkjet-Printed Line Morphologies and Temperature Control of the Coffee Ring Effect," *Langmuir*, vol. 24, 2224-2231, 2008.

[17] D. Kim, S. Jeong, B. K. Park, and J. Moon, "Direct writing of silver conductive patterns: Improvement of film morphology and conductance by controlling solvent compositions," *Applied Physics Letters*, vol. 89, 264101, 2006.

[18] A. M. J. van den Berg, A. W. M. de Laat, P. J. Smith, J. Perelaer, U. S. Schubert, "Ceometric control of inkjet printed features using a gelating polymer," *J. Mater. Chem.*, vol. 17, 677-683, 2007.

[19] G. Horowitz, R. Hajlaoui, H. Bouchriha, E. Bourguiga, M. Hajlaoui, "The concept of threshold voltage in organic field effect transistors," *Adv. Mater.*, vol. 12, pp 923, 1998.

[20] S. Lee, S. Jeon, A. Nathan, "Modeling sub-threshold current-voltage characteristics in thin film transistors," *Journal of display technology*, vol. 9, pp. 883-339, 2013.

[21] A. Salleo, T. W. Chen, A. R. Völkel, Y. Wu, P. Liu, B. S. Ong, R. A. Street "Intrinsic hole mobility and trapping in a regioregular poly(thiophene)," *Phys. Rev. B*, vol. 70, 15311, 2004.

[22] J. F. Chang, H. Sirringhaus, "Relative importance of polaron activation and disorder on charge transport in high mobility conjugated polymer field effect transistors," *Physical review B (condensed matter and materials physics)*, vol. 76, 205204, 2007.

[23] H. Bassler, P. M. Borsenberger, R. J. Perry, "Charge transport in poly (methylpheneylsilane): The case for superimposed disorder and polaron effects," *Journal of polymer science part B: Polymer physics*, vol. 32, 1677-1685, 1994.

[24] P. Servati, D. Striakhilev, A. Nathan, "Above-threshold parameter extraction and modeling for amorphous silicon thin film transistrs," IEEE Trans. Electron Devices, vol. 50, 2227-2235, 2003.

[25] A. Ceredeira, M. Estrats, R. Garcia, A. O. Conde, F. J. Garcia Sanchez, "New procedure for the extraction of basic a-Si:H TFT model parameters in the linear and saturation regions," Solid State Electronics, vol. 45, 1077-1080, 2001.

Chapter 3 Fabrication and Electrical Characteristics of SnO_2 TFTs

3.1. Introduction

This chapter describes the fabrication process and operational characteristics of SnO_2 TFTs. TFT characteristics are normally affected by the quality of the semiconductor layer and the quality of the interface layer between the semiconductor and insulator layers. The crystallinity and the grain size are critical factors in determining the film quality, and the crystallinity and the crystalline orientation can affect the electrical characteristics as well. Highly crystalline and highly oriented thin films lead to higher-performance TFTs compared to randomly oriented thin-film-based TFTs. As the grain size increases, the number of grain boundaries per active channel layer decreases, resulting in better performance. In addition, the interface trap density at the semiconductor/insulator interface should also be considered when attempting to create high performance TFTs.

In the work described herein, we started with solution-phase sol-gel precursors to deposit the layers. According to the theory of sol-gel chemistry, the formed film can be affected by the addition of surfactants, acids and bases to the starting materials; the film quality is also affected by the temperature, time, and ambient conditions during the sintering process. To fabricate TFTs, we deposited semiconductor layers on underlying insulator layers. The post-formed crystal structure of the films is also affected by the structure of these underlying film structures.

The quality (crystallinity, and surface morphology) of sol-gel processed SnO_2 layers is evaluated by XRD and AFM as a function of sintering temperatures. In addition, the effect of NH_4OH addition on film crystallinity and morphology was also investigated, with different concentration of NH_4OH. The relationships between the semiconductor film quality and the electrical characteristics of the TFTs were studied. Finally, it is shown that the SnO_2 based transistors on sol-gel processed ZrO_2 insulators delivered better TFT performances. This result was attributed to improvement of interface quality, and overall film crystallinity.

3.2. SnO_2 precursor preparation and thin film formation

All reagents were purchased from Aldrich and used as received. To create a sol-gel semiconductor, a SnO_2 liquid precursor was prepared by dissolving 0.001 mol of $SnCl_2 2H_2O$ (99.995% pure) in 10 ml ethanol, which was then stirred with varying amounts of NH_4OH. The prepared glass and SiO_2/Si substrates were cleaned with acetone and DI-water, followed by 10 min of UV/Ozone treatment, before the SnO_2 thin films were deposited on the substrates. The SnO_2 samples for XRD measurements were deposited by drop-casting. For AFM and TFTs, the SnO_2 films were deposited by a spin-

casting process at 3000 rpm for 30 secs in air. All deposition processes were conducted within 20 mins, after preparing the SnO_2 precursors.

3.3. SnO_2 thin film characteristics

Figure 3.1 shows the XRD patterns as the function of post sintering process. Clear evidence of conversion to SnO_2 is apparent even at 350 ^oC from the corresponding to XRD peaks, which are well matched with the reference JCDPS data (41-1445). In addition, the crystallization studies show that strong crystallinity is developed at temperature or above 400 ^oC.
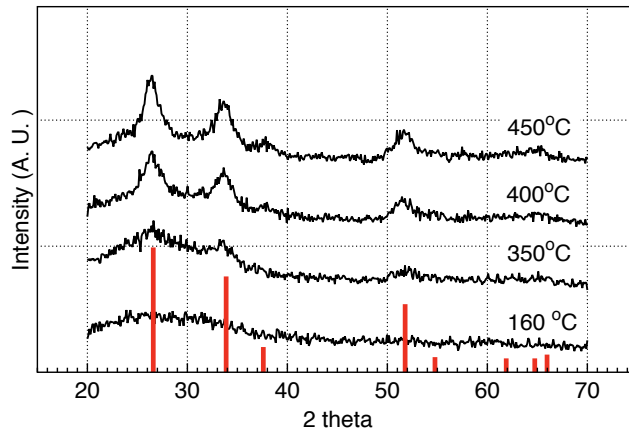

Figure 3.1 XRD spectra of SnO_2 films sintered at various temperatures for 1 hour in air. Note onset of strong crystallinity at 400 ^oC

The formation of thin metal oxide films from solution based precursors has been reported to depend on numerous variables, including the choice of precursors, solvent, aging time, acidity and catalysts [1]-[4]. It is found that the formation of a gel-phase in the precursor for this system is critical to obtaining high performance devices by adding NH_4OH into the $SnCl_2 2H_2O$ precursor in ethanol. In the case of 0.44 mmol NH_4OH addition, the crystallization temperature is depressed from 350 ^oC for sample without NH_4OH to only 200 ^oC for the samples with NH_4OH. It can be explained by the fact that a free OH^- nucleophilic ion originates from the NH_4OH and attacks one of the hydrogen atoms of water molecules bound to the metal complexes, facilitating lower temperature conversion [5], [6]. In the case of 0.88 mmol NH_4OH addition, especially, at 160 ^oC, the deposited films were not SnO_2, but $SnCl_6(NH_4)$.
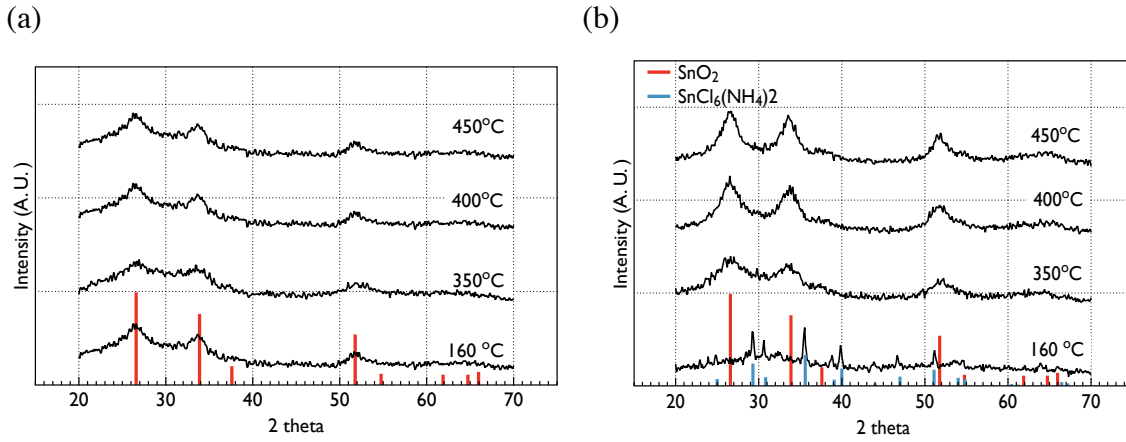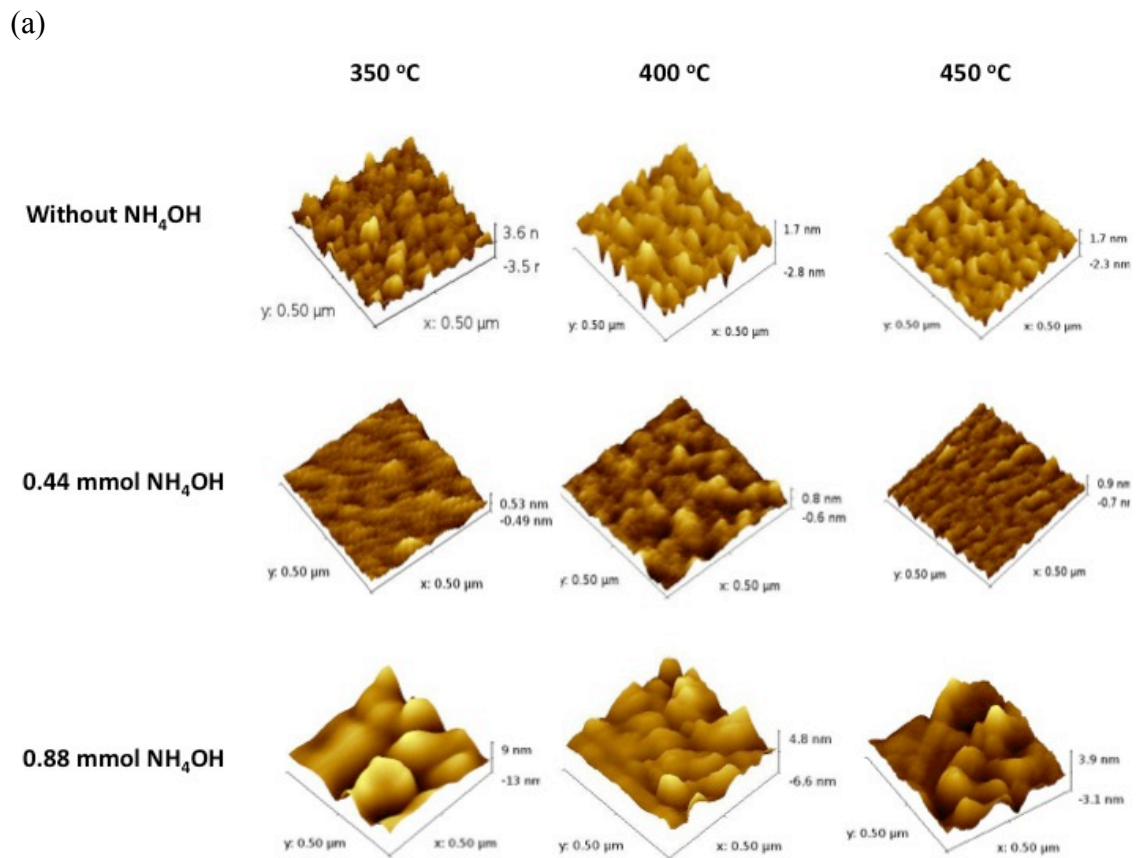
(a)

(b)

Figure 3.2 XRD spectra of SnO$_2$ films sintered at various temperatures for 1 hour in air. (a) 0.44 mmol NH$_4$OH addition and (b) 0.88 mml NH$_4$OH addition. The red and blue bars are corresponding to reference JCDPS reference data for SnO$_2$ and SnCl$_6$(NH$_4$)$_2$, respectively.
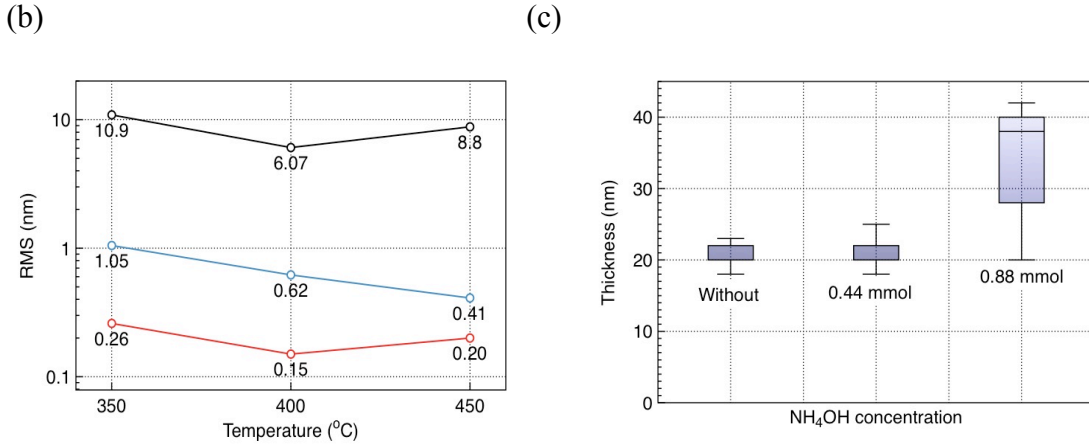

(a)

(b)   (c)

Figure 3.3 (a) The AFM images and (b) The average RMS values of sintered SnO_2 films with different post annealing temperature and different NH_4OH concentration. (c) The thickness distribution, corresponding to NH_4OH concentration.

The surface morphology was examined and RMS thickness variation values were also obtained by AFM, with different post annealing process and with different NH_4OH concentration in Figure 3.3. Without NH_4OH, some porosity is still evident in the films by atomic force microscopy, but continuous transport paths are clearly obtained. Potentially, even higher performance may be achievable in the future by eliminating the residual porosity. By adding 0.44 mmol NH_4OH, the porosity was not found and the smoothest SnO_2 films were obtained, regardless of sintering temperature. When more NH_4OH was added, 0.88 mmol, the prepared precursor solution was milky. Due to aggregated complexes formed by adding of 0.88 mmol NH_4OH, uniform layers cannot be deposited. The measured film thickness and RMS values were also obtained from AFM data, summarized in Figure 3.3 (b). The smoothest (RMS: 0.15 nm) and uniform SnO_2 films (Thickness: 20 nm) were formed by adding 0.44 mmol NH_4OH. Significant fluctuation in thickness and largest RMS values were obtained when 0.88 mmol NH_4OH was added.

The characteristics of the prepared precursor are important factors to decide the sintered film quality. The speed of chemical reaction, the energy to convert into the target materials, and stability, are representatively limited by the precursors, which is related to the crystalline size, chemical components and the process temperatures. At the precursor level, understanding of the rheology of precursor fluids is an indirect method to determine the phase of sol-gel precursors. As mentioned above, the sol contains colloidal particles. If the colloidal particles are inside the major liquid, particles increase their viscosity on stirring or shearing. This behavior occurs when the colloidal suspension changes into a state of flocculation from a stable solution. In contrast, polymer solutions with long entangled and looping molecular chains show Pseudo-plastic characteristics. There materials have irregular order and they have sizable internal resistance against flow.

45

In sol-gel system, the gel is a 1-dimensional or 3-dimentional interconnected structure, consisting of sols, like the polymer solution. The gel phase also has sizable internal resistance, originating from the 1-dimensional or 3-dimentional structures.
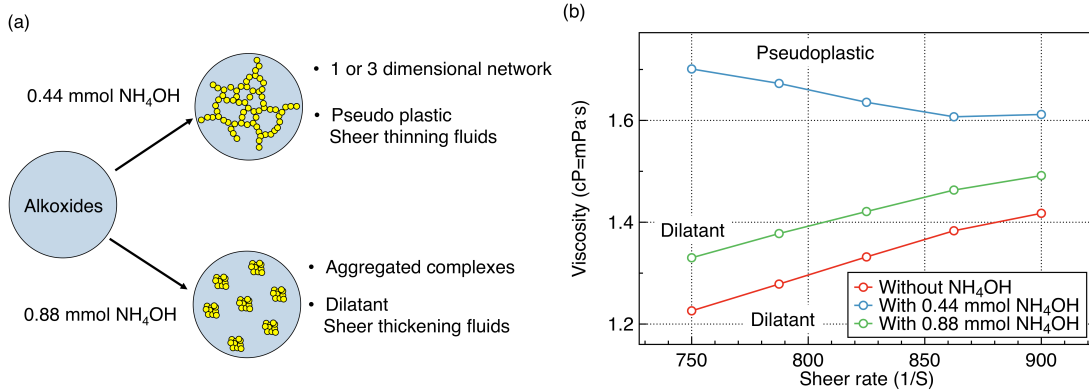

Figure 3.4 (a) Schematic of intermediate phases of sol-gel precursors: polymeric gel-like precursor formed by addition of 0.44 mmol NH_4OH, and aggregated complexes formed by addition of 0.88 mml NH_4OH. (b), viscosity versus sheer rate for prepared solution phase precursors for different NH_4OH concentrations.

The relationship between viscosity and sheer rate for different NH_4OH concentrations was investigated to understand the behavior of prepared precursor solutions and determine the phase of the prepared precursor solution. The schematic of the phases of the precursors was drawn in Figure 3.4 (a) and plotted in Figure 3.4 (b), respectively. Firstly, a free OH^- nucleophilic ion originates from the NH_4OH and attacks one of the hydrogen atoms of water molecules bound to the metal complexes, facilitating lower temperature conversion. In addition, the addition of 0.44 mmol NH_4OH results in a change of the phase of the precursor into a continuous 1 or 3-dimensional gel-like phase due to inter-aggregation by hydroxide bridges [7], [8]. The obtained rheological properties support the formation of a gel-like phase, based on the observation of pseudo-plastic flow in the NH_4OH-containing precursor vs. dilatant flow in the corresponding pure precursor solution and 0.88 mol NH_4OH added precursor solution [9].

3.4. SnO_2/SiO_2 thin film transistors

For initial evaluation, test devices were prepared on substrate-gated test structures consisting of Cr (5 nm)/Au (45 nm) source/drain electrodes (200 um channel width and

100 um channel length) deposited on thermally grown 100 nm SiO_2/n+ Si substrates. After a 10 min UV/Ozone surface treatment, the prepared SnO_2 precursor solution was spin-coated at 3000 rpm for 30 seconds, within 20 minutes, dried at 160 ^{o}C on a hotplate, and then annealed at temperatures ranging from 350°C ~ 450°C for 1 hour in air in a tube furnace. To minimize fringing current effects, the SnO_2 was patterned with a mechanically-controlled probe tip. This tip was dragged around each transistor, as close as possible to the contact pads and channel area, prior to the sintering process, to ensure complete film removal by mechanical abrasion. Figure 3.5 shows the schematic of the fabricated SnO_2 TFT on thermally grown 100 nm thick SiO_2/Si substrates.
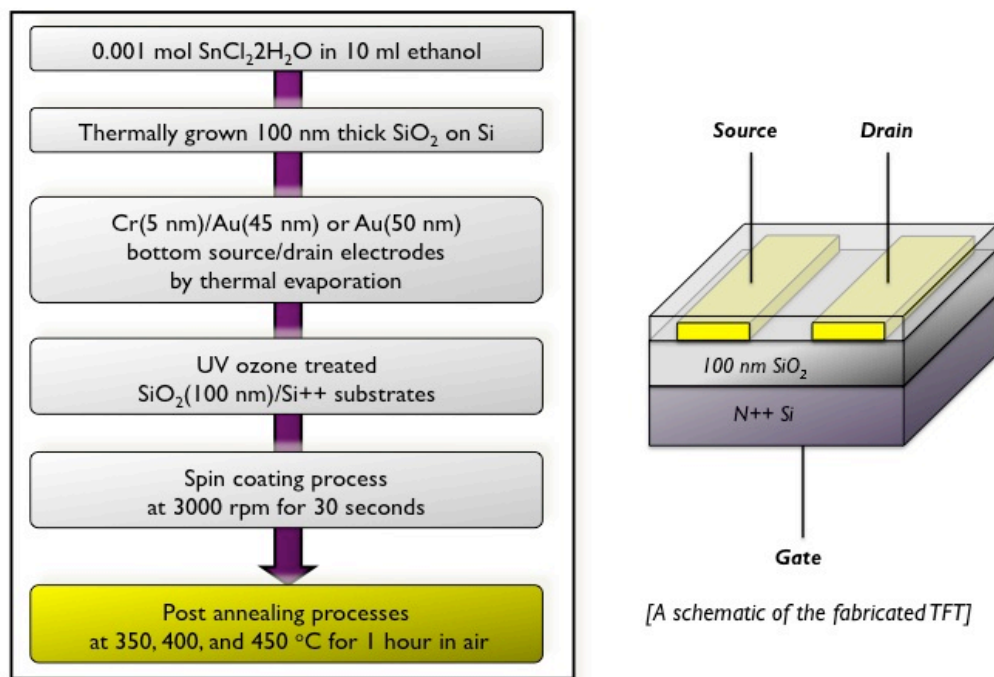

Figure 3.5 The fabrication flow of the test SnO_2 structure and schematic of the fabricated TFT

The measured electrical characteristics of the fabricated TFTs with the pristine SnO_2 precursor, under conditions of varying post annealing process temperature and channel length were measured. The obtained TFT parameters, such as field effect mobility in saturation regime, on/off current ratio and sub-threshold swing, were summarized in Figure 3.6. As channel length decreased, the field effect mobility in saturation regime and on/off current ratio decreased. In contrast, SS was increased. The increased off current, related to decreased on/off current ratio, and increased SS indicates less gate bias controllability. Note that unlike the field effect mobility in the linear

47

regime, the saturation mobility is largely unaffected by contact resistance. However, here, the extracted field effect mobility in the saturation regime also was affected by channel length. There is a clear monotonic relationship between crystallinity and field effect mobility. Figure 3.7 shows the representative electrical characteristics of a TFT with a channel length of 100 um and a width of 200 um. The extracted saturation field effect mobility was ~ 0.8 cm^2/Vs for devices processed at 350ºC, and increased to ~ 1.5 cm^2/Vs at 400 ºC, corresponding to the onset of crystallinity as observed via XRD [10]. The higher mobility was also obtained for devices annealed at 450ºC; however, there was a significant increase in leakage. We attribute this to increased carrier concentration in the SnO$_2$ film, resulting from oxygen vacancies generated by the high temperature annealing process [11], [12]. More conductive sintered SnO$_2$ films at 450 ºC make the gate controllability less.

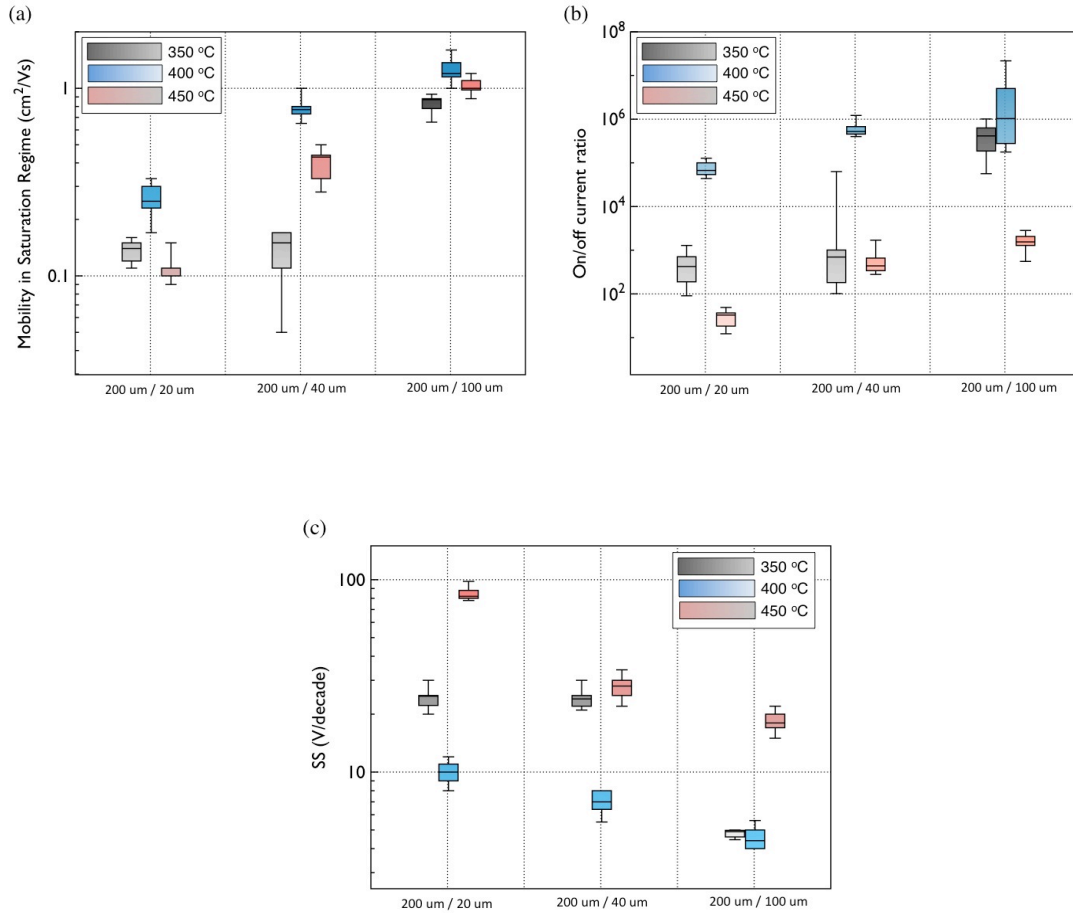Figure 3.6 The obtained parameters of the fabricated TFTs with the pristine SnO$_2$ precursor, varying a post annealing process temperature and with different channel length: (a) Field effect mobility in saturation regime, (b) On/off current ratio and (c) SS.
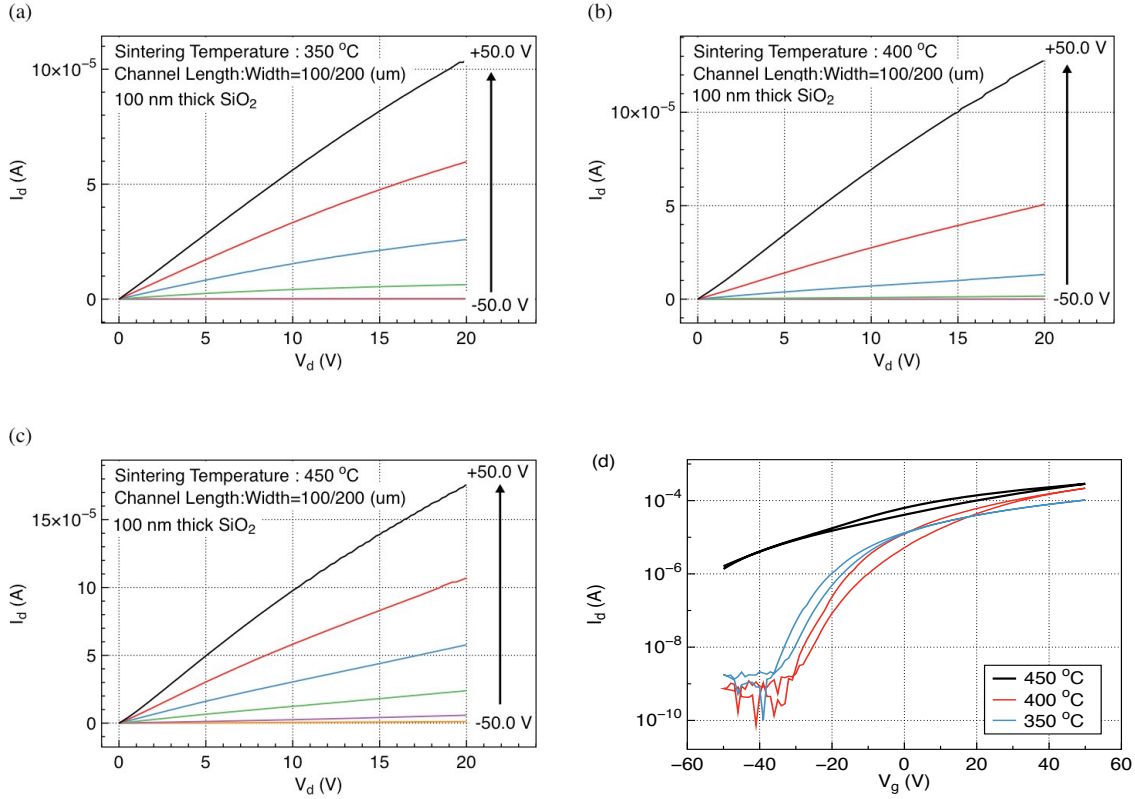
Figure 3.7 The obtained electrical characteristics of the fabricated TFTs with the pristine SnO$_2$ precursor, varying a post annealing process temperature (a) at 350 $^{\circ}$C, (b) at 400 $^{\circ}$C, and (c) at 450 $^{\circ}$C for 1 hour in air (d) I$_d$-V$_g$ curves.

In chapter 3.2, it was found that the metal oxide film quality depends on the amount of added NH$_4$OH. Corresponding TFT characteristics (channel length and width were 100 um and 200 um, respectively) were extracted. The extracted parameters are summarized in Figure 3.8. The obtained rheological properties support the formation of a gel-like phase, based on the observation of pseudo-plastic flow in the NH$_4$OH-containing precursor vs. dilatant flow in the corresponding pure precursor solution. During annealing, the gel-like precursor facilitates the formation of films with a less porous structure, smooth film morphology, and uniform film thickness. This, coupled with the reduction in decomposition temperature, facilitates the formation of films with good transport properties.

The performance benefits of exploiting the gel-like phase precursor were evaluated using the aforementioned SiO$_2$-gated test structures. Compared to the standard solution, the gel-like phase formed by adding 0.44 mmol NH$_4$OH resulted in test devices with a 3X boost in saturation mobility ($\sim$ 5.0 cm^2/Vs) and improved sub-threshold swing without any degradation in I$_{on}$/I$_{off}$. Transfer and output characteristics for these test devices are shown in Figure 3.9. The devices show excellent transport characteristics due

to the excellent polycrystalline film quality. As it is commonly observed for devices with polycrystalline channels, the devices exhibit an increase in mobility with transverse electric field due to the successful filling of gap states at higher gate biases.
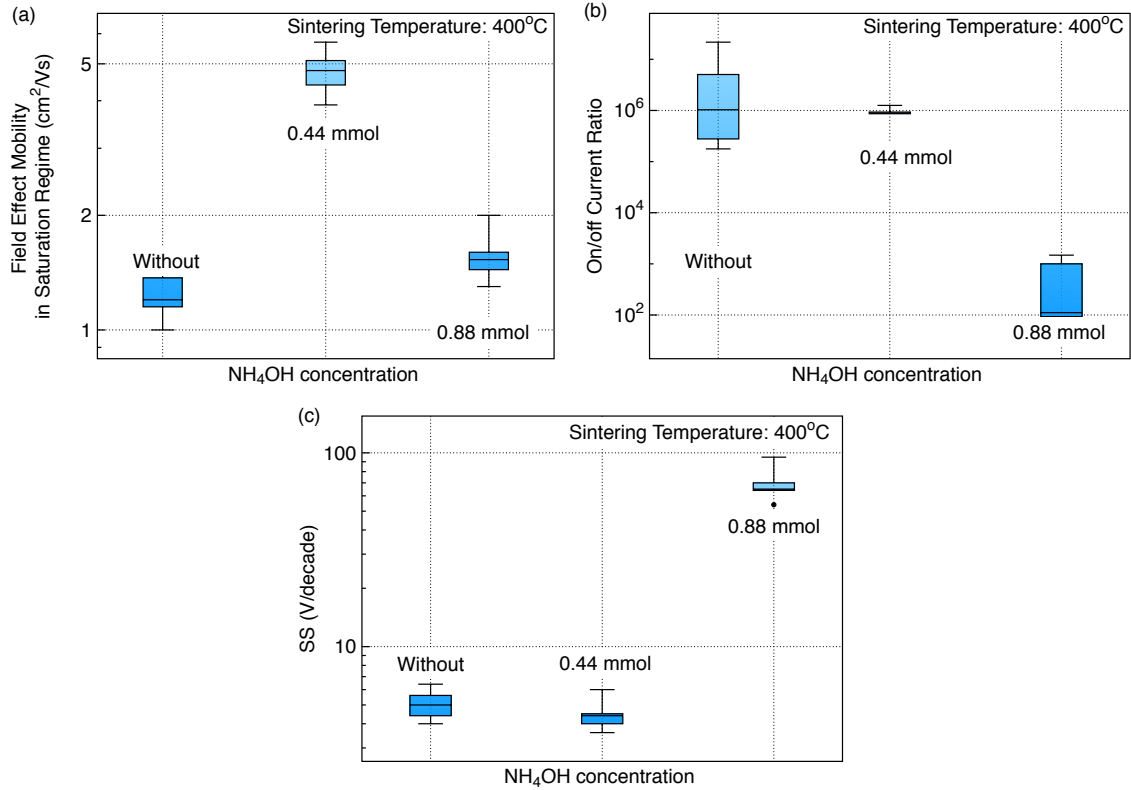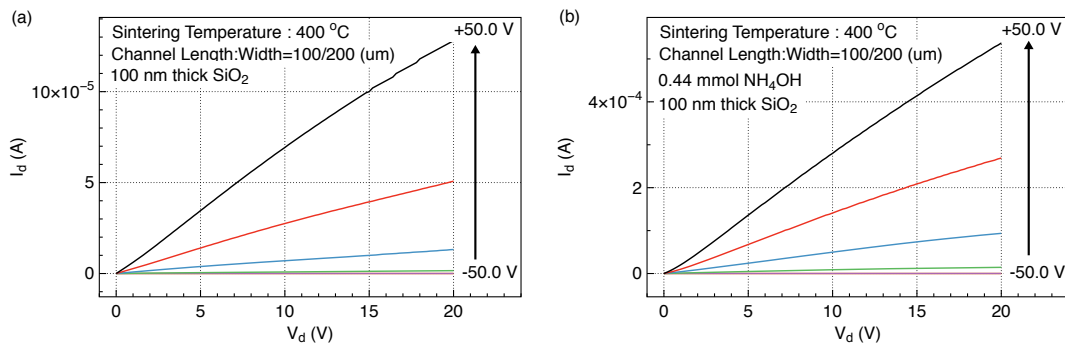

Figure 3.8 The extracted parameters of the fabricated TFTs with different NH_4OH concentrations: (a) Field effect mobility in saturation regime, (b) On/off current ratio and (c) SS.
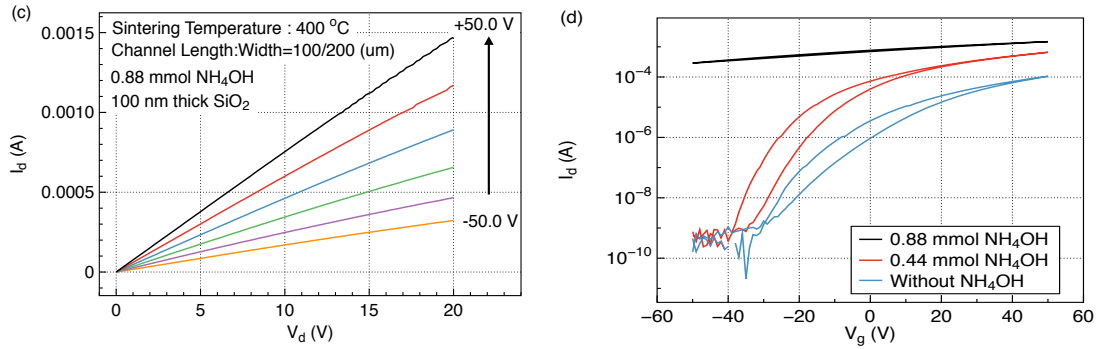
Figure 3.9 The obtained electrical characteristics of the fabricated TFTs, varying NH$_4$OH concentrations, after finishing 400 °C sintering process in air: (a) without NH$_4$OH (b) with 0.44 mmol NH$_4$OH, and (c) 0.88 mmol NH$_4$OH (d) I$_d$-V$_g$ curves.

To elucidate electron conduction mechanisms in reference TFTs and in TFTs consisting of converted SnO$_2$ from gel-like solution precursors, the transfer and output characteristics were analyzed [13], [14]. Further increase in the concentration of NH$_4$OH (0.88 mmol) also provided improved on-state performance, but resulted in some increased aggregation in the final film, causing an increase in device leakage. Specifically, to analyze the electron transport mechanisms in SnO$_2$ TFTs, the field effect mobility in the linear regime was extracted as a function of measurement temperature and biased gate voltages in Figure 3.10.
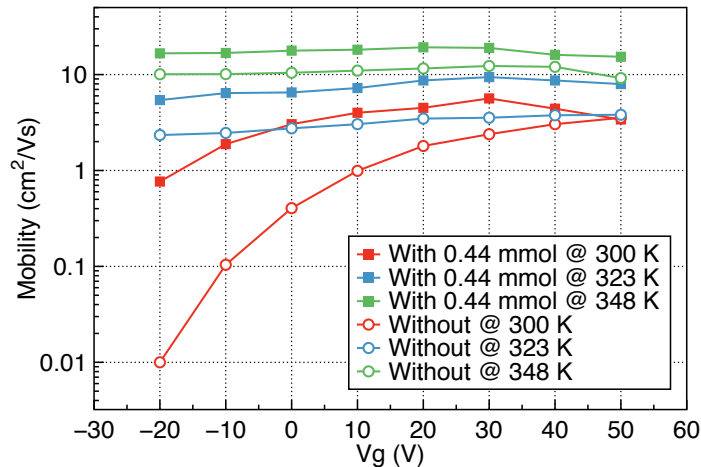

Figure 3.10 Voltages and temperature dependence of low-field mobility for SnO$_2$/SiO$_2$ test devices fabricated using gel-like (with 0.44 mmol NH$_4$OH) and pure precursors (without NH$_4$OH)

51

In chapter 2, several representative transport mechanisms for organic, amorphous, and poly crystalline material were introduced. The extracted field effect mobility in the linear regime in these models shows temperature and gate bias voltage dependency. The mobility was found to increase with gate bias, consistent with a standard multiple trapping and release (MTR) or variable range hopping (VRH) model, commonly observed in devices with polycrystalline channels [15]. Given the relatively high obtained mobilities, we suggest that MTR is the appropriate formalism.

Compared to the pure film, the film formed from the gel-like precursor showed higher mobility and weaker gate bias dependence on mobility, suggesting better band-like transport and lower impact of localized states. The improvement in mobility is consistent with a lower density of localized trap states, based on the MTR model equation, Eq. (1):

$$\mu \propto \left(\frac{C_i (Vg - Vo)}{qN_t} \right)^{\frac{T_c}{T} - 2} \tag{3.1}$$

where μ_{eff} is the low-field mobility, C_i is the insulator capacitance per unit area, V_g is the gate voltage, T_C is a characteristic temperature, and N_t is the total density of trap states. Devices with polycrystalline channels commonly exhibit temperature-dependent transport with an activation energy that is correlated to the grain boundary barrier height, indicative of the defect density at the grain boundaries. The thermally activated drain current can be expressed by

$$I_d = I_0 exp\left(\frac{-E_a}{kT} \right) \tag{3.2}$$

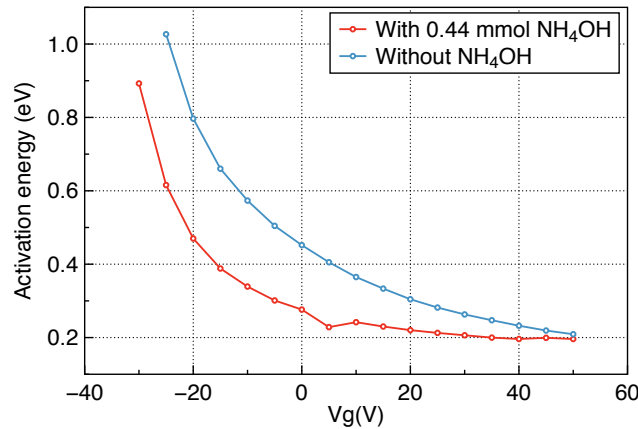where, I_0 is the prefactor, E_A is the activation energy, k is the Boltzmann constant and T is the temperature.

Figure 3.11 Variation of activation energy (E_A) versus gate voltage (V_g) for SnO$_2$/SiO$_2$ test structures as a function of NH$_4$OH addition.

The activation energy (E_A) as a function of gate bias from the temperature dependence of log (I_{DS}) vs $1/T$, was plotted in Figure 3.11. At low-biases, when most traps are unfilled, the gel-like precursor devices clearly show dramatically lower activation energy than the pure solution devices, again indicating much lower mid-gap state density. This also explains the observed improvement in sub-threshold swing [15]-[17].

3.5. The compact power law model

Based on the conventional MOSFET theory, the threshold voltage is the minimum required gate voltage to form a conducting channel between the source and drain electrodes. As illustrated in Figure 2.13, the threshold voltage is evaluated from a linear fitting to the curve of $I_d^{1/2}$ versus V_g, which originates from the conventional square law. In addition, the field-effect mobility is independent of the biased gate voltage. In contrast, there is an ambiguity in evaluating the threshold voltage using the conventional square law theory. For thin-film transistors, including our systems, which are defined with the conventional theory, significant drain current is typically obtained below a threshold voltage. The conventional model cannot explain the transport mechanism at a low gate bias voltage, which is close to the extrapolated threshold voltage. Thus, the drain current, which is above the threshold voltage, is modeled using a power-law dependence based on the biased gate voltages. The basic equations are introduced in Chapter 2.

Based on Equations 2.26 and 2.27, the saturation drain current can be expressed as

$$I_{Dsat} = A(Vg - Vt)^m \tag{3.3}$$

where A is a the conductance parameter, m is an empirical parameter, and Vt is the threshold voltage extracted from the power-law equation. The integral operator method is used to extract Vt as follows, assuming that the channel conductivity is a power function of (V_g-V_t) [18], [19]:

$$H(Vg) = \frac{\int_0^{V_g} I_{dsat}(Vg)dVg}{I_{dsat}} \tag{3.4}$$

This model can be applied to the drain current in the saturation regime, particularly above the threshold voltage. We can separate into two regions; then, Equation 3.5 can be further simplified, and H(Vg) is given by Equation 3.6:

$$H(Vg) = \frac{\int_0^{V_t} I_{dsat}(Vg)dVg}{I_{dsat}} + \frac{\int_{V_t}^{V_g} I_{dsat}(Vg)dVg}{I_{dsat}} \tag{3.5}$$

$$H(Vg) = \frac{\int_{V_t}^{V_g} I_{dsat}(Vg)dVg}{I_{dsat}} = \frac{Vg - Vt}{\gamma + 2} \qquad (3.6)$$

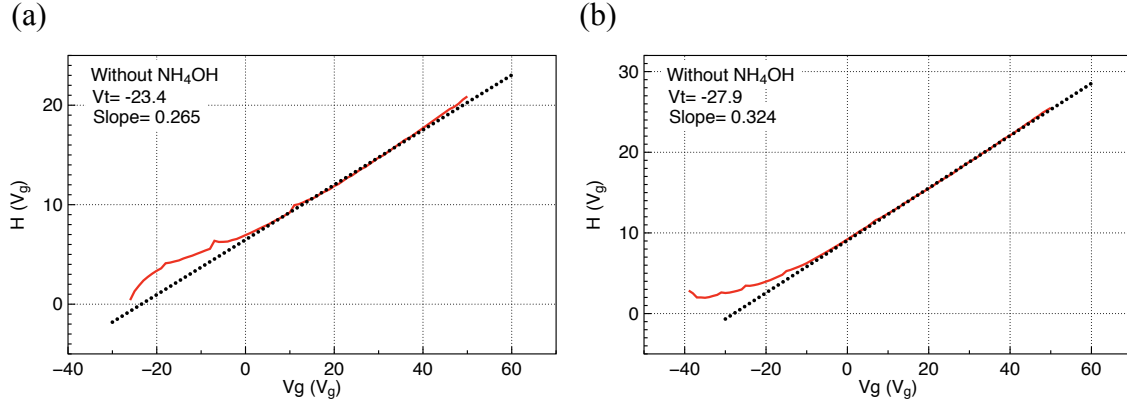(a)   (b)

Figure 3.12 Integral function curves. The dotted line represents a linear interpolation of H for the SnO_2 semiconductor, which is converted from the pure precursor (a) and the NH_4OH-added precursor (b).

Then, Vt and the gamma values are determined from the slope using Equation 3.6. Figure 3.12 presents the numerical H as a function of Vg. The Vt values obtained from the linear regression of H(Vg) and the extracted Vt values are -23.4 and -27.9 V, respectively.

   We can determine the film quality from the gamma number using Equation 3.6 and the slope of the H-Vg curves in Figure 3.12. From Equation 2.33, the empirical parameter *m* in Equation 3.3 is $\gamma+2$. The extracted empirical parameter values with the pure precursor and NH_4OH-added precursor are 2.84 and 2.12, respectively. γ is equal to $2(T_c/T)-2$. From this equation, the extracted T_c values are 387 and 289 K. The gamma number and T_c value of the SnO_2 layer, which is converted from 0.44 mol of the NH_4OH-added precursor, are lower than those of the pure precursor. This result confirms that the SnO_2 layers with NH_4OH are of higher quality and are closer to the ideal single layer $(T_c=T)$, which results in better thin-film transistor performance. The lower T_c values correspond to a distribution with a steeper tail. The validity of these numbers was confirmed again from the obtained I_d-V_g curves in the linear regime. In the previous section, the I_d-V_g curves were obtained as a function of the measurement temperatures in Figure 3.13 to evaluate the activation energy. The empirical parameters in the linear regime were evaluated based on Equation 2.30. In the linear regime, the relation between the empirical parameter m and γ is $m=\gamma+1$. The differences in the extracted T_c values between two regimes were within 10%. From these curves, the T_c values were extracted again using Equation 2.33. The summarized values are listed in Table 3.1. The gate bias

dependent property was considered based on the extracted Υ and the relationship between the drain current and gate bias voltage in Equation 2.30.

$$\frac{dI_d/dV_g}{W/LC_iV_d} = (1+\gamma)\mu(Vg - Vt)^{\gamma} \tag{3.7}$$

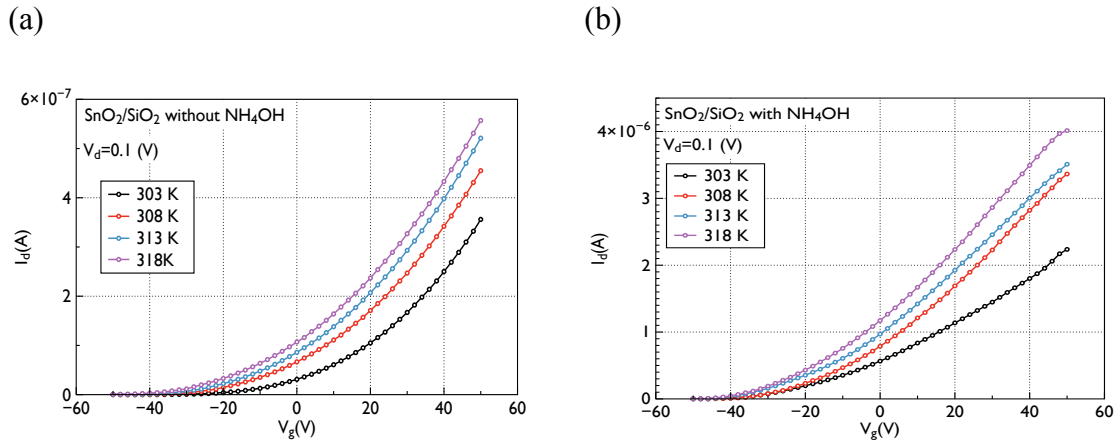(a)   (b)

Figure 3.13 I_d-V_g curves were obtained as a function of the measurement temperatures. (a) Pure precursor and (b) 0.44 mol NH_4OH-added precursor
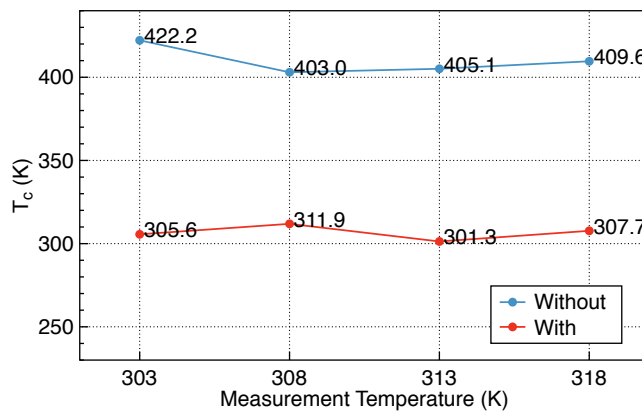

Figure 3.14 The extracted T_c values as a function of the measurement temperatures from the I_d-V_g curves in the linear regime.

	Pure precursor	NH$_4$OH-containing precursor
Tc (in the saturation regime)	387 (K)	289 (K)
Tc (in the linear regime)	~ 404.9 (K)	~ 306.6 (K)
Field-effect mobility in the saturation regime	~ 1.5 (cm^2/Vs)	~ 5.0 (cm^2/Vs)
On/off current ratio	~ 10^6	~ 10^6
SS	~ 4.5 V/decade	~ 3.5 V/decade

Table 3.1 Summarized Tc values and thin-film transistor parameters with different precursor conditions. A smaller Tc value implies that the semiconductor films have higher film quality, which results in improved thin-film transistor performances

The conductance parameter A is plotted as a function of Vg in Figure 3.15 using the extracted Vt and m values and Equation 3.3. As expected, the extracted A value is constant regardless of Vg in the saturation regime. In addition, the simulated conductance parameters are compared with the experimentally measured parameters, and the simulation results are consistent with the measured results in the saturation regime, as shown in Figure 3.16.
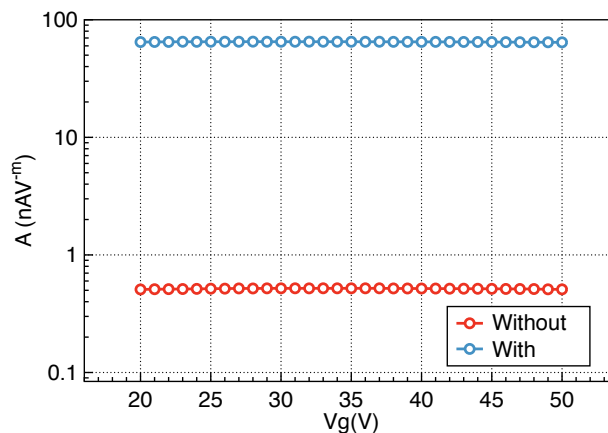

Figure 3.15 Extracted conductance parameter of the fabricated TFTs with the pure precursor and NH$_4$OH-added precursor. The conductance parameter values are nearly constant regardless of the applied gate voltages.
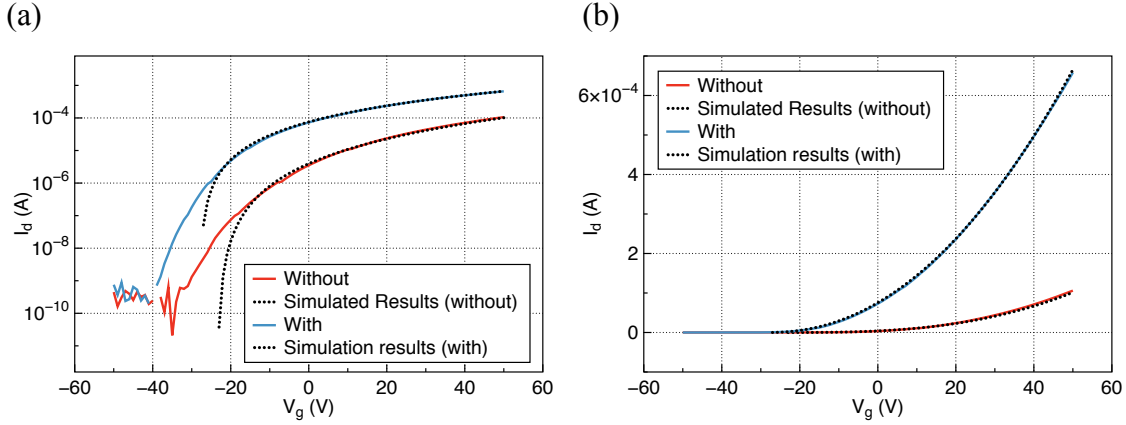
(a) ... **(b)** ...

Figure 3.16 Experimentally measured Id-Vg curves and simulated results with the extracted parameter for the empirical power law. (a) Log scale and (b) linear scale.

The compact power law model used here is based largely on MTR theory and the inclusion of the conductance parameter A originated from the percolation theory model. We can also extract useful parameters having physical meaning, such as the concentration of localized states (G_0) and the characteristic temperature (T_c) of the exponential density of states, which is represented as $G(E)=G_0 exp(-E/K_B T_C)$. It is shown that this approach is valid for the fabricated SnO_2 based TFTs operating above threshold regime to understand and describe the TFT operational behaviors.

3.6. Cut-off frequency

Measuring the cut-off frequency is another characterization scheme to estimate the speed of the fabricated thin-film transistors. The cut-off frequency is defined as the frequency at unity current gain, i.e., when the ratio of the output current to the input current is one. Figure 3.17 presents the measurement setup for the cut-off frequency. The accurate approach to measuring this parameter is to directly measure the input and output currents. Unfortunately, it is difficult to measure the input current in our devices due to the low gate capacitance. Instead, the input current value was calculated using the relation of $V_{in} \times j\omega C_{in}$, where C_{in} is the input capacitance, which was directly measured using a 4285A LCR meter; since we use thermal oxide for these devices, the capacitors are well behaved and we expect this estimation to be reasonably accurate. To directly measure the output current, the resistor was loaded between the output voltage and Vss. To select the most appropriate resistor, the channel output resistance value was first extracted from the I_d-V_g curves of the fabricated thin-film transistor in the linear regime. Then, the calculated channel output resistance was divided by 10. Here, a 20 $k\Omega$ resistor was chosen. The transistor was biased at $V_g = V_d = 0$ V and $V_s = -30$ V with an Agilent 4156C to obtain the maximum transconductance (g_m). A small signal of 3 V_{pp} was biased on top

of the DC gate bias. The output voltage was obtained using a pico-probe under varying AC input signal frequency.

(a)

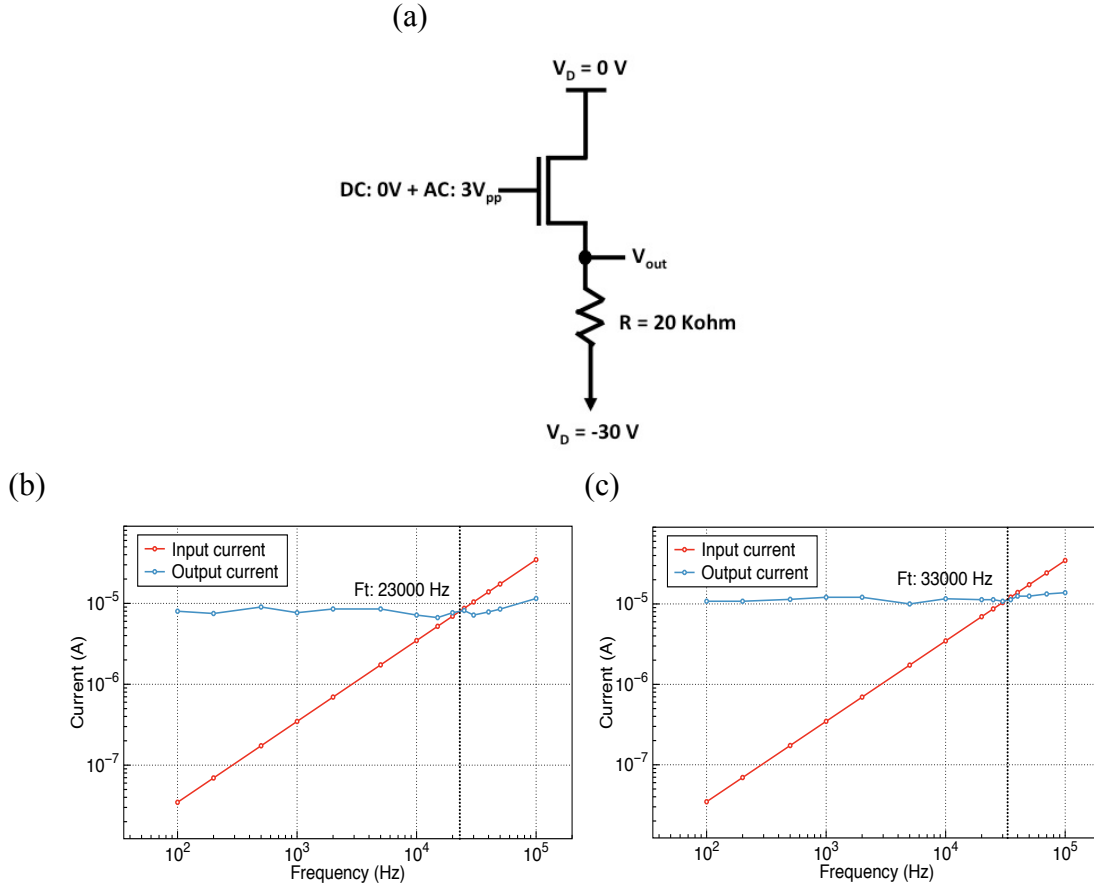(b)   (c)

Figure 3.17 (a) Measurement setup for the input and output currents of a fabricated thin-film transistor. Cut-off frequency measurements of the SnO_2 transistors (b) with the pure precursor and (c) with 0.44 mol NH_4OH.

Figure 3.18 presents a schematic diagram of the thin-film transistor small-signal model, including the intrinsic and extrinsic components. In our thin-film transistor structure, the gate electrodes are not patterned and fully overlapped with the source and drain electrodes. If we define the length of the overlapped source and drain electrodes as L_{gs} and L_{gd}, respectively, then the gates to the source and drain overlap, and the capacitances can be expressed as follows (in the saturation regime):

$$C_{gs} = WL_{gs}C_i + \frac{2}{3}WLC_i \tag{3.8}$$

$$C_{gd} = WL_{gd}C_i, \tag{3.9}$$

$$f_T = g_m/(2\pi(C_{gd} + C_{gd})) \tag{3.10}$$

Using Equations 3.8 and 3.9, the cut off frequency is expressed by Equation 3.11.

$$f_T = g_m/(2\pi(C_{gd} + C_{gd})) = \mu V_d/(2\pi L(L_{gs} + L_{gd} + 2/3L)) \quad (3.11)$$
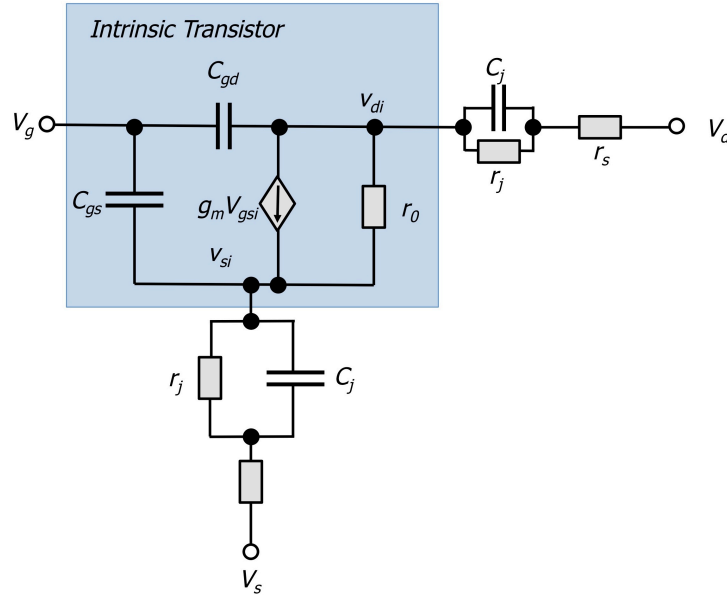
Figure 3.18 presents a schematic diagram of the thin-film transistor small-signal model, including the intrinsic and extrinsic components.

The field-effect mobilities in the saturation regime are 1.4 and 3.0 cm^2/Vs, V$_d$ is 30 V, and the channel lengths L$_s$ and L$_d$ are 100 μm. The calculated cut-off frequencies for each device are 25 Khz and 47 Khz, respectively. The calculated values are somewhat higher than the measured values, but still in the same order, suggesting that the DC transport characteristics are representative of achievable AC performance. The slight error may originate from the underestimated L$_s$ and L$_d$.

$$Frequency_{MAX} = \frac{1}{Intrinsic.\,delay} = \frac{1}{R_{on}C_{Load}} \quad (3.12)$$

59

If V_d is sufficiently large, then R_{on} is

$$R_{on} \cong \frac{V_d}{I_{dsat}} = \frac{V_d}{\frac{1}{2} \mu C_i \frac{W}{L} (Vg - Vth)^2} \cong \frac{2}{\mu C_i \frac{W}{L} V_d} \qquad (3.13)$$

$$C_{load} = C_{gs} + C_{ds} = WL_{gs}C_i + \frac{2}{3} WLC_i + WL_{gd}C_i \qquad (3.14)$$

Using Equations 4.6 and 4.7, the maximum frequency can be expressed as

$$Frequency_{MAX} = \mu V_d / (2L(L_{gs} + L_{gd} + 2/3L)) \qquad (3.15)$$

To further increase the speed of the devices in the AC operation, the field-effect mobility must first be large. Second, as observed in Equations 3.11 and 3.15, patterned gate electrodes are required to reduce the overlap area. In addition, a highly scaled channel length is critical. For example, if we fabricate an active channel that is 10 times shorter with a patterned gate electrode, the expected cut-off frequency is approximately 10 MHz for the SnO_2 precursor, assuming that no additional dispersive phenomena become important.

3.7. Contact effects

We can occasionally observe nonlinearities in the electrical characteristics and transfer I-V curves, which deviate from the ideal cases. The most representative cause originates from the energy barriers between mismatched source and drain electrodes and the semiconductor. These contact effects depend on the bias condition and work functions of the electrodes. The structure must be considered as two Schottky diodes that are connected to each other when there are energy barriers between the electrodes and semiconductor. The current equation for diodes is

$$I = I_0[exp(\frac{qV}{nkT}) - 1] \qquad (3.16)$$

where n is the ideality factor. The relationships between the current and voltages are

$$I_{ds} = I_0 tanh(\frac{qV_{ds}}{nkT}) \qquad (3.17)$$

Ideally, if we choose a suitable material for the electrodes, the linear current-voltage relationship can be shown following Ohm's Law, which we can refer to as Ohmic contacts. The contact resistance can be expressed through voltage drop factors: a decrease in the voltage drop between the electrodes leads to a decrease in current. This contact resistance factor will be more critical when the ratio between the contact resistance and channel resistance increases. For example, shorter channel lengths make the channel resistance much smaller than the contact resistances. Thus, to improve the electrical characteristics of the fabricated thin-film transistors, it is also important to find suitable materials for the source and drain electrodes and to estimate the contact resistance values. The transfer line method (TLM) is widely used to evaluate the series contact resistance [20], [21]. This simple method assumes that the thin-film transistor is a type of resistance that consists of two contact resistances (R_C) and one main channel resistance (R_{ch}). The total resistance value can be extracted from the I-V curves under conditions of a low drain-source voltage to make the distribution of major carriers uniform. In the linear regime, the channel resistance can be expressed as

$$R_{ch} = L/W\mu C_i(Vg - Vt) \tag{3.18}$$

where W is the channel width, L is the channel length, μ is the mobility, and Ci is the unit area capacitance of the dielectric. Vg and Vt are the biased gate voltage and threshold voltage, respectively. To extend this equation to transistors with different W values, the total resistance can be normalized by the channel width W:

$$R_{total} \times W = \frac{L}{\mu C_i(Vg - Vt)} + R_s + R_d \times W \tag{3.19}$$

The width-normalized total resistance values were plotted as functions of the channel length. When the channel length is zero, the extrapolated total resistance of the channel length is the contact resistance. Figure 3.19 presents the total resistance of the fabricated thin-film transistor with Au source and drain electrodes as a function of the channel length with different biased gate voltages. The total resistance values were extracted from different channel lengths of 40 and 100 μm. The extracted contact resistance value was approximately 20 kΩ. The channel resistance values can be evaluated from the total resistance values by subtracting the contact resistance values, which correspond to different applied gate voltages. The extracted channel resistances of the fabricated thin-film transistor with the 0.44 mol NH_4OH-added precursor are lower than those of the fabricated thin-film transistor with the pure precursor regardless of the applied gate voltages. The extracted contact resistance value was lower than the

minimum channel resistance, particularly in the on state. Thus, the contact resistance does not limit the thin-film transistor performance for both cases.

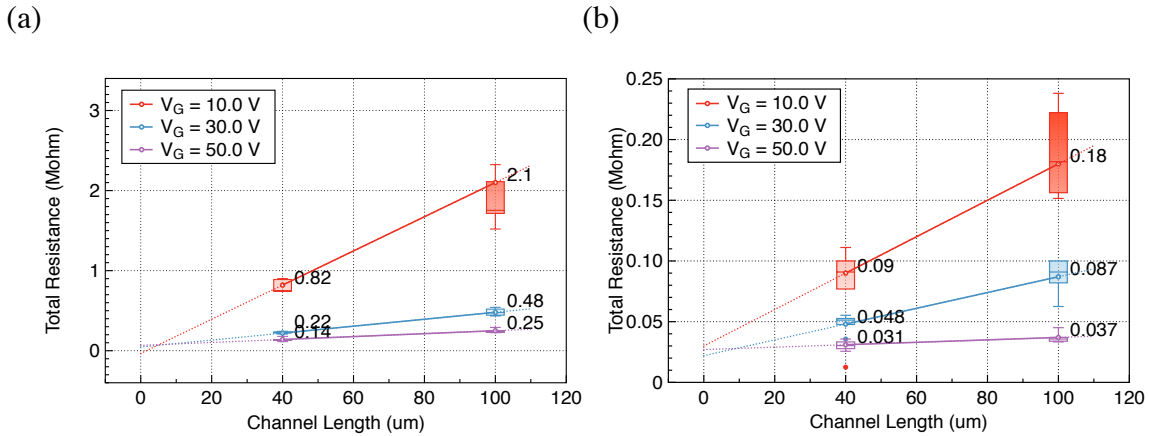(a)   (b)

Figure 3.19 Extracted total resistance as a function of the channel length with different biased gate voltages from the fabrication thin-film transistor with a pure precursor (a) and the 0.44 mol NH_4OH-added precursor (b).

3.8. Aging time effects

As mentioned in Chapters 1 and 2, the precursor phase and final converted products were affected by many factors, such as the temperature, surfactant, and precursors. This chapter has demonstrated that deposited-film qualities were improved by increasing the sintering temperature and adding NH_4OH. These processes increase the crystalline size, which makes the grain less porous and the high-quality films smoother and increases the thin-film transistor performances. In this section, we investigate the aging time effects at the precursor level instead of the process parameters. The time interval between the precursor preparation process and spin casting process was controlled. Three groups were prepared with different aging times of 30 and 60 min with and without NH_4OH. First, each precursor was spin-casted on SiO_2/Si substrates that were UV/ozone-treated for 10 min. After depositing Au source/drain electrodes by thermal evaporation, the sintering process was conducted at 400°C for 1 h in air. Figures 3.20 and 3.21 present the statistical data of the field-effect mobility in the saturation regime and the on/off current ratio. Significant degradation was not observed up to 30 min. However, the field-effect mobility in the saturation regime and the on/off current ratio were significantly degraded after 30 min regardless of the NH_4OH concentration. The degraded field-effect mobility and on/off current ratio originate from the decreased transport characteristics in the aged films. In particular, the on-current of the fabricated thin-film transistors with precursors aged for 60 min were approximately 100 times lower than that of the fabricated thin-film transistor with as-prepared and 30 min aged

62

precursors. More specific investigation is necessary to understand this result. However, similar effects have been observed in other metallic precursor sol-gel systems [22].
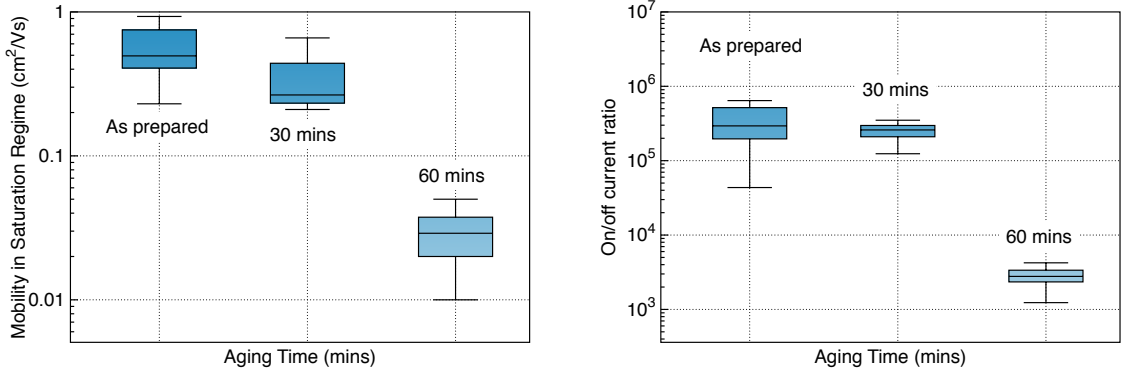

Figure 3.20 Statistical data of the field-effect mobility in the saturation regime and the on/off current ratio of the fabricated thin-film transistor with the pure precursor as a function of the aging time.
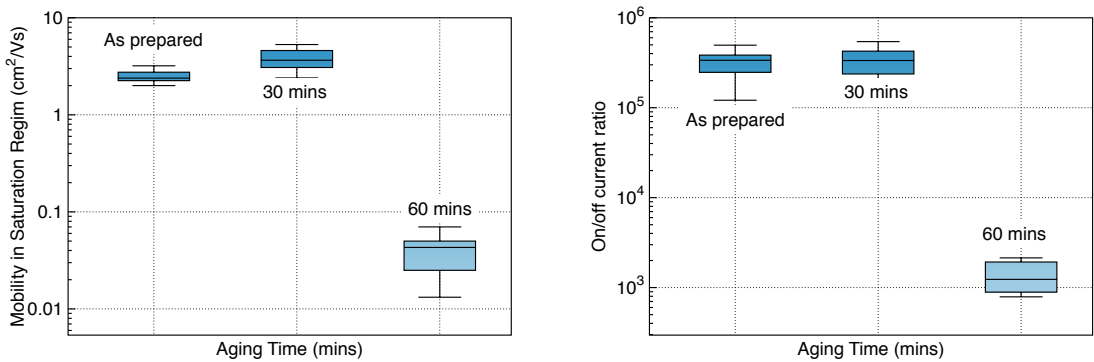

Figure 3.21 Statistical data of the field-effect mobility in the saturation regime and the on/off current ratio of the fabricated thin-film transistor with the 0.44 mol NH_4OH-added pure precursor as a function of the aging time.

3.9. Sol-gel processed SnO_2 on ZrO_2 transistors

Several approaches to improving the performance of metal oxide TFTs have previously been investigated, such as modification of the semiconductor film, deposition of an intermediate layer between the semiconductor and the insulator and employment of

high-k insulators. In particular, an improvement in mobility has been observed across numerous metal oxide TFT systems and has generally been explained by the higher carrier concentrations achievable at lower voltages when high-k insulators are used. Some of these carriers fill localized states, resulting in devices with higher mobility and more band-like transport [23-25]. Wang, Kim and coworkers have shown that the quality of the semiconductor/dielectric layer interface contributes to significant enhancement of the transistor performance [26]. Here, devices with high-k dielectrics show improved sub-threshold slope due to improvements in overall trap state density, particularly close to mid-gap. A small lattice mismatch between the metal oxide and the insulator is considered to be another factor in improving the TFT performance because a small lattice mismatch can lead to a well-aligned epitaxial film compared to the disordered interfaces of metal oxides on SiO_2 layers [27].

A ZrO_2 liquid precursor was prepared by dissolving 0.001 mol of zirconium acetylacetonate in 10 ml of ethanol with 0.1 ml of mono-ethanolamine. The UV/ozone treatment was conducted prior to the precursor deposition. The deposited precursors were sintered as a function of the temperature with different process times. Figure 3.22 (a) presents the XRD spectra that were obtained from the deposited ZrO_2 layer as a function of the annealing temperature and time at 400°C, which is shown in Figure 3.22 (b), respectively. The broad XRD peaks that are visible after sintering at 300°C are consistent with the reference tetragonal ZrO_2 structure, and a strong crystallinity developed only at or above 400°C.
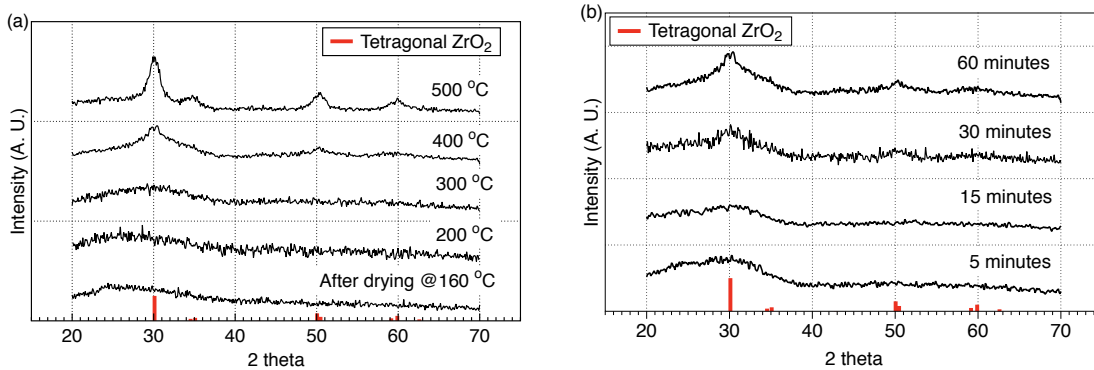

Figure 3.22 (a) XRD spectra of ZrO_2 films sintered at different temperature for 1 hour in air. (b) XRD spectra of ZrO_2 films sintered at 400 °C in air for various times.

The quality of the ZrO_2 layers, e.g., the dielectric constant dispersion, breakdown field, and gate leakage current, was characterized using a cross-bar capacitor that consists of a sol-gel-processed ZrO_2 layer (100 nm thick) sandwiched between two thermally deposited Au electrodes. First, the XRD spectra were obtained with different process times at 400°C in air based on the optimized sintering conditions for SnO_2 semiconductor layers. The broad XRD peaks became visible after 5 min, which confirmed the

conversion of ZrO_2. The major XRD peaks were clearly visible after 1 h, which was consistent with the reference tetragonal ZrO_2 structure.

Figure 3.23 illustrates the variation of the dielectric constant as a function of frequency for the samples sintered at different temperatures and times. The dielectric constant exhibits an obvious decreasing trend behavior with increasing frequency [28]-[31] and remains relatively constant at higher frequencies (over 10 kHz). However, the dispersion of the dielectric constant decreases as the sintering temperature and the process time increase. The increase of the dielectric constant is determined by the polarization of the materials. It is well known that in a sol-gel system, H_2O or OH groups in the films and other impurities result in electronic or ionic polarization, which result in a similar frequency dependency [32]. To solve this issue, first, a longer process at higher temperature is suggested [33]. Second, the sintering process should be conducted in O_2 to minimize these effects [34], [35]. Here, the sintering process was conducted at 450°C for 2 h in air to minimize the dielectric constant dispersion. The ZrO_2 films were sintered at 450°C for 2 h in air, as confirmed by the XRD spectra in Figure 3.24.
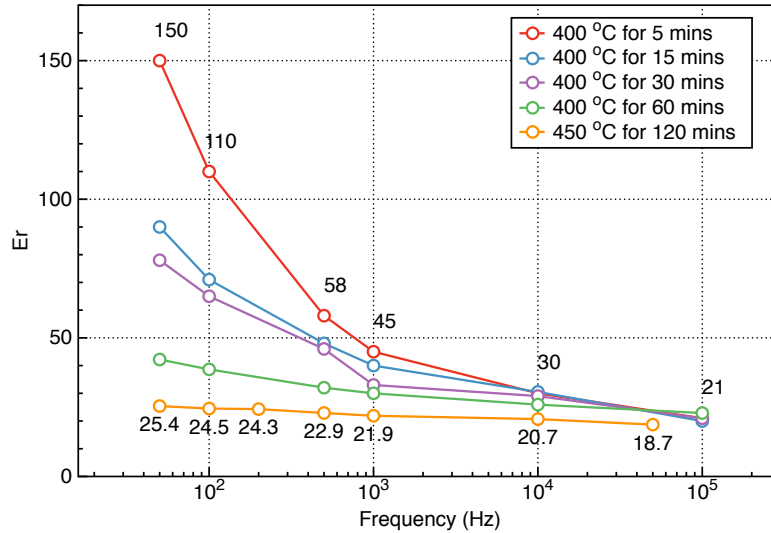

Figure 3.23 Variance of the dielectric constant of sintered ZrO_2 films with different sintering processes.
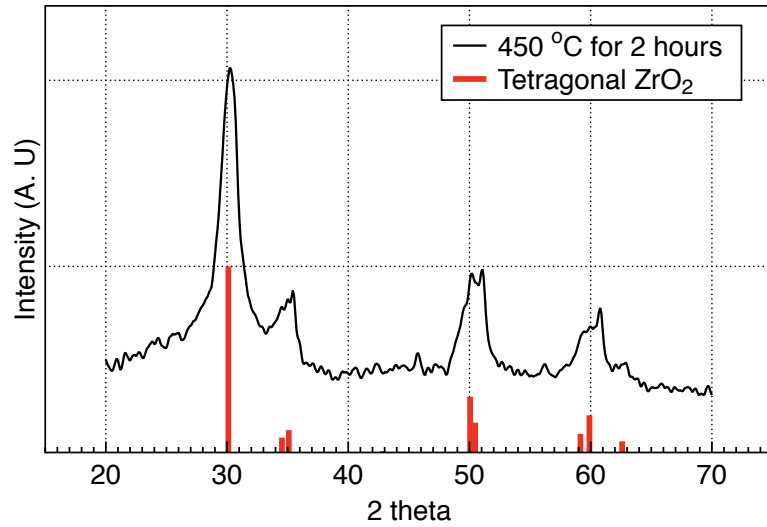
Figure 3.24 XRD spectra of ZrO$_2$ films sintered at 450°C for 2 hours in air.

Figure 3.25 presents the typical leakage current and the break down voltage of the prepared devices. The breakdown field is defined at the abrupt increase in the leakage current. As observed, the ZrO$_2$ films (average film thickness of approximately 75 nm) that were sintered at 450°C for 2 h in air exhibit less gate leakage current and increased breakdown voltages.

(a)

(b)
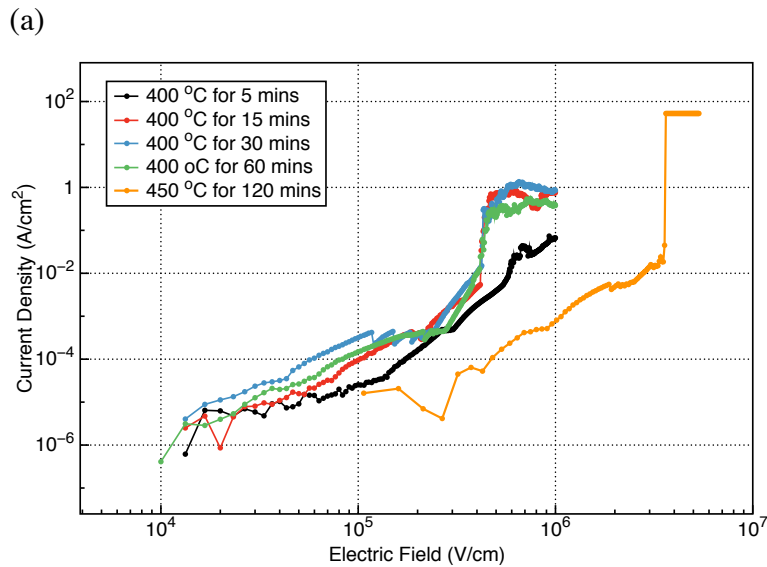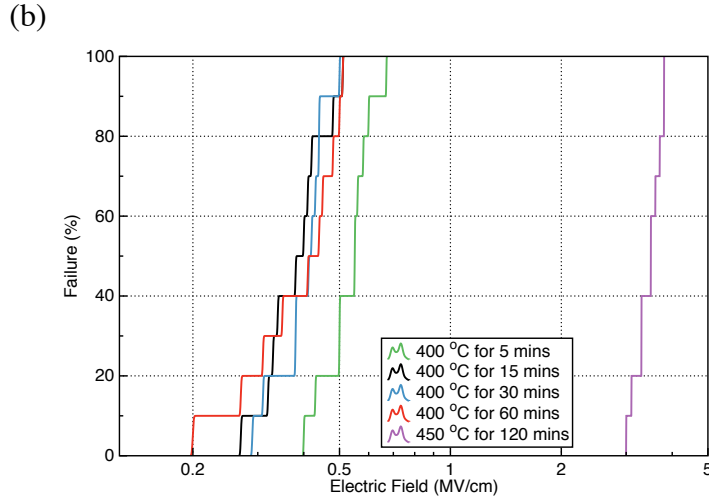
Figure 3.25 (a) Typical leakage and breakdown curves of the prepared Au/ZrO$_2$/ITO capacitors in air. (b) Cumulative plot of the ZrO$_2$ breakdown with different annealing process times.

Based on the aforementioned ZrO$_2$ fabrication process, devices with high-k gate dielectrics were fabricated on commercial ITO-coated glass substrates with an ITO thickness of 250 nm as follows: the discussed zirconium precursor solution was ultrasonicated for 1 h. The schematic structure for SnO$_2$/ZrO$_2$ TFTs are illustrated in Figure 3.26.

Figure 3.26 Schematic structure of the fully transparent SnO$_2$/ZrO$_2$ TFTs fabricated herein.

Then, the prepared ZrO_2 precursor was spin-coated on UV/ozone-treated ITO/glass substrates at 3,000 rpm for 30 s. Five sequential spin-coating operations were performed to realize a 75 nm-thick ZrO_2 dielectric layer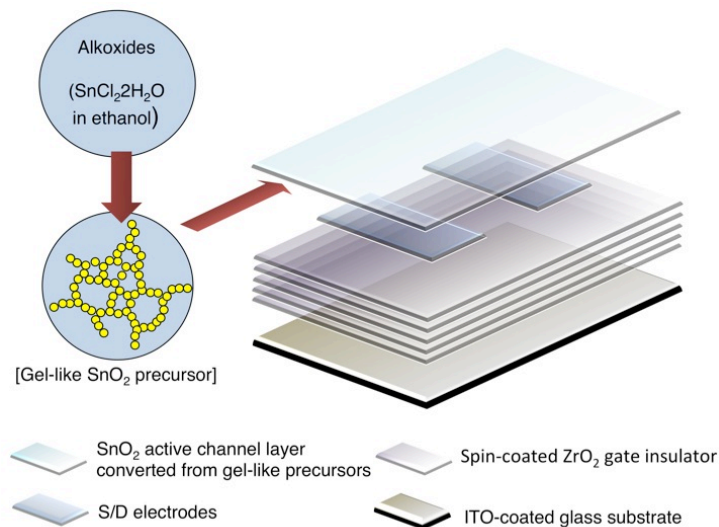. Each layer was dried at 250°C for 1 min prior to the next coating step. Next, 50 nm-thick Au source/drain electrodes were thermally evaporated. Finally, the SnO_2 semiconductor layer was deposited as above and consequently dried at 100°C for 10 min in air. To minimize the fringing current effects and gate leakage, the SnO_2 and ZrO_2 layers were patterned by removing the aforementioned films with a mechanically controlled probe tip. This tip was dragged around each transistor as close as possible to the contact pads and channel area prior to the sintering process to ensure a complete film removal using mechanical abrasion, and this process was followed by the sintering process at 450°C for 2 h in air.

Figure 3.27 presents the electrical characteristics of the fabricated SnO_2/ZrO_2 TFTs. The fabricated TFTs exhibited the conventional n-type transistor characteristics. The field-effect mobility in the saturation regime was approximately 30 cm^2/Vs. The on/off current ratio was approximately 10^3. Excellent characteristics were obtained at operating voltages below 1.5 V. Because of the high-k ZrO_2 dielectric layer, the active channel layer accumulated at rather low gate voltages, and the interface trap density between ZrO_2 and SnO_2 was significantly reduced, as indicated by the reduction of the SS from 5 to 0.3 V/decade.

(a)   (b)
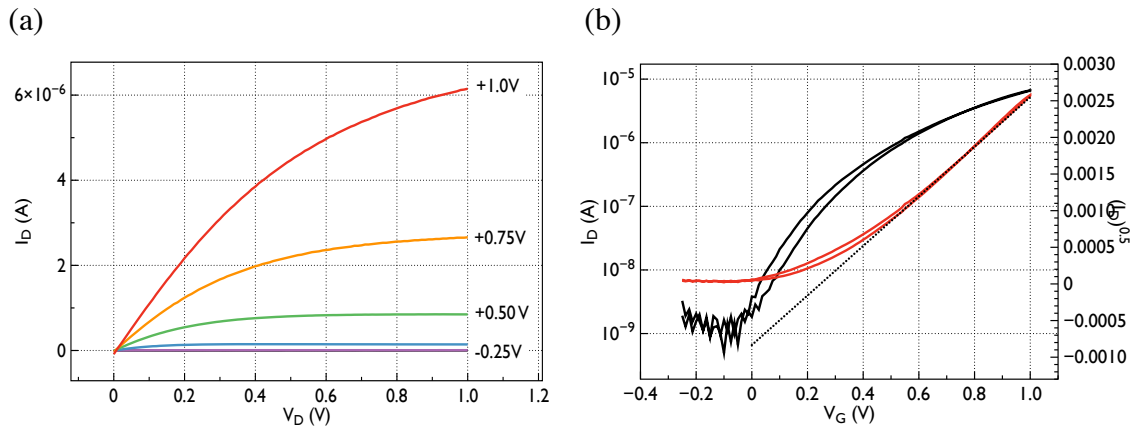
Figure 3.27 Representative electrical characteristics of the SnO_2/ZrO_2 transistors (a) I_d-V_d and (b) I_d-V_g (left axis) and $I_d^{0.5}$-V_g (right axis).

The optical properties of the transparent TFTs were determined through the entire film stack. Optical transmittance spectra of fully transparent SnO_2/ZrO_2TFTs structure on ITO/glass substrates are shown in Figure 3.28. Clearly, the optical transparency is excellent, with essentially no significant impact on the transparency of the overall device relative to that of standard ITO-coated glass. It also suggests that the fully transparent devices can be fabricated with transparent S/D electrodes.

Figure 3. 28 Optical transmittance spectra of fully transparent
SnO_2/ZrO_2 films on ITO/glass substrates.

Compared to the SiO_2-based test devices, the high-k devices showed a dramatic increase (~5X) in mobility, including devices with mobility of >30 cm^2/Vs. This increase in mobility results from the improved quality of the semiconductor and reduced defectivity of semico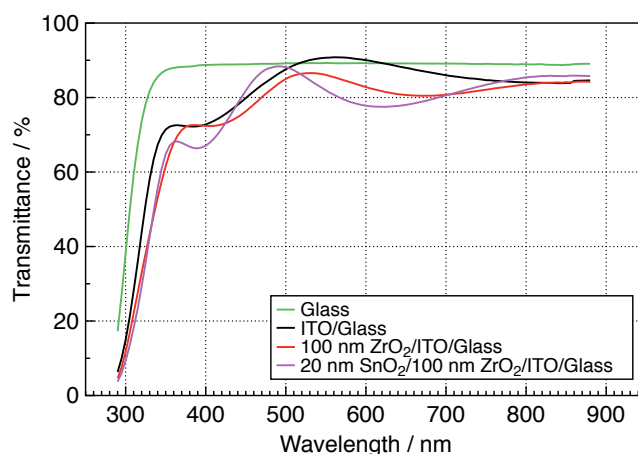nductor/dielectric layer interface. The underlying reasons for this dramatic enhancement are in need of further study and are a topic for future research. Based on these results, the combination of SnO_2 and ZrO_2 is a promising candidate for the next generation of transparent electronics.

3.10. Summary

We have demonstrated that SnO_2 is a promising candidate for transparent semiconductors and have developed a remarkably high-performance solution-processable route on sol-gel processed ZrO_2 insulators. The film quality and TFT characteristics of different NH_4OH-added precursors were investigated as a function of the NH_4OH concentration. The relationship between the sheer rate and viscosity confirmed that the gel-like precursor produced more uniform and poreless SnO_2 layers after the addition of 0.44 mol of NH_4OH. Furthermore, the sintered SnO_2 semiconductor layers had good film quality and high crystalline size, as confirmed by the XRD data and obtained AFM images. The field-effect mobility in the linear regime was evaluated to understand the transfer mechanism inside the SnO_2 semiconductor layers. The field-effect mobility in the linear regime depends on the measurement temperature and biased gate voltage, which is consistent with the MTR model for organic, amorphous, or polycrystalline TFTs. Based

69

on this model, the activation energy and film quality parameter values were extracted using equations. In addition, an empirical power law model was used to explain the non-linear relationship between the drain current and gate voltage. All of the obtained material characteristic data and lower activation energy curves with narrow distributions and small T_c values confirmed that NH_4OH plays a major role in obtaining higher-quality SnO_2 semiconductor layers. In addition, the AC characteristics of the fabricated SnO_2 TFTs and contact resistance were also extracted based on the LTM. We have developed a novel solution-processed transparent thin-film transistor technology based on a sol-gel-deposited SnO_2 semiconductor and ZrO_2 dielectric layers. The sol-gel-processed ZrO_2 films demonstrate that the dielectric constant varies with frequency due to dispersive effects, particularly for inadequately annealed films. Higher temperature process and longer sintering process minimize the dielectric constant dispersion, decrease the leakage current, and promote the breakdown properties. The entire process is fully compatible with low-cost display glass substrates and delivers unprecedented levels of performance. The devices were demonstrated to have a saturation mobility of approximately 30 cm^2/Vs, a sub-threshold swing of approximately 0.3 V/decade, and an operating voltage less than 1.5 V. These results represent a significant improvement and important step toward the realization of low-cost, large-area, high-performance systems on glass.

3.11. References

[1] K. Govender, D. S. Boyle, P. B. Kenway, and P. O'Brien, "Understanding the factor that govern the deposition and morphology of thin films of ZnO from aqueous solution," *J. Mater. Chem.,* vol. 14, pp. 2575-2591, 2004.

[2] S. Ilican, Y. Caglar, and M. Caglar, "Preparation and characterization of ZnO thin films deposited by sol-gel spin coating method," *Journal of Optoelectronics and Advanced Materials.*, vol. 10, no. 10, pp. 2578-2583, 2008.

[3] J. Wang, Y. Qi, Z. Zhi, J. Guo, M. Li, and Y. Zhang, "A self-assembly mechanism for sol-gel derived ZnO thin films," *Smart Mater. Struct.*, vol. 16, no. 6, pp. 2673-2679, 2007.

[4] X. Wang, Q. Zhang, Q. Wan, G. Dai, C. Zhou, and B. Zou, "Controllable ZnO architectures by ethanolamine-assisted hydrothermal reaction for enhanced photocatalytic activity," *J. Phys. Chem. C.*, vol. 115, no. 6, pp. 2769-2775, 2011.

[5] J. Wang and L. L. Shaw, "Synthesis of high purity hydroxyapatite nanopowder via sol-gel combustion process," *J. Mater Sci: Mater Med.*, vol. 20, pp. 1223-1227, 2009.

[6] A. C. Pierre, "*Introduction to sol-gel Processing",* Kluwer academic publishers, 2002.

[7] H. Bahadur, A. K. Srivastava, R. K. Sharma, and S. Chandra, "Morphologies of sol-gel derived thin films of ZnO using different precursors materials and their nanostructures," *Nanoscale Res. Lett.*, vol. 2, no. 10, pp. 469-475, 2007.

[8] H.-W. Kim, H. –E. Knowles, and J. C. Knowles, "Improvement of hydroxyapatitie sol-gel coating on titanium with ammonium hydroxide addition," *J. Am. Ceram. Soc.*, vol. 88, no. 1, pp.154-159, 2004.

[9] R. S. Hiratsuka, S. H. Pulcinelli, and C. V. Santilli, "Formation of SnO_2 gels from dispersed sols in aqueous colloidal solutions," *Journal of Non-crystalline Solids*, vol. 121, no. 1-3, pp. 76-83, 1990.

[10] F. M. Hossain, J. Nishii, S. Takagi, A. Ohtomo, T. Fukumura, H. Fuhiok, H. Ohno, H. Koinuma, and M. Kawasaki, "Modeling and simulation of polycrystalline ZnO thin film transistors" *J. Appl. Phys.*, vol. 94, no. 12, pp. 7768-7788, 2003.

[11] F. J. Yusta, M. L. Hitchman, and S. H. Shamlian, "CVD preparation and characterization of tin dioxide films for electrochemical application", *J. Mater. Chem.,* vol. *7*, no. 7, pp. 1421-1427, 1997.

[12] J. Nishino, S. Ohshio, H. Saitoh, and K. Kamata, "Tin dioxide prepared by a rapid chemical vapor deposition, *Mater. Res. Soc. Symp. Proc.*, vol. 363, no. 363, pp. 225-230, 1995.

[13] G. Horowitz, and P. Delannoy, "An analytical model for organic based thin film transistors," *J. Appl. Phys.,* vol. 70, no. 1, pp. 469-475, 1991.

[14] G. Horowitz, M. E. Hajlaoui, and R. Hajlaoui, "Temperature and gate voltage dependence of hole mobility in polycrystalline oligothiophene thin film transistors," *J. Appl. Phys.*, vol. 87, no. 9, pp. 4456-4463, 2000.

[15] M. K. Ryu, S. Yang, H. K. Park, C. S. Hwang, and J. K. Jeong, "High performance thin film transistor with cosputtered amorphous Zn-In-Sn-O channel: Combinatorial approach," *Appl. Phys. Lett.*, vol.95, pp. 072104-072106, 2009.

[16] L. Pichon, A. Mercha, R. Carin, O. Bonnaud, T. Mohammed-Brahim, Y. Helen, and R. Rogel, "Analysis of the activation energy of the subthreshold current in laser and solid phase crystallized polycrystalline silicon thin film transistors," *Appl. Phys. Lett.*, vol.77, no. 4, 576-568, 200.

[17] M. K. Ryu, S. Yang, H. K. Park, C. S. Hwang, and J. K. Jeong, "Impact of Sn/Zn ratio on the gate bias and temperature induced instability of Zn-In-Sn-O thin film transistors," *Appl. Phys. Lett.,* vol. 95, no. 17, pp. 173508-173510, 2009.

[18] A. Cerdeira, M. Estrada, R. Garcia, A. Ortiz-Conde, and F. J. Garcia Sanchez, "New procedure for the extraction of basic a-Si:H TFT model parameters in the linear and saturation regions," *Solid-State Electronics*, vol. 45, pp. 1077-1080, 2001.

[19] S. Mansouri, G. Horowitz, and R. Bourguiga, "Modeling of mobility in organic thin film transistor based octithiophene (8T)," *Synthetic Metals*, vol. 160, pp. 1787-1792, 2010.

[20] S. Luan, and G. W. Neudeck, "An experimental study of the source/drain parasitic resistance effects in amorphous silicon thin film transistors," J. Appl. Phys., vol. 72, pp. 766-772, 1992.

[21] Y. Xu, R. Gwoziecki, I. Chartier, R. Coppard, F. Balestra, and G. Ghibaudo, "Modified transmission line method for contact resistance extraction in organic field effect transistors," *Appl. Phys. Lett.*, vol. 97, pp. 063302, 2010.

[22] S. Bhaskar, S. B. Majumder, P. S. Dobal, R. S. Katiyar, A. L. M. Cruz, and E. R. Fachini, "Effect of precursor sol aging on sol-gel derived ruthenium oxide thin films," *Mat. Res. Soc. Symp. Proc.*, vol. 606, pp. 211-216, 2010.

[23] C. D. Dimitrakopoulos, I. Kymissis, S. Purushothaman, D. A. Neumayer, P. R. Duncombe, R. B. Laibowiz, "Low voltage, high mobility pentacene transistors with solution processed high dielectric constant insulators," *Adv. Mater.*, vol.11, pp. 1372-1375, 1999.

[24] S. Lee, D. J. Yun, S. W. Rhee, K. Yong, "Atomic layer deposition of hafnium silicate film for high mobility pentacene thin film transistor applications," *J. Mater. Chem.*, vol. 19, pp. 6857-6864, 2009.

[25] M. G. Kim, M. G. Kanatazidis, A. Facchetti, T. J. Marks, "Low temperature fabrication of high performance metal oxide thin film electronics via combustion processing," *Nature Materials*, vol.10, pp. 382-388, 2011.

[26] H. S. Kim, P. D. Byrne, A. Facchetti, T. J. Marks, "High performance solution processed indium oxide thin film transistors," *J. Am. Chem. Soc.*, vol. 130, pp. 12580-12581, 2008.

[27] G. Adamopoulos, S. Thomas, D. D. C. Bradely, M. A. Mclachlan, T. D. Anthopoulos, "Low voltage ZnO thin film transistors based on Y2O3 and Al2O3 high-k dielectrics deposited by spray pyrolysis in air," *Appl. Phys. Lett.*, vol.98, pp. 123503, 2011.

[27] H. M. Chenari, H. Ali, M. M. Golzan, H. Sedghi, and M. Talebian, "Frequency dependence of ultrahigh dielectric constant of novel synthesized SnO_2 nanoparticles thick films," *Current Applied Physics*, vol. 11, pp. 409-413, 2011.

[29] B. H. Venkataraman, and K. B. R. Varma, "Frequency-dependent dielectric characteristics of ferroelectric $SrBi_2Nb_2O_9$ ceramics," *Solid State Ionics*, vol.167, pp.197–202, 2004.

[30] D. Ravinder, G. R. Mohan, Prankishan, Nitendarkishan, and D. R. Sagar, "High frequency dielectric behavior of aluminium substituted lithium ferrites," *Materials Letters*, vol. 44, pp. 256-260, 2000.

[31] G. B. Kumar, and S. Buddhudu, "Optical, thermal and dielectric properties of $Bi_4(TiO_4)_3$ ceramic powders," *Cerem. Int.*, vol. 36, pp. 1857-1861, 2010.

[32] T. Nishide, T. Yabe, N. Miyabayashi, and M. Sano, "Analysis of Firing Processes of Titania Gel Films Fabricated by Sol-Gel Processes," *Thin Solid Films*, vol. 467, pp. 43-49, 2004.

[33] K. Kukli, K. Forsgren, M. Ritala, M. Leskela, J. Ararik and A. Harsta, "Influence of growth temperature on properties of zirconium dioxide films grown by atomic layer Deposition," Journal of Applied Physics, vol. 95, pp. 1833-1840, 2002.

[34] D. Y. Shin, and K. N. Kim, "Electrical and optical properties of MgO films deposited on soda lime glass by a sol-gel process using magnesium acetate," *Journal of ceramic processing research*, vol. 10, pp. 536-540, 2009.

[35] Y. Wu, M. J. Forbess, S. Seraji, S. J. Limmer, T. P. Chou, and G. Cao, "Oxygen vacancy related dielectric relaxation in $SrBi_2Ta_{1.8}V_{0.2}O_9$ ferroelectrics," *J. Appl. Phys.*, vol. 89, pp. 5647-5652, 2001.

Chapter 4 High Performance Inkjet-Printed Tin Oxide Transistors

4.1. Introduction

As shown in previous chapters, solution-processed SnO_2/ZrO_2 TFTs show extremely promising TFT characteristics. In particular, we were able to realize very high mobility devices using solution-processed ZrO_2 and SnO_2 layers. To fabricate those devices, commercial ITO deposited glass substrates was used and Cr/Au or Au source and drain electrodes were formed by thermal evaporation. Combining the aforementioned attractive properties of SnO_2 and ZrO_2 with the process benefits of inkjet printing, fully ink-jet printed SnO_2 TFTs will be well matched with the main goals of this field, i.e., to improve process throughput for large area panels, to lower the fabrication cost, and to improve device performance. To do that, it is first necessary to select the suitable inks for inkjet printing. The aforementioned liquid phase sol-gel precursors have been considered as the inks for the printing system, to take advantage of their properties. It is also necessary to understand the main mechanisms of stable droplet formation in inkjet systems. Then, the shapes of the deposited droplets may be predicted and controlled, based on the behavior of the droplets on the relevant surfaces. In this chapter, we introduce three inorganic metal oxide ink-jet inks for the electrodes (Sb-doped SnO_2), semiconductors (SnO_2) and insulators (ZrO_2). New functionalities of well-known chemical stabilizers such as ethylene glycol (EG) and monoethanolamine (MEA) used in sol-gel systems are suggested to control the topology and to suppress the coffee ring effect in the ink-jet printing systems. In addition, we introduce a technique to create uniform inorganic metal oxide layers through ink-jet printing by employing a thin organic buffer layer and by increasing the viscosity of the primary solvent in the mixture. First, printing with a low-viscosity solvent as the dominant solvent in the mixture is possible. Second, we can deposit uniform thin layers without the coffee-ring effect by controlling the spreading speed and evaporation rate using a high-viscosity solvent mixture. Finally, transparent metal-oxide-based transistors can be fabricated with no coffee-ring effect on glass substrates using ink-jet printing to create uniform multi-layer stacked structures that consist of a bottom Sb-doped SnO_2 (ATO) gate electrode, a ZrO_2 insulator, an ATO source/drain electrode and an SnO_2 semiconductor with a high mobility of 20 cm^2/Vs, a 10^4 on/off ratio and a 0.18 V/decade sub-threshold slope.

4.2. Sn-doped SnO_2 films

All reagents were purchased from Aldrich and were used as received. To produce ATO electrodes, an SnO_2 liquid precursor was prepared by dissolving 0.001 mol

$SnCl_2 \cdot 2H_2O$ in a mixture a mixture of ethanol and ethylene glycol with varying quantities of $SbCl_3$ as a dopant. To measure sheet resistance and to extracted a resistivity, 100 nm thick ATO films were deposited on glass substrates by spin-coating at 3000 rpm for 30 sec, five times. The post annealing process was conducted at 400 ºC, 450 ºC, and 500 ºC for different process times.

The variation in sheet resistivity of the ATO films (~100 nm thick) with different $SbCl_3$ compositions and annealing conditions in air are summarized in Figure 4.1(a). and Table 4.1. The resistivity initially decreased with increasing processing time to approximately 0.04 ohm·cm at 500 °C for 15 min with 8 wt% $SbCl_3$ and then increased slightly with the processing time. The increased resistivity of the ATO films with a longer heating process can be explained by oxygen vacancy scattering. Figure 4.1(b) shows the XRD data corresponding to the ATO films formed with 8 wt% $SbCl_3$ after heating at 500 °C for 15 min in air. The inset shows the optical image of ATO film on a glass substrate, after completion of the post annealing process. These results are in agreement with the SnO_2 reference data (JCDPS: 411445), and no significant byproducts, such as Sb_2O_3, were formed.

Figure 4.2 shows the optical images of ATO films sintered at 500 ºC for 15 mins in air and in vacuum on glass substrates and the extracted resistivity of ATO films sintered in different annealing conditions. The ATO films sintered at 500 ºC for 15 mins in vacuum were brown and much less conductive than ATO films sintered at 500 ºC for 15 mins in air. It is well know that when the heat-treatment temperature increases, a possible competition exists between the two oxidation states (Sb^{5+} and Sb^{3+}) of antimony. Sb^{5+} dominated and led to the decrease in the sheet resistance at high temperatures and Sb^{3+} played a role as a p-type dopant at low temperature but did not contribute to conduction [1], [2]. Under higher temperature annealing in air, Sb^{3+} was oxidized into Sb^{5+}, resulting in the observed dependence of resistivity on annealing temperature and ambient.
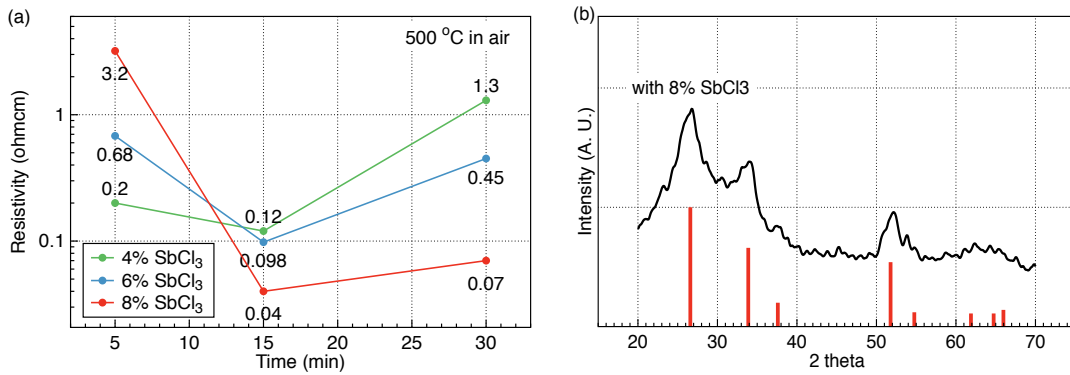

Figure 4.1 (a) The measured resistivity of deposited Sb doped SnO_2 films at 500 ºC in air, corresponding to different process time and different $SbCl_3$ weight percent. (b) The measured resistivity of deposited Sb doped SnO_2 films sintered at 500 ºC in air, corresponding to different process times and different $SbCl_3$ weight percent.

Temperature (ºC)	Weight percent of SbCl$_3$	Process Time (mins)			
		5	15	30	60
400	0	0.58	2.8	-	-
	2	0.91	2.6	-	-
	4	0.33	2.4	-	-
	6	-	2.3	-	-
	8	-	5.0	-	-
450	0	8.0	4.4	5.0	5.4
	2	3.4	2.5	8.4	-
	4	0.18	0.12	1.3	-
	6	-	-	-	-
	8	-	-	-	-
500	0	-	-	-	-
	2	-	-	-	-
	4	0.2	0.12	1.3	-
	6	0.68	0.098	0.45	-
	8	3.2	0.04	0.07	-

Table 4.1 The measured resistivity (ohm·cm) of Sb-doped SnO$_2$ films, corresponding to varying sintering process temperature and process time with different SbCl$_3$ weight percent.
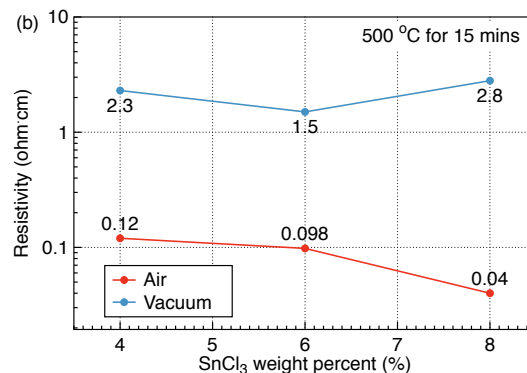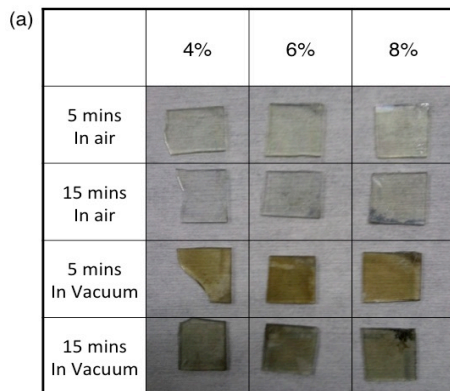

Figure 4.2 (a) Optical images of ATO films sintered at 500 ºC for 15 mins in air and in vacuum on glass substrates with different SbCl$_3$ weight percent and (b) The extracted resistivity of sintered ATO films.

The high contact resistances of source and drain electrodes of TFTs can contribute to TFT performance degradation. The on current is decreased and the operation voltage is higher than expected as a consequence of the voltage drop across the channel being reduced due to the significant voltage drops at the contacts. In addition, as the channel length decreases, the contact resistance is the dominant resistance of the overall device resistance. We can not take full advantage of short channel TFTs as a consequence of this. Therefore, to use the ATO films as the source and drain electrodes for TFTs, the sintering process should be conducted at 500 ℃ for 15 mins in air to minimize the resistivity of ATO films. Based on this, when we design the TFT fabrication process flows, those sintering conditions for ATO source and drain electrodes are the high priority condition of the total thermal budget design and allocation.

4.3. Ink-jetted ATO electrodes

Ink-jet techniques present two main challenges. First, the inks must be able to generate droplets. The surface tension, surface temperature, ink viscosity and nozzle diameter determine the figures of merit, such as the Weber, Ohnesorge and Reynold's numbers, which are listed in table 4. 2 [3]-[5]. The stabilities of the generated drops were estimated using the Z number, which is the inverse of the Ohnesorge number. If the Z number is too small, the ink is too viscous to form stable drops. If the Z number is too large, satellite drops are generated [5]. The experimentally confined Z numbers of the systems ranged from $7.8 < Z < 18.9$ to form the stable drops. Below 7.8, viscous dissipation prevents drop ejection. Even when Z was 18.0, stable single drops were formed without any satellite drops. The extracted Weber values were not within the well-established optimal range for stable printing, but were near the optimal range. Several groups have reported stable ink-jet printing with a Z number outside the well-established optimal range. After impinging on the substrates, the homogeneity of the final printed features is another key factor in determining the performance level and reliability of ink-jet printed electronic devices. The drop movement on a surface is explained by fluid dynamics related to the gravitational force, impact inertia, surface tension, evaporation rate, capillary motion and the Marangoni flow inside the solvents. To confirm the driving force for jetted drops, we considered the Bond number, $B = \varrho g a^2 / \gamma$, where ϱ is the density, g is the acceleration of gravity, a is the diameter of the orifice, and γ is the surface tension [6]. The calculated Bond number was smaller than 1; therefore, the gravitational force was neglected. The Weber number is important for understanding the dynamics of spreading. The calculated Weber number was higher than 1, which indicates that the jetted drop liquid is driven radially outward by the pressure originating from the impact and not capillary motion. The force resisting the spreading was scaled by the Z number. At high Z numbers, the viscosity reduces ink spreading, and at low Z numbers, the inertia reduces ink spreading [4].

Ethanol (ml)	EG (ml)	Surface Tension (mN/m)	Viscosity (mPas)	Density (g/cm^3)	Velocity (m/sec)	Reynold	Weber	Ohnesorge	Z
10	0	21.8	1.20	0.79	6	118.4	39.1	0.0528	18.9
9	1	23.0	1.63	0.82	6	90.6	38.5	0.0658	14.6
7	3	25.0	2.90	0.89	6	55.2	38.4	0.1122	8.9
5	5	28.3	4.90	0.95	6	34.9	36.3	0.1725	5.8
0	10	48.5	16.00	1.12	6	12.6	24.9	0.3959	2.5

Table 4.2 Summarized of physical properties and dimensionless numbers for each system.

We employed ethanol instead of using 2-methoxyethanol as the major solvent to create less toxic sol-gel systems and increase the speed of the chemical reactions, such as de-etherization in alcohol. We printed inks onto SiO_2/Si substrates and formed lines to confirm the viability of our precursor inks and to investigate the line morphology. An 8% $SbCl_3$ added to the ATO precursors (in 10 mL ethanol) was used as the ink to print the transparent electrodes.

Figure 4.3 and 4.4 are optical images of the deposited ATO drops, by varying the number of drops at the same position. In case of a pure ethanol system, the evaporation rate of ethanol at room temperature is relatively fast, and thus the diameters of deposited ATO films are almost same, regardless of the number of drops. In contrast, the diameter of ATO films formed using ethylene glycol (EG)-based inks is proportional to the number of drops. Since the boiling temperature of EG is higher than that of ethanol, the pre-deposited ATO drop is not dried fully and it merges with the post deposited drop and spreads further before drying is complete.
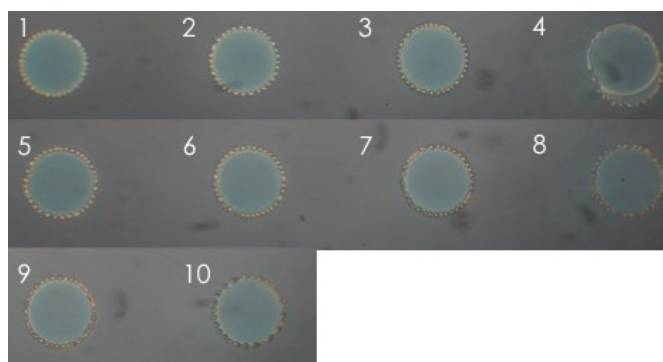

Figure 4.3 The ink-jetted ATO inks on UV/Ozone treated SiO_2 surface.
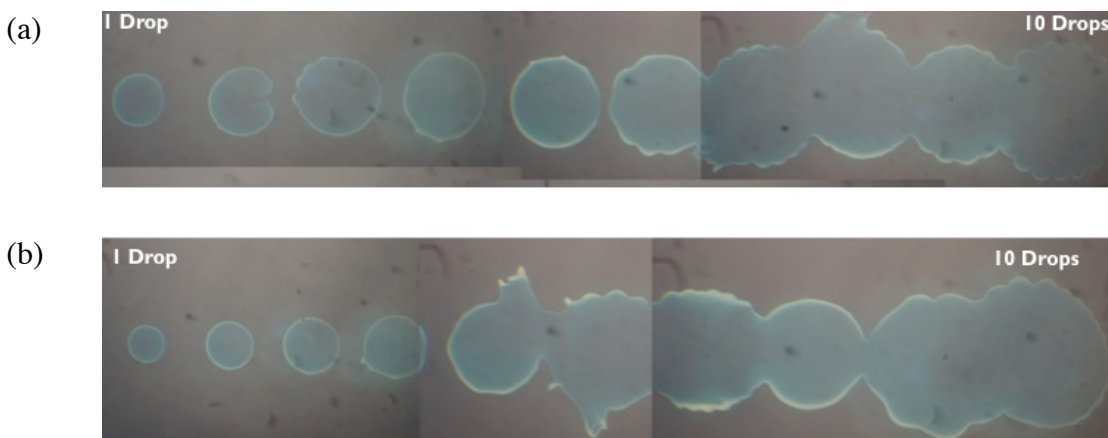The number at corner is the number of dropped inks.

(a)

(b)

Figure 4.4 The ink-jetted ATO inks on UV/Ozone treated SiO_2 surface.
(a) 1 ml EG added ATO inks and (b) 3 ml EG added ATO inks

The morphology of the ATO lines printed on 10-min UV/ozone-treated SiO_2 substrates with varying substrate temperatures were obtained and are plotted in Figure 4.5(a). The optical images and the WYKO images exhibit a significant dip in their centers, the so-called "coffee ring" effect. This effect is commonly described by two different mechanisms, determined by various velocity parameters: the impact driven regime and the capillary force driven regime.

The impact-driven regime may be explained as follows. Initially, due to the velocity of the generated droplets (~ 6 m/s), the impact inertia causes the central area of each droplet to sink below the surrounding areas. At this moment, if the evaporation rate of the solvent is sufficient, the thin central area dries faster than the surrounding area. The evaporation rate increases as the surface approaches the preheated substrates. The sunken and dried central region of the ink droplets prevents the movement of the ink, which accumulates at the rims and dries. When pure ethanol was used as the solvent for the ink, the evaporation was too rapid to allow the ink to move back into the thin central region. Then, the deposited drop spread outward driven by capillary force (the capillary force driven regime). In the capillary force driven regime, the increased surface tension between the UV/ozone treated SiO_2 substrate and the ethanol reduced the contact angle. The faster evaporation at the rims, originating from the small contact angle, accelerated the evaporation at the edge, which intensified the outward radial flow to replenish the loss of the evaporated solvent. This increased spreading speed resulted in wider features with thinner central regions.

During ATO line deposition, when the second droplet impacted the substrate, it merged with the ink that had already been deposited. Due to the splash effect originating from the velocity of generated drops and the low contact angle, the second droplet partially overlapped the first droplet and exhibits the same concave shape as the first droplet. Overall, strongly coffee ringed structures were formed.

The amplitudes of the pattern waviness are summarized in Figure 4.7. The amplitude of waviness at the center is lower than that of the corner. Finally, continuous wavy ATO lines were formed, consisting of concave ATO dots. To control the geometry of deposited droplets, the substrate temperature was varied. Increasing the substrate

temperature boosted the evaporation rate of the solvent-printed ATO droplets and resulted in narrower ATO electrode lines with increased height. The increased height delayed the drying time in the central region. The ratio of the sidewall height to the height in central region was reduced; however, similar wavy ATO lines were still formed. To eliminate the wavy ATO electrodes that originated from the more rapid drying process in the thin central region of each droplet, a trial was conducted to decrease this evaporation rate by adding specific solvents, such as EG, with higher boiling points. As the ratio of EG to ethanol increased to 1 mL EG: 9 mL ethanol, the wavy shape in the central region disappeared at low temperatures. Adding a higher boiling point solvent to the mixture delayed the overall drying time. However, as the substrate temperature increased to 70 °C, the wavy shape returned. At 70 °C, the evaporation rate of the mixture containing 1 ml EG and 9 mL ethanol is sufficient to completely dry the sunken central region created by the impact. When 3 mL EG was mixed with 7 mL ethanol at low temperature, the deposited ink spread further and wave-free ATO electrodes were obtained. At 70 °C, the ethanol, whose boiling point is 70 °C, evaporated more rapidly than the EG, and the EG became the major solvent. The higher boiling point of EG delayed the drying process and introduced a reflow motion in the center of the printed ATO lines. In addition, the spreading speed of the ATO ink was reduced, due to the high viscosity of the major solvent, EG. These factors lead to wave-free uniform ATO in the center and relatively narrow electrodes. Based on the defined parameters (Figure 4.6), the measured values are summarized in Figure 4.7-9. The sidewall height ratio of the main electrode height was reduced from 3.14 to 1.47, although the edges of the ATO electrodes were still higher than the center in Figure 4.5. and 4.9. At 110 °C, the evaporation rate increased sufficiently to reduce the drying time for both the low (ethanol) and high (EG) boiling point solvents, once again producing wavy ATO lines.
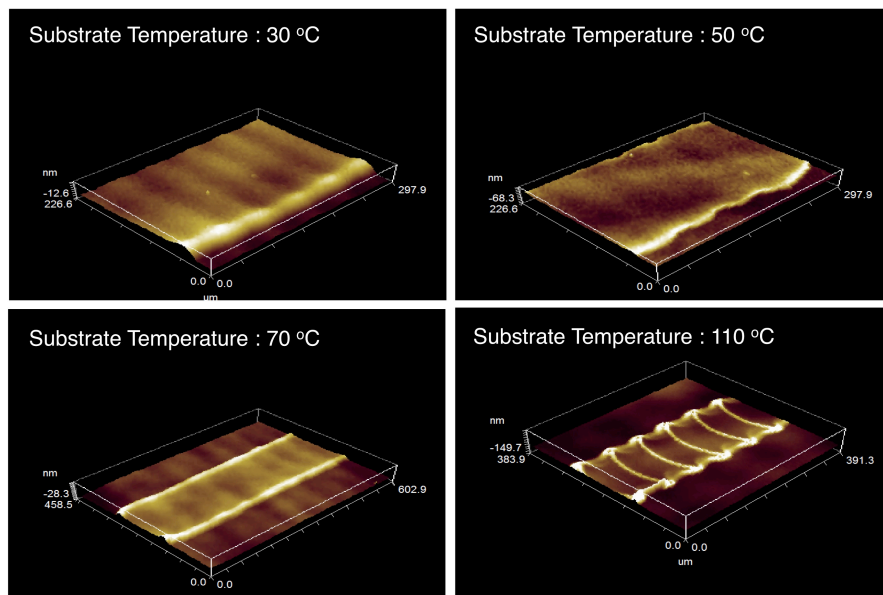
(a)
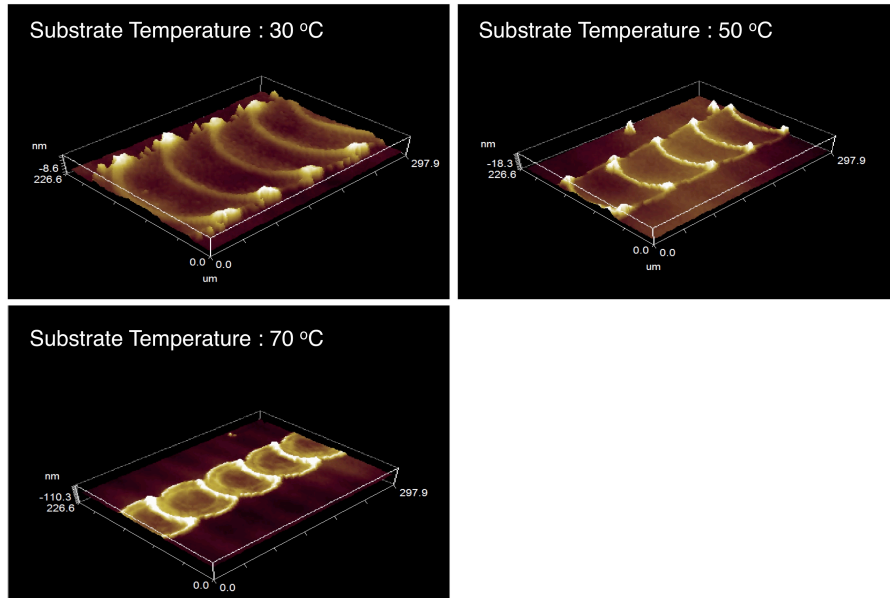
(b)
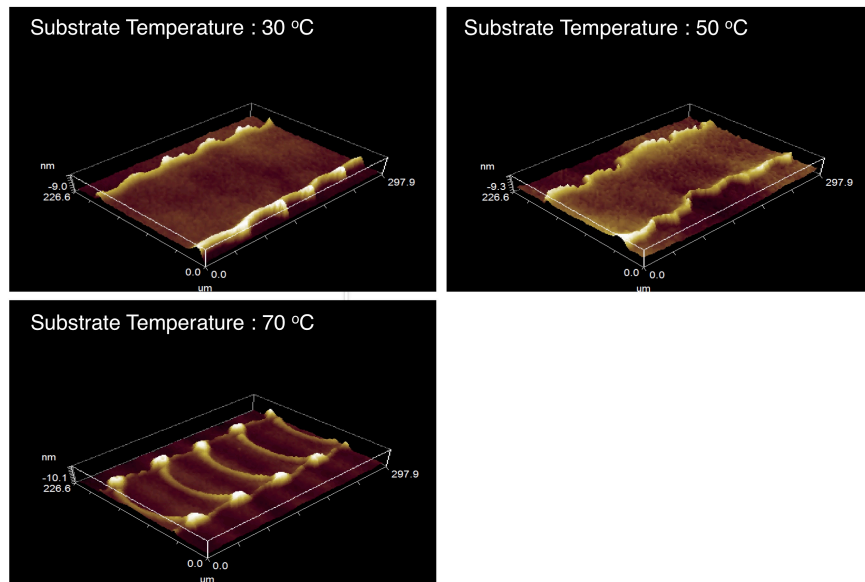
(c)

Figure 4.5 The WYKO images of printed ATO electrodes on SiO$_2$/Si substrates with different volume ratio EG of ethanol: (a) pure ethanol, (b) 1 ml EG and 9 ml ethanol and (c) 3 ml EG and 7 ml ethanol, respectively.
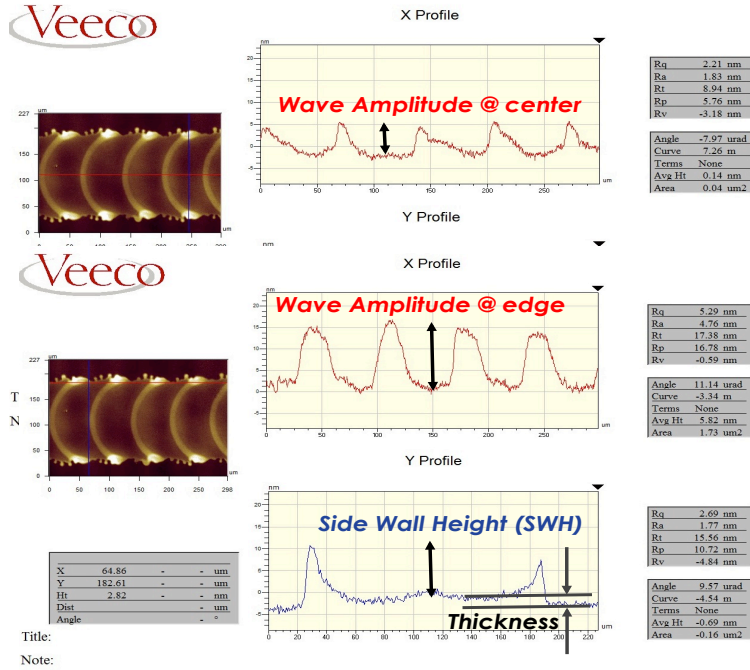
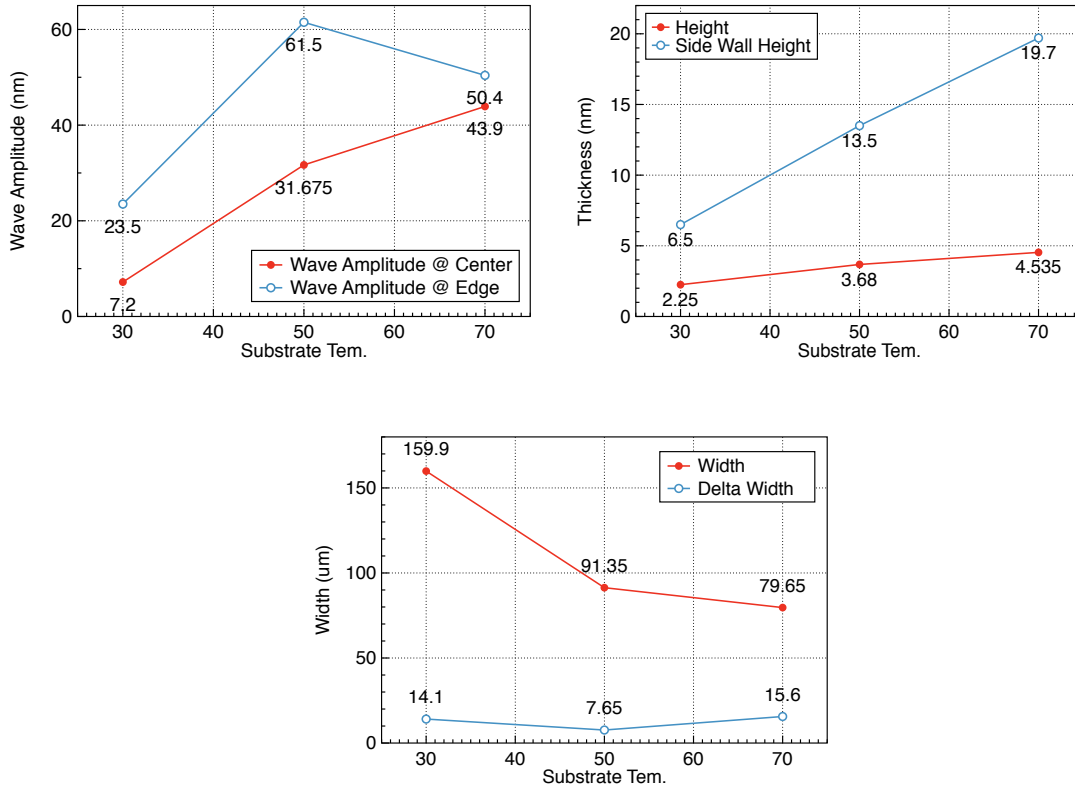Figure 4.6 The defined parameters to analyze printed ATO line morphology.

Figure 4.7 Summarized parameters for ink-jetted ATO line morphology.
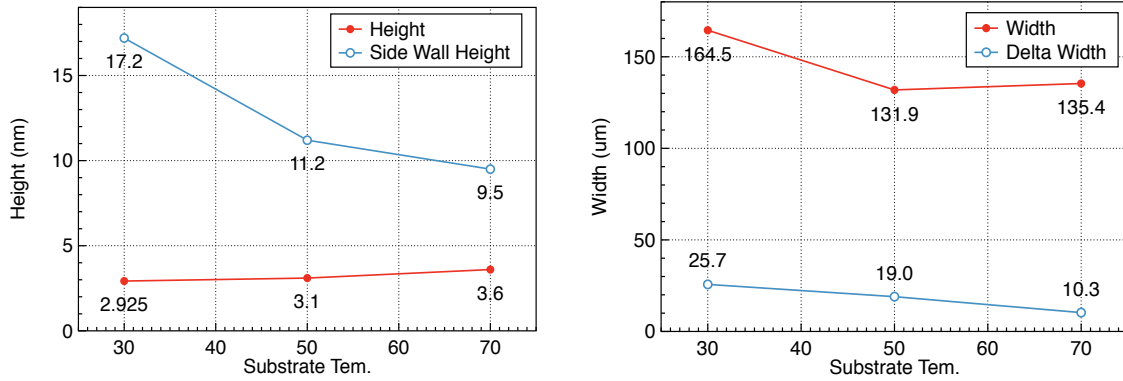The major solvent of these ATO inks is pure ethanol.

Figure 4.8 Summarized parameters for ink-jetted ATO line morphology.
The major solvent of these ATO inks is the mixture 1 ml EG and 9 ml ethanol.
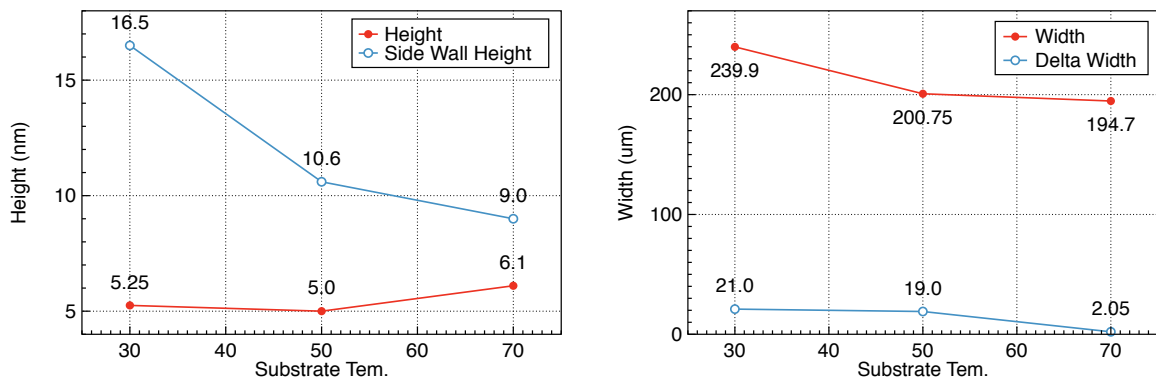

Figure 4.9 Summarized parameters for ink-jetted ATO line morphology. The major solvent of these ATO inks is the mixture 3 ml EG and 7 ml ethanol.

The impact of solution concentration on the ATO electrode morphology is investigated in Figure 4.10. The amount of dried solute increased with increasing concentration, which resulted in thicker ATO electrodes. The measured height of the central region and edge are summarized in Figure 4.11, from the cross sectional profile of each electrode. The increased dried solute concentration per unit drop thickened the electrode but maintained its width.
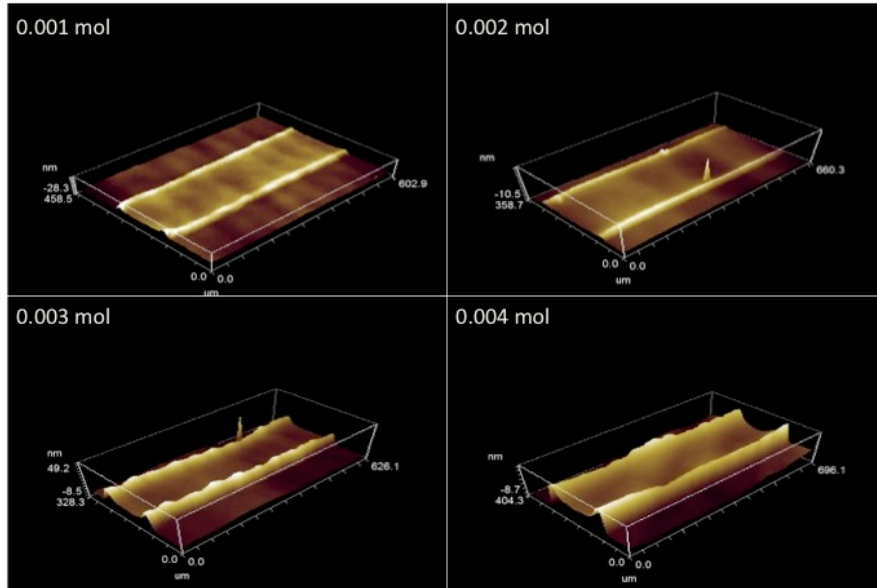
Figure 4.10 The WYKO profile images of printed ATO electrodes,
as a function of the concentration.
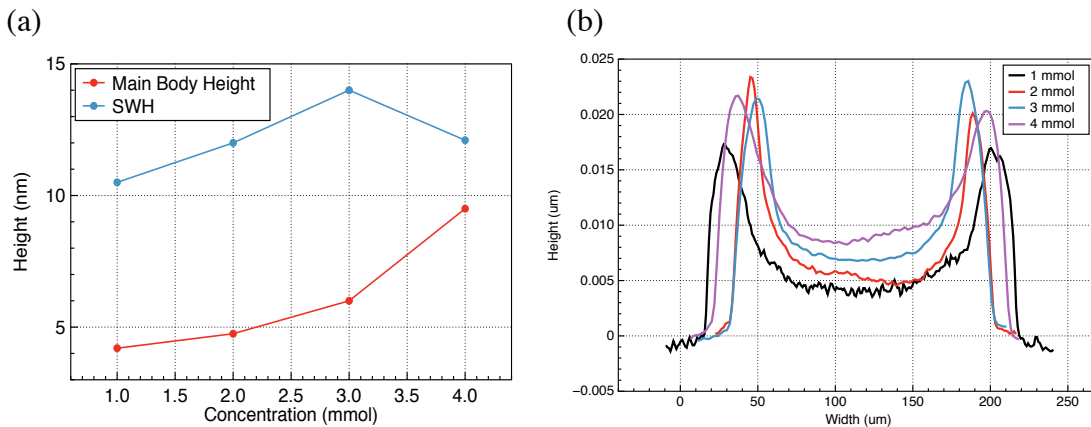
(a)

(b)

Figure 4.11 (a) Evaluated height of the main body and side-wall height of the printed ATO electrodes with different concentrations and (b) the cross-sectional profile images of each electrode.

Test TFTs were fabricated using the prepared inks in a mixture of 3 ml of EG and 7 ml of ethanol for the ATO and a mixture of 1 ml of EG and 7 ml of ethanol for SnO_2 films. Figure 4.13 provides the electrical characteristics of the test TFTs, which consisted of printed ATO S/D electrodes and printed SnO_2 semiconductors on thermally grown 100 nm-thick SiO_2/n++ Si substrates at 50°C. Figure 4.12 presents a schematic of the printed thin-film transistors and an optical image of the fabricated thin-film transistor with various numbers of printed semiconductor layers.
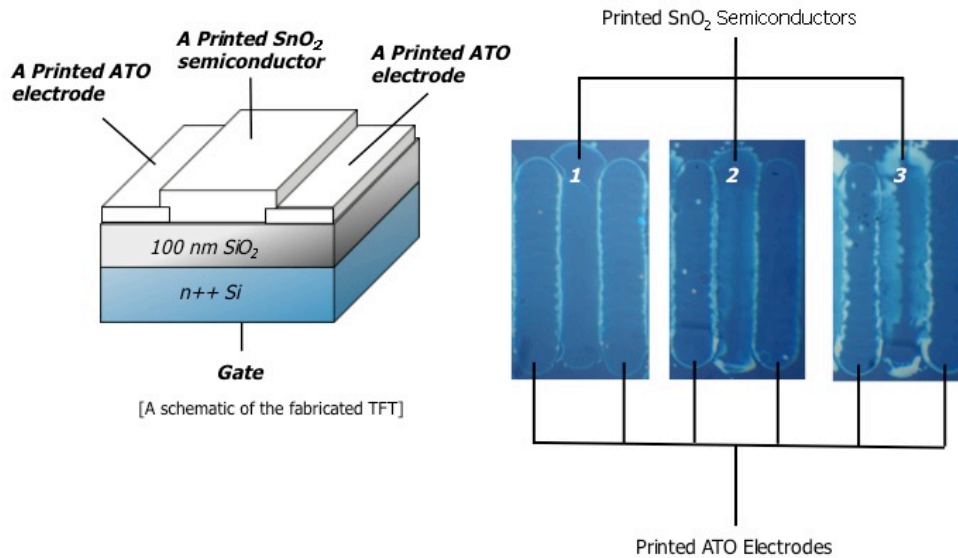
83

Figure 4.12 Schematic of the fabricated TFTs and optical images of TFTs, which consists of printed ATO electrodes, and SnO_2 semiconductors on SiO_2/Si substrates

Figure 4.13 presents the drain current versus drain voltage (I_d–V_d) curves for a representative TFT with a channel length of 150 μm and a width of 600 μm as a function of V_d in the range from 0-25 V with the selected V_g range from −50 to +50 V in 25 V increments. The fabricated TFTs exhibited a conventional n-type and normally on-state behavior with negative threshold voltages (V_{th}). An on/off current ratio (I_{on}/I_{off}) of approximately 10^6 and a sub-threshold slope (SS) of 2.5 V/decade were obtained for the TFTs, as shown in Figure in Figure 4.13. (b). The field effect mobility in the saturation regime, $\mu_{eff} \approx 3.0$ cm^2/Vs, was evaluated from a linear fit of the curve for $I_d^{0.5}$ versus Vg (Figure 4.13. (b)).
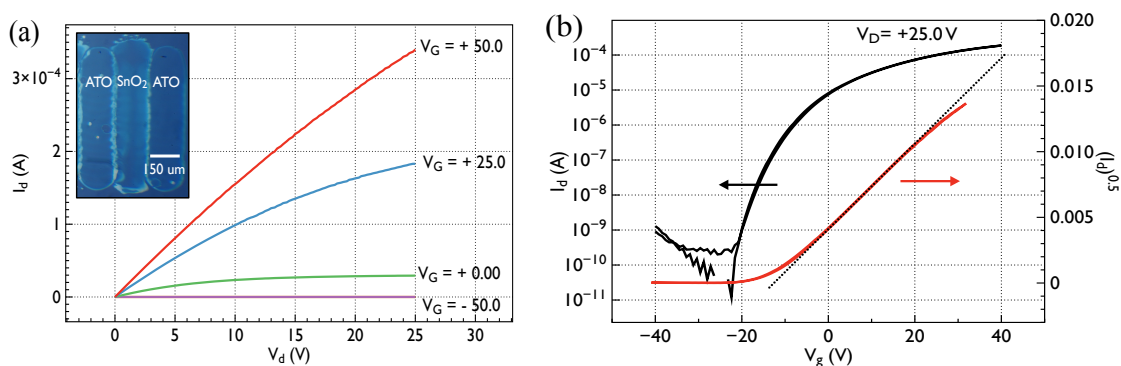

Figure 4.13 Representative electrical characteristics of printed ATO S/D and printed SnO_2-based devices on SiO_2/Si substrates (a) I_d-V_d and (b) I_d-V_g (left axis) and $I_d^{0.5}$-V_g (right axis).

84

Figure 4.14 shows statistics of the electrical characteristic parameters of the fabricated thin-film transistors. The field-effect mobility in the saturation regime was increased by 20-fold when the SnO_2 semiconductor layer was deposited in multiple layers to increase the channel thickness and coverage. The measured film thickness of the printed mono-layer was approximately 5 nm. In contrast, the SnO_2 layers were thicker than 15 nm in the SnO_2 layer that was multilayer deposited two or three times, which increases the conductivity of the semiconductor layers and promotes the field-effect mobility in the saturation regime. However, when the SnO_2 layers were deposited three times, some devices exhibited a lower on/off current ratio due to back-channel effects. In addition, the gate controllability was poor, as confirmed by the larger SS values.
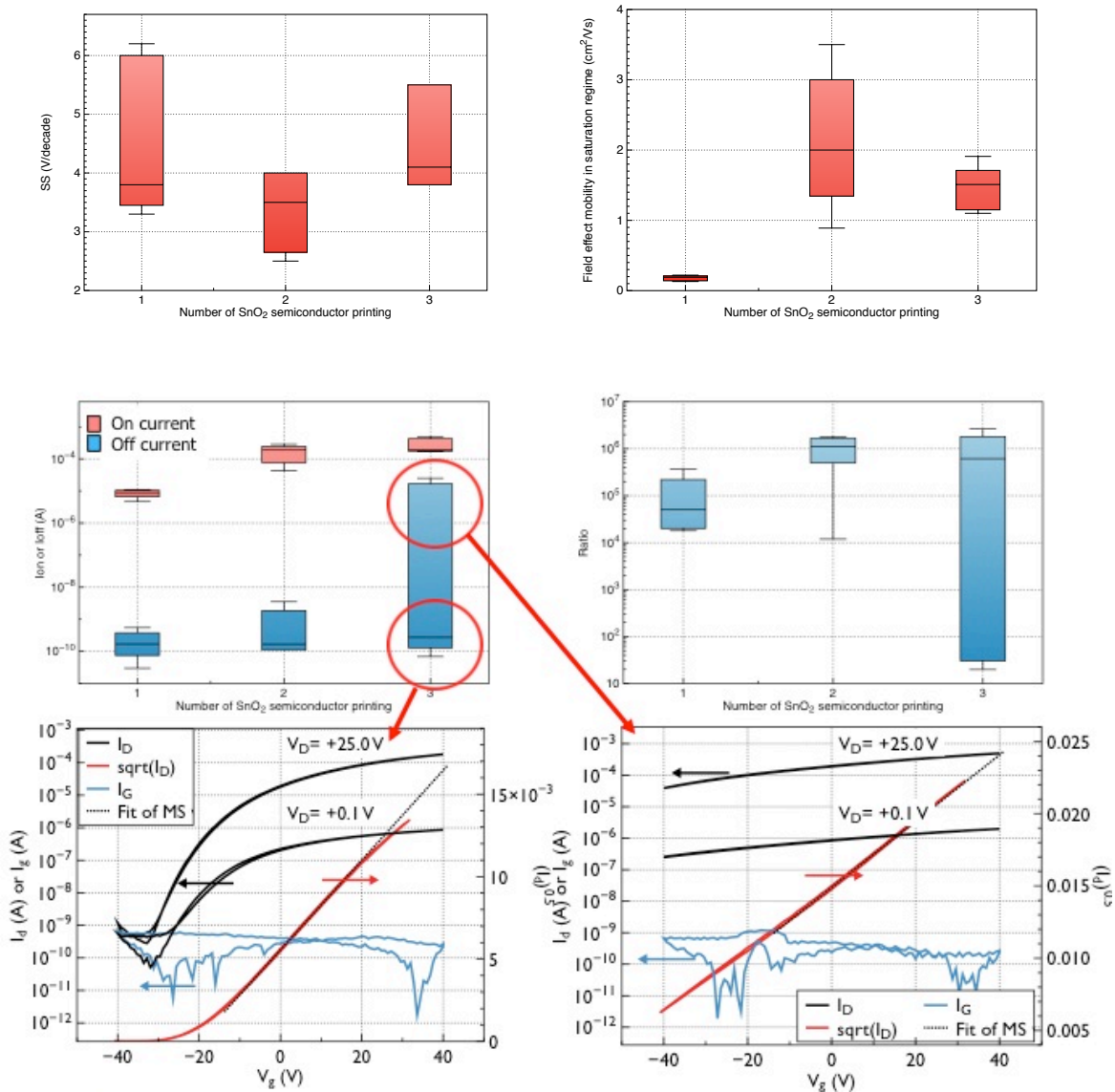

Figure 4.14 Statistics of transistor characteristic parameters and an example of poor performance observed in three-layer SnO_2 based transistors

The contact resistance values of the printed ATO electrodes were extracted using the TLM, as discussed in Chapter 3. The width-normalized total resistance values were plotted as functions of the channel length. When the channel length is zero, the extrapolated total resistance of the channel length is equal to the contact resistance. Figure 4.15 presents the total resistance of the fabricated thin-film transistor with printed ATO source/drain electrodes as a function of the channel length with different biased gate voltages. The total resistance values were extracted from different channel lengths of 55, 90, and 144 μm. The extracted contact resistance values were approximately 15 kΩ.
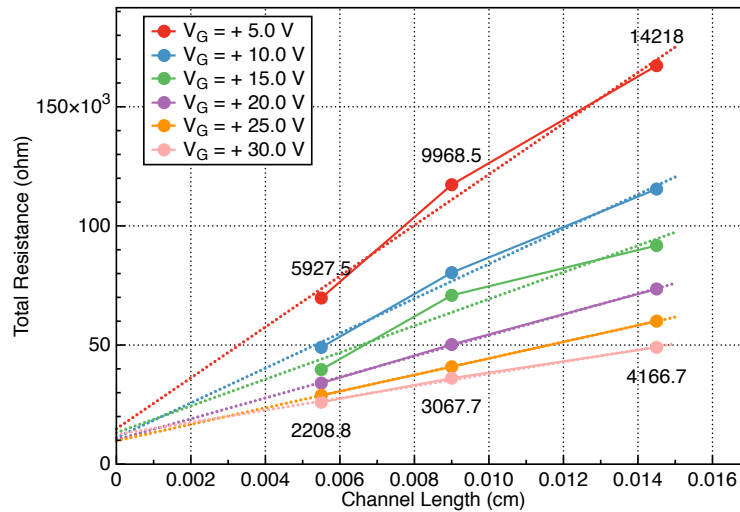

Figure 4.15 Extracted total resistance as a function of the channel length with different biased gate voltages from the fabrication thin-film transistor with printed ATO source/drain electrodes.

To create fully printed TFTs, we used patterned gate structures. To use the printed lines as the bottom-gate electrodes, a uniform line is critical for uniform layers of insulators, S/D electrodes or semiconductors. Although wave-free lines were successfully formed on the UV/ozone-treated SiO_2 substrates, the addition of EG and an increased substrate temperature did not completely eliminate the coffee-ring effect. Based on the established theory, the behavior of a droplet impinging on a substrate is affected by the impact velocity, droplet diameter, viscosity, and surface energy. In fact, the ink-jetted ATO inks (in the mixture of 3 ml of EG and 7 ml of ethanol) on a hydrophobic surface did not exhibit the coffee-ring effect at their edges. Figure 4.16 presents the printed ATO patterns on old SiO_2 substrates as a function of the delay time with different substrate temperatures. Here, the old SiO_2 substrates indicated that the surface of pristine hydrophilic SiO_2 had been exposed to organic contamination for a period of time, and its surface exhibited increasingly hydrophobic characteristics until an additional process was conducted to change it into a hydrophilic surface, such as O_2 plasma or UV/ozone cleaning. At 50°C, the surface energy was low, and the printed patterns separated into beads or rods because of the relatively larger cohesion force between the inks. As the

substrate temperature increased, the movement of the dropped inks was delayed because of the increased evaporation rate. At 90°C, continuous ATO patterns were formed regardless of the delay time. These results indicate that the control of the surface energy plays a role in the formation of uniform ATO lines without the coffee-ring effect. However, more-established approaches are required to obtain repeatable and controllable results.

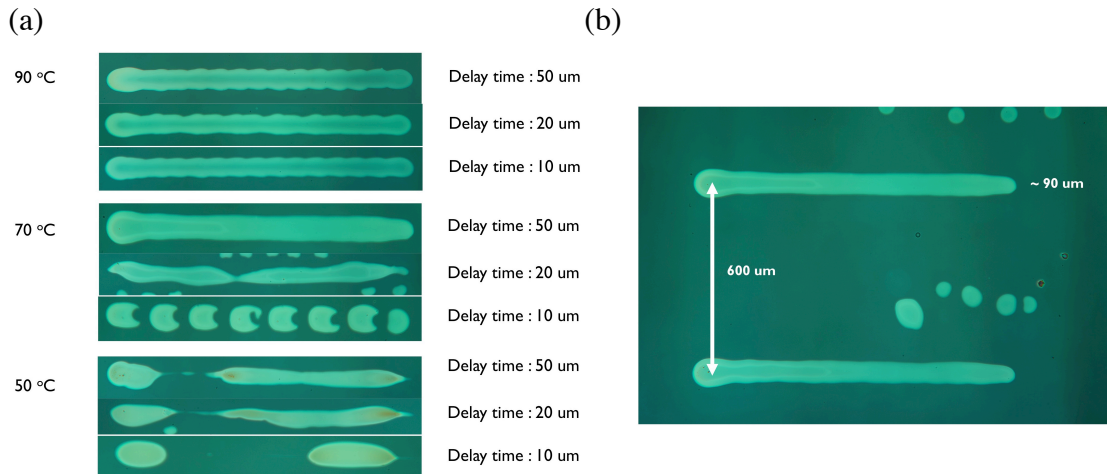(a)   (b)

Figure 4.16 (a) Printed ATO electrode lines on hydrophobic substrates as a function of the delay time with different substrate temperatures. (b) Optical image of ATO electrodes without the coffee-ring effect.

The next approach considered to change the surface characteristic of SiO_2 was the Hexamethyldisilazane (HMDS) treatment. Water is normally adsorbed on the polar surface of SiO_2. After the HMDS treatment, the surface oxide is silated and creates a non-polar surface. The hydrophobic SiO_2 surface energy can also be controlled by conducting UV/ozone treatment again; the surface energy varies as a function of the exposure time. Figure 4.17 presents the WYKO images of the printed ATO electrode lines on HMDS-treated SiO_2 substrate as a function of the UV/ozone process time with different substrate temperatures. However, the surface energy remained relatively low after 3 min of the UV/ozone process. As the UV/ozone process time increased, the separated ink droplets combined with one another and formed a uniform island. The merging of the droplets was limited as the substrate temperature increased because of the rapidly evaporating solvent, which resulted in a coin-stack structure.
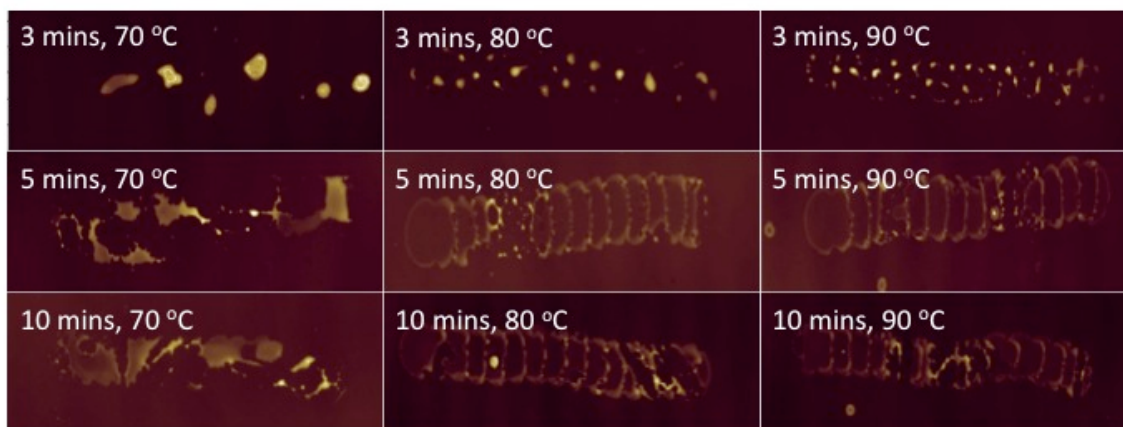
Figure 4.17 (a) WYKO images of printed ATO electrode lines on HMDS treated SiO_2 substrates as a function of substrate temperatures with different UV/Ozone process times.

Considering the aforementioned results on treated and untreated SiO_2 substrates, PMMA layers were used as buffers to control the surface energy on the glass substrates prior to printing. The increased surface energy was confirmed by contact angle measurements performed with the prepared ATO ink in a mixture of 3 ml of EG and 7 ml of ethanol. UV/ozone treatment was also applied with various process times to control the surface energy. The change of the surface energy was confirmed by the measured contact angle values shown in Figure 4.18.
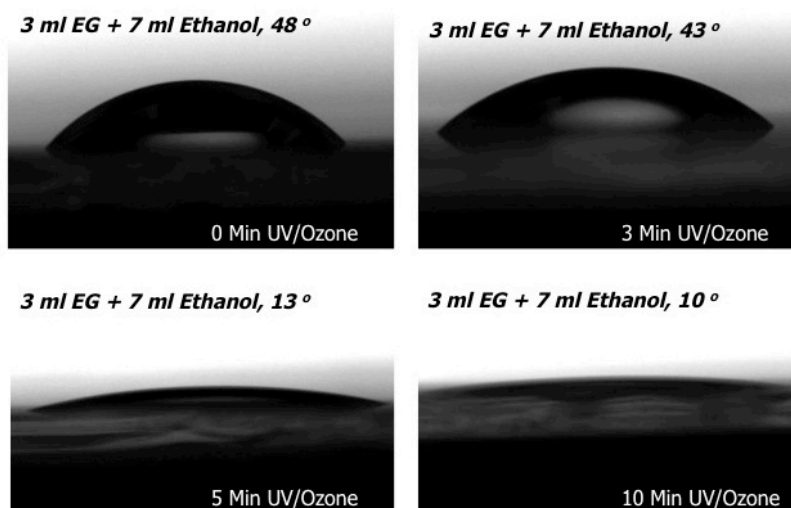

Figure 4.18 Measured contact angle of the mixture of 3 ml of EG and 7 of ml ethanol mixture on PMMA coated substrates as a function of the UV/ozone treatment process times.

Without the UV/ozone treatment, no continuous ATO lines formed on the hydrophobic surface. Separate beads were formed at room temperature. The ATO inks dropped onto the PMMA buffer layers maintained their contact angles. In addition, a high contact angle caused increased cohesion within the liquid, resulting in the printed lines breaking up to form spherical drops. After UV/ozone treatment for 10 min, the surface energy increased and caused less cohesion of the liquid. The inkjetted drops spread too far to obtain uniform ATO lines.

Thus, after a UV/ozone processing time of 5 min, the shape of each droplet and the line morphologies were investigated for each substrate temperature. Figure 4.19 provides the profiles of the typical drops formed using this process at the various substrate temperatures after treating the PMMA layers with UV/ozone for 5 min; the ink is a mixture of 3 mL EG and 7 mL ethanol.
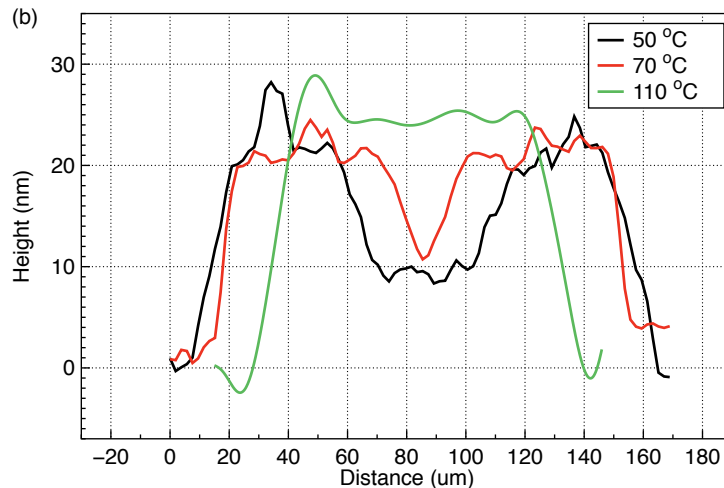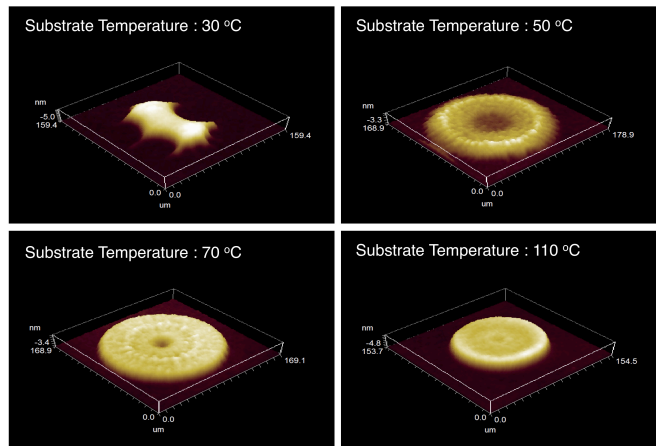
(a)

(b)

Figure 4.19 The morphology of printed ATO ink drop (precursors in the mixture of 3 ml EG and 7 ml ethanol) on 5 mins UV/Ozone treatment PMMA layers, for four different substrate temperatures. (a) WYKO images (b) Typical cross-sectional profiles.

At 50 °C substrate temperature during jetting, the patterns exhibited the coffee-ring-shaped concave structure. As the substrate temperature increased, the inks experienced more rapid evaporation, which led to a reduction in the droplet spread during the drying process. Flat disks were obtained at 110 °C. Based on the Marangoni flow effect, a co-solvent system with differing vapor pressures provides the best strategy for eliminating the coffee-ring effect [7], [8]. Using a specific combination of vapor pressure and surface tension with two different co-solvents, a reverse Marangoni flow can be generated to suppress outward flow. However, in this system, the vapor pressure of ethanol is higher than that of EG, and the surface tension of ethanol is lower than that of EG. This combination of vapor pressure and surface tension leads to Marangoni flow in the same direction as the spread, extending from the center of the droplet. Therefore, this mechanism cannot explain our results. Instead, our results must be explained by the dynamic behavior of the droplet as it impacts and spreads, considering the impact inertia and the time-dependent ink movement from the central region toward the edge. The estimated Weber number was higher than 1, which indicates that the flow was likely driven by the dynamic pressure of impact. As the EG volume increased, the viscosity of the ink increased, which increased the Z number and indicated that the spreading was limited by viscosity. This increased viscosity reduced the spreading speed, which led to a reduction in the area and an increase in the droplet height for the same volume of printed ink, increasing the contact angle. The increased contact angle plays a secondary role in decreasing the spreading speed of the droplet. In addition, when the droplets impinged on a pre-heated substrate, whose temperature was above the boiling point of ethanol (70 °C), ethanol was no longer the major solvent, and the highly viscous EG (boiling point: 197 °C) became the major solvent of the ink. The increased viscosity of the solvent dampened the amplitude of the recoiling oscillation, leading to increased dot height. When the center region sank due to the impact of the ink, the minimum height of the pendent droplet increased, decreasing the evaporation rate. The significant increase in the boiling point of the major solvent, EG, also increased the drying time in the sunken central region formed by the impact inertia. The coffee-ring effects found in the droplets on the SiO_2 substrates under the same conditions were not eliminated, which supports the idea that the initial contact angle which originates from the surface energy of the more hydrophobic PMMA layer, is the most critical factor in controlling the droplet morphology.

The availability of PMMA led to its use as the buffer layers between the substrates and the post ink-jetted layers. To produce conductive ATO layers, a 15-min processing time at 500 °C was needed (Table 4.1. and Figure 4.1.). However, the decomposition temperature of PMMA is approximately 300 °C. During the 500 °C processing, the complete removal of PMMA layers by thermal decomposition induces the collapse of the post deposited layers on the PMMA layer. Figure 4.20 (a) presents the WYKO images of the ATO with the PMMA layers after the heating process. Regardless of line morphology, all ATO electrodes were cracked, likely due to the decomposition of the underlying PMMA. To solve this problem, a thinner PMMA layer is required to minimize the volume changes. Figure 4.20 (b) presents the measured film thicknesses corresponding to different speeds and different PMMA concentrations. The film thickness of the PMMA layers on the glass substrates was approximately 100 nm after spin coating with a PMMA A3 solution at 3000 rpm for 30 sec. Thinner PMMA buffer

layers (thickness $\approx$ 7 nm) were formed by increasing the spin speed to 6000 rpm and diluting the PMMA A3 solution with anisole. None of the post-deposited ATO layers cracked on these thin PMMA buffer layers after the 500 °C heating process, and no significant degradation was noted in the conductivity.
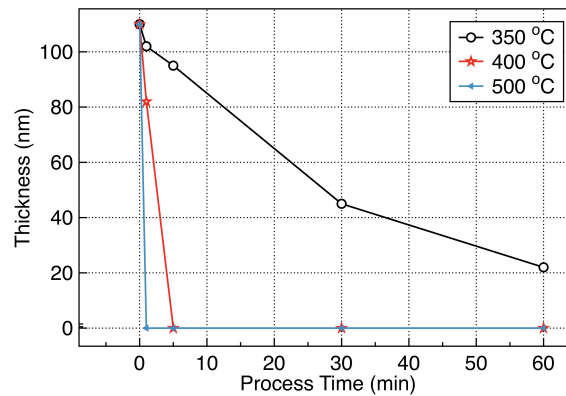
(a)
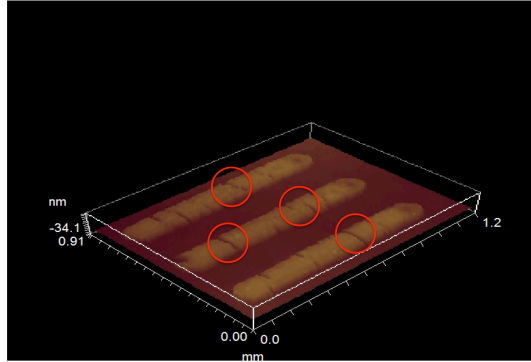
(b)
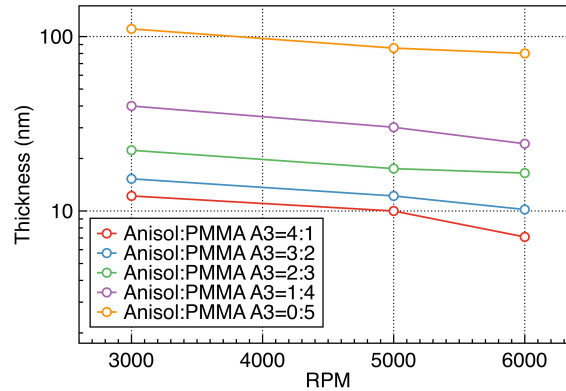
(c)

Figure 4.20 (a) The WYKO image of the cracked printed ATO electrodes, after finishing heating process at 500ºC for 15 mins. (b) Deposited PMMA layer thickness, corresponding to spin-coating RPM. (c) The measured thickness of PMMA layer during heating process at different temperature and process time.

The printed ATO line morphology was investigated. Figure 4.21 depicts the printed ATO lines on 5-min UV/Ozone-treated thin PMMA layers. At 50 °C and 70 °C, a valley appears in the middle of the lines when the drop spacing (D) is 20 μm. However, for D values of 30 and 40 μm, spikes formed on the surface. At 110 °C, each droplet was individually dried, resulting in the wavy structure. As the drop spacing decreased, the overlapped area increased, reducing the wave height of the ATO lines from 6 nm to 2 nm. The ATO electrode thickness was ~50 nm and the width was ~100 μm under these conditions.
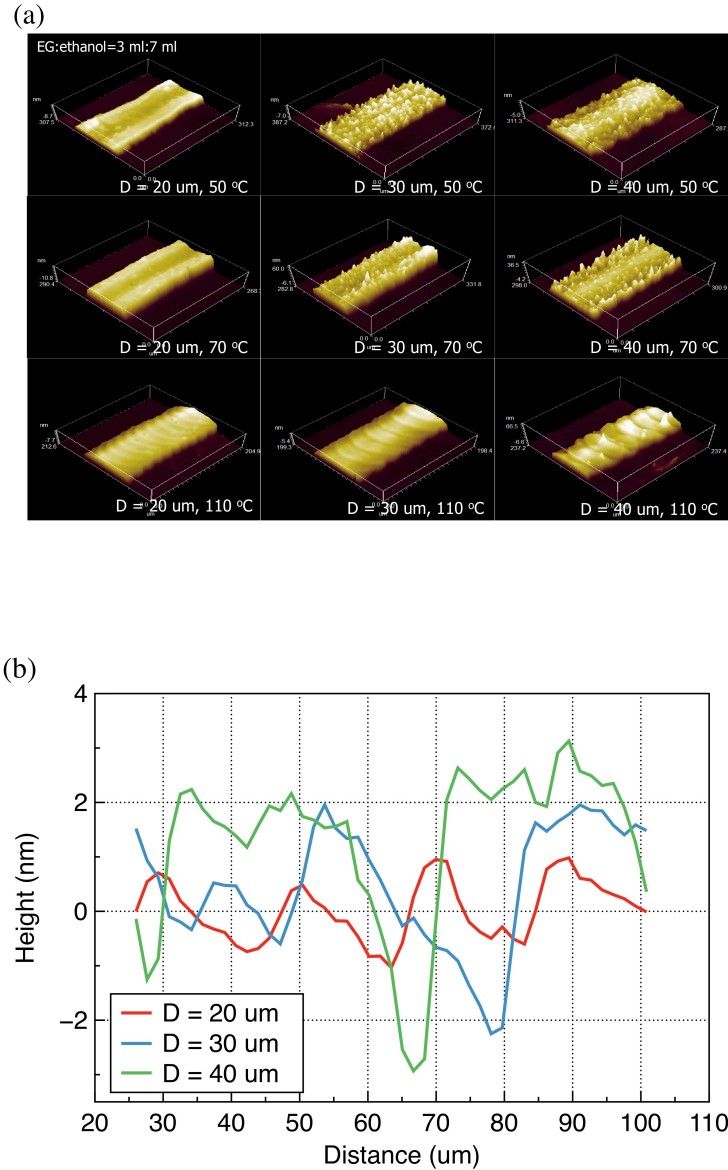
(a)

(b)

Figure 4.21 (a) The line morphology of printed ATO lines with different drop spacing and substrate temperature. (b) The surface profiles of ATO lines at 110 ᵒC.

92

## 4.4. Ink-jetted square ZrO$_2$ insulating films

In previous sections, to understand the movement of ink-jetted inks on substrates, we evaluated the figures of merit, such as the Weber, Ohnesorge and Reynold's numbers. Here, to begin, these values are extracted from the measured and extracted parameters from the ethanol and monoethanoline mixtures used to deposit ZrO$_2$ and summarized in table 4.3. The extracted physical parameters and evaluated Reynold, Weber, and Ohnesorge numbers are almost same as the extracted numbers for the ATO system.

Ethanol (ml)	MEA (ml)	Surface Tension (mN/m)	Viscosity (mPas)	Density (g/cm^3)	Velocity (m/sec)	Reynold	Weber	Ohnesorge	Z
10	0	21.8	1.20	0.79	5.6	110.5	34.1	0.0528	18.9
9	1	23.0	1.78	0.82	5.6	77.4	33.5	0.0748	13.4
7	3	26.0	3.35	0.88	5.6	44.1	31.8	0.1279	7.8
5	5	29.0	5.44	0.94	5.6	29.0	30.5	0.1902	5.3
0	10	48.9	19.10	1.11	5.6	9.7	21.2	0.4765	2.1

Table 4.3 Summary of physical properties and dimensionless numbers for each system.

Figure 4.22 shows the WYKO images and the cross-sectional profiles for the ink-jetted droplets of the ZrO$_2$ precursor inks with varying ratios of MEA to ethanol and with different substrate temperatures on the 5-min UV/ozone-treated thin PMMA buffer layers. The profiles indicate that the coffee-ring effect can be suppressed with an ink mixture containing 3 mL MEA and 7 mL ethanol at high substrate temperatures. As the ratio of MEA to ethanol increased, the viscosity of the ink also increased. In addition, the larger volume of MEA solvent became dominant when the jetted ink impinged the preheated substrates at 100 °C, which is above the boiling point of ethanol. Similar to the EG-ethanol system at high temperatures, the significant increase in the MEA viscosity and the increased contact angle decreased the spreading speed, minimized the outward flow related to the coffee-ring effect, and increased the minimum height of the central region of the droplet, originating from the impact inertia. Unlike the flat disk-shaped droplets obtained from the EG-ethanol system, when MEA was added to ethanol at 100 °C, perfectly dome-shaped droplets were obtained with no coffee-ring effect. In addition, the results of the two systems differed significantly in that ring-like residues appeared around the periphery of the main droplet. When the droplet impinged on the preheated substrate, truncated sphere shapes were initially formed. Then, the MEA, having a lower boiling

point than EG, dried faster and caused the thin rim to dry faster, leaving a gelled precursor on the heated substrates before the maximum spreading diameter could be reached, causing the formation of a flat disk shape like that formed with the EG-ethanol system. When the gelled precursor was on the rim, no liquid pressure remained to restrain the inward motion of the liquid in the outer rim.
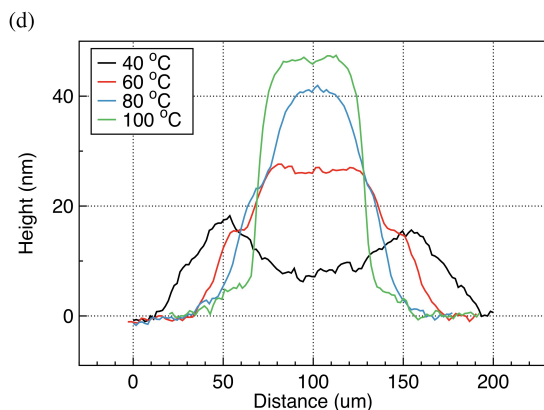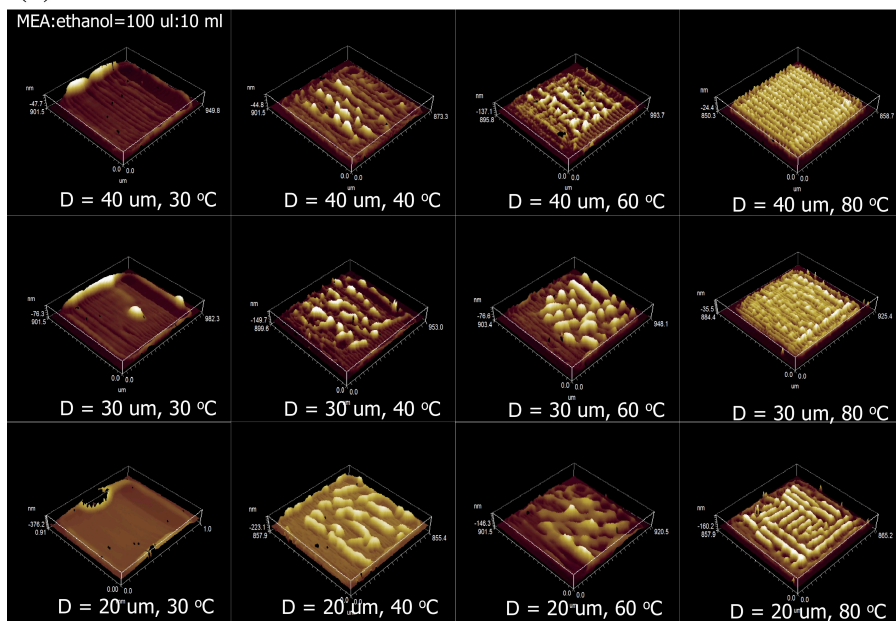
(a)

(b)

(c)

94

(d)
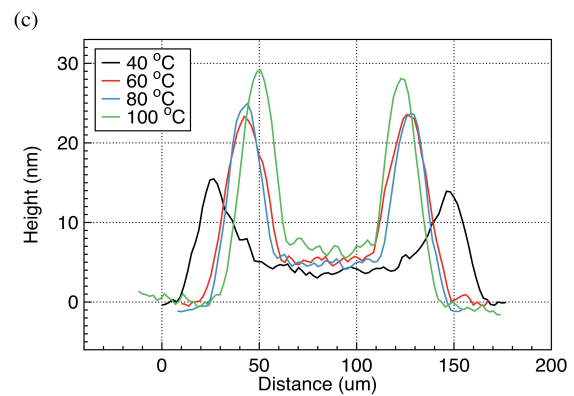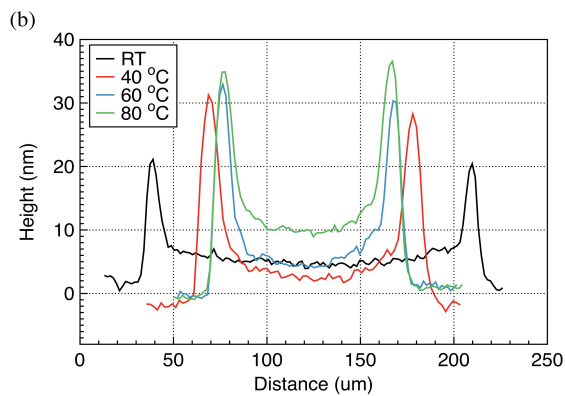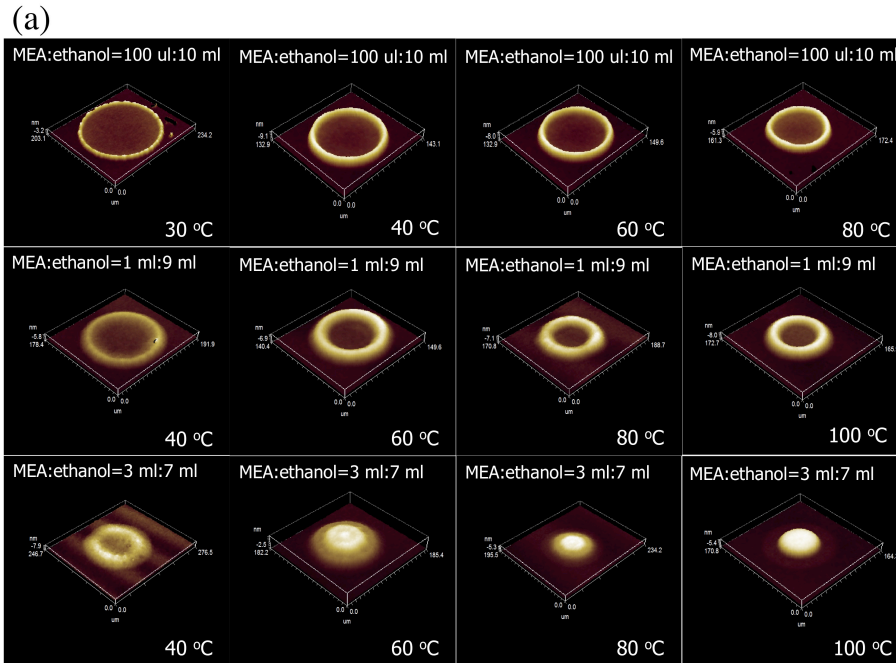
Figure 4.22 (a) WYKO images of ZrO$_2$ dots with different ratio of MEA to ethanol and at different substrate temperatures. (b) Cross sectional profiles for the mixture 100 ul MEA and 10 ml ethanol, (c) for the mixture 1 ml MEA and 9 ml ethanol, and (d) for the mixture 3 ml MEA and 7 ml ethanol, respectively.

To form square films via printing, the ZrO$_2$ precursor was ink-jetted onto UV/ozone-treated PMMA-coated glass substrates using a raster-scan technique with identical drop spacing in both the x and y directions and control over the drop spacing and substrate temperature. Figure 4.23 shows the typical behavior of printed square films created at different drop spacings (D) and substrate temperatures. We began with the reference ZrO$_2$ precursor solution (a liquid mixture of 100 μL MEA and 10 mL ethanol). At room temperature, the coffee-ring effect was noted when each droplet impinged on the substrates. Due to the velocity of the generated droplets, each droplet splashed upon impact. This result also occurred with the pure ethanol system for the ATO electrodes. When the identical second droplet impinged sequentially, it merged with the first droplet deposited. The second droplet also exhibited a concave structure. This merger altered the shape of the previously deposited droplet. The relatively thick edge wall of the first droplet collapsed below the overlapped region of the newly deposited second droplet leading to a continuous wavy line at the center. This line development continued until the last droplet was deposited. Finally, a single ZrO$_2$ line was formed, consisting of continuous concave droplets. After depositing the first line, a second line was formed on a portion of the first line. The sidewall of the first line, below the overlapped portion of the second line, collapsed and shifted to the left due to outward motion originating from the second line deposition. This process ultimately produced wrinkle-shaped square films. As the substrate temperature increased, each droplet dried faster, and its diameter decreased. At 80 °C, when the second droplet impinged upon the first deposited droplet, the first droplets did not move easily. The increased evaporation rate halted the movement of the ink earlier to yield a chainmail-shaped structure. With the liquid mixture of 1 mL MEA and 9 mL ethanol, the deposited droplet moved more freely at low temperatures due to the added MEA, which has a high boiling point and a low evaporation rate at 40 °C. During printing, the first deposited lines also shifted up and to the left due to outward motion originating from the second line deposition. This behavior
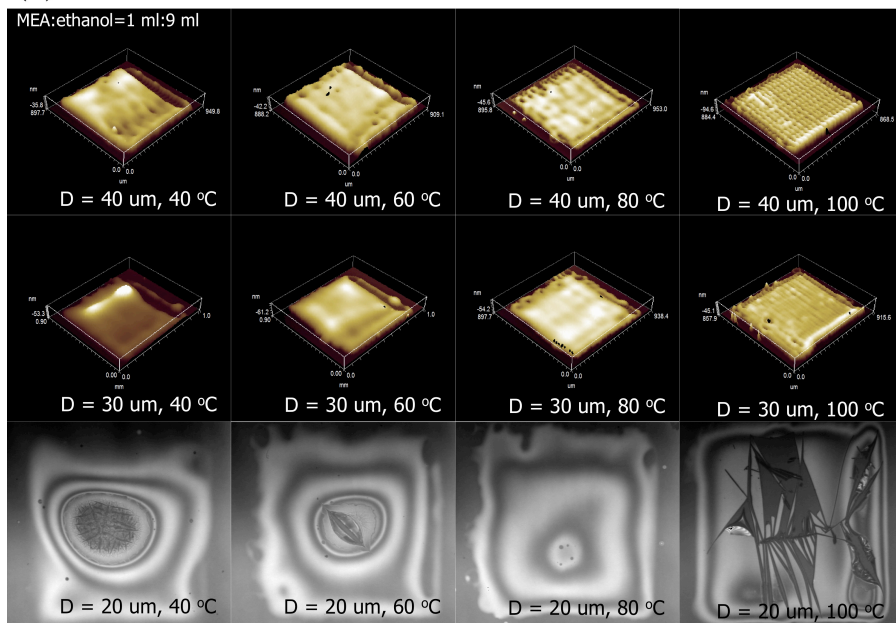
of inks continued until the last line was deposited. As a consequence, the top left of the square film is taller than the bottom right of the square films at low temperature. As the substrate temperature increased, the evaporation rate also increased. The first deposited lines dried faster and the lines are less affected by the aforementioned outward motion originating from the second line deposition. After completing the printing of the square film, more uniform square films were obtained. At 100 °C, each ink drop dried without additional flow because of the evaporation rate, and the boundaries of each droplet were obvious creating a chainmail-shaped structure. The liquid mixture of 3 mL MEA and 7 mL ethanol was also evaluated. At 40 °C, the higher boiling point of the MEA resulted in a reflow process and failed to form a uniform layer. At 60 °C, the restoring force of the surface tension dominated the inertial force; thus, the merged lines moved back into the direction of the line printing and dried, representing an intermediate oscillation stage prior to reaching a steady state. A hill formed near the end of the printing line. As the temperature increased, the movement of the ink was retarded due to the increased evaporation rate and reduced spreading speed, and the hill near the end of the printing line disappeared. At 80 °C, by suppressing the movement to the right edge through the increased evaporation rate, boundary-free and uniform square ZrO_2 films were formed (in Figure 4. 24). However, at 100 °C, each droplet dried individually, regardless of overlap, due to the high evaporation rate. No ink movement occurred at this stage. As a result, an array consisting of each dome-shaped droplet was formed on the substrates. When the distance between the droplets decreased, the volume per unit area increased, leading to an increase in the film thickness. The increased volume per unit area also decreased the evaporation rate and increased the drying time. A higher temperature was required to increase the evaporation rate and achieve the same conditions. For example, when the distance between the droplets was 30 μm at the same temperature, uniform layers were still obtained, not arrays in which each unit was a dome-shaped dot. The increased volume per unit area extended the drying time required to reach the evaporation-dominant phase. When the distance between droplets was 20 μm, the thickness of the square films also increased. Unfortunately, heating at 500 °C caused the deposited square ZrO_2 films to crack due to thermal stress, as depicted in Figure 4. 23 (b) and (c).

(a)

MEA:ethanol=100 ul:10 ml

D = 40 um, 30 °C   D = 40 um, 40 °C   D = 40 um, 60 °C   D = 40 um, 80 °C

D = 30 um, 30 °C   D = 30 um, 40 °C   D = 30 um, 60 °C   D = 30 um, 80 °C

D = 20 um, 30 °C   D = 20 um, 40 °C   D = 20 um, 60 °C   D = 20 um, 80 °C

(b)

MEA:ethanol=1 ml:9 ml

D = 40 um, 40 °C   D = 40 um, 60 °C   D = 40 um, 80 °C   D = 40 um, 100 °C

D = 30 um, 40 °C   D = 30 um, 60 °C   D = 30 um, 80 °C   D = 30 um, 100 °C

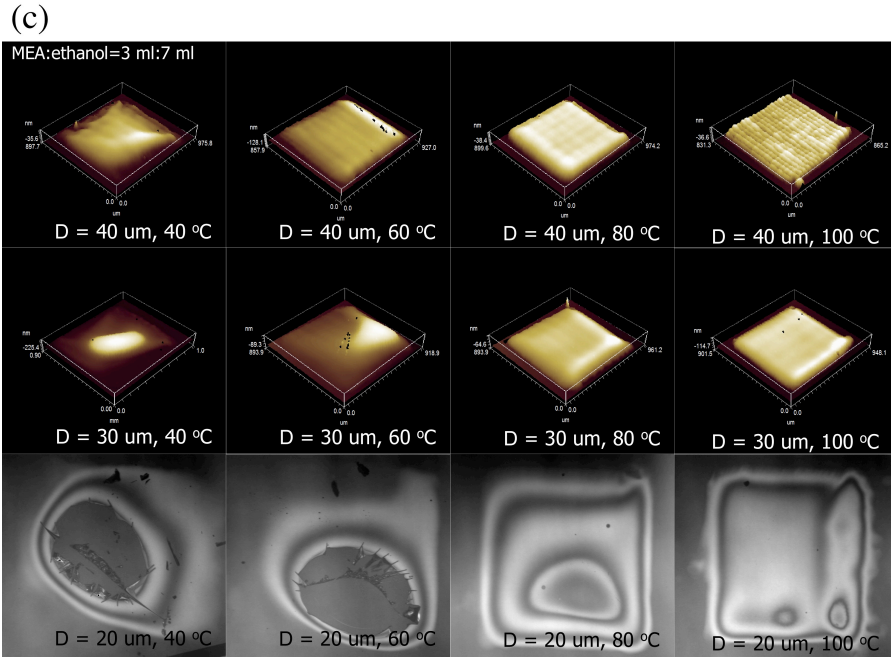D = 20 um, 40 °C   D = 20 um, 60 °C   D = 20 um, 80 °C   D = 20 um, 100 °C

97

(c)

Figure 4.23 WYKO images and optical images of square ZrO_2 films with differing ratios of MEA to ethanol, different drop spacing, D, and at different substrate temperatures. (a) Cross-sectional profiles for the mixture of 100 ul MEA and 10 ml ethanol, (b) for the mixture of 1 ml MEA and 9 ml ethanol, and (c) for the mixture of 3 ml MEA and 7 ml ethanol, respectively.
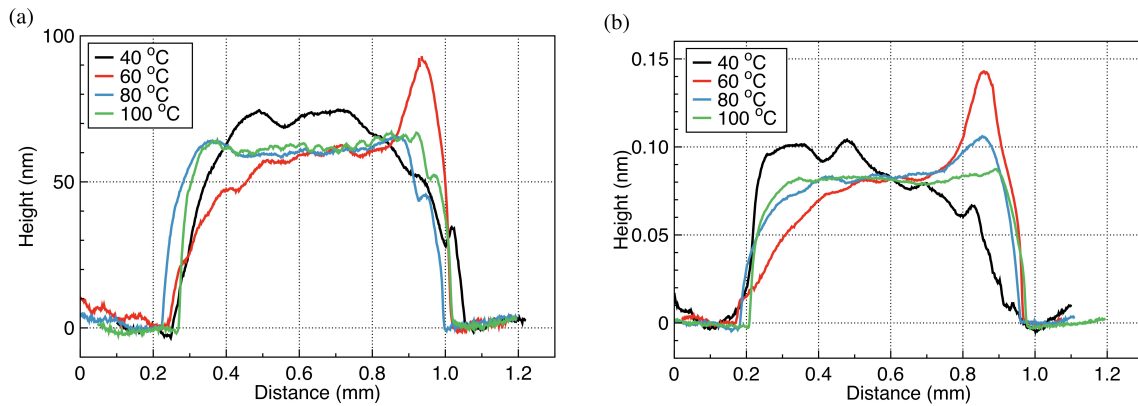

Figure 4.24 The cross sectional profiles of printed ZrO_2 square films on very thin PMMA layers, after a heating process with different substrate temperatures. (a) the liquid ink mixture of 1 ml EG and 9 ml ethanol and (b) the liquid ink mixture of 3 ml EG and 7 ml ethanol.

4.5. Electrical characteristics of printed ZrO_2 films

The electrical characteristics of sol-gel-processed ZrO_2 insulator films were investigated in Chapter 3. The electrical characteristics should be carefully estimated because in a sol-gel system, H_2O or OH groups in the films and other impurities produce electronic or ionic polarizations, which result in a frequency dependency of the dielectric constant [9], [10]. To evaluate the accurate field-effect mobility of the fabricated TFTs, the dielectric constant was extracted as a function of the frequency from the ITO/printed ZrO_2/Au structures with different sintering process times at 500°C in air. Figure 4.25 reveals the variation of the dielectric constant as a function of frequency. Obviously, the dielectric constant exhibited a clear decreasing trend with increasing frequency. The dielectric constant values increased by 1.5-fold at 50 Hz and remained relatively constant at frequencies above 10 kHz. However, compared to the five-layer spin-cast ZrO_2 films discussed in the previous chapter, the dispersion of the dielectric constant was insignificant at 500°C regardless of the sintering process time. Figure 4.25(b) presents the current density versus the electric field curves as a function of the sintering process time at 500°C in air. The current density did not change considerably after 1 h of sintering at a low electric field, which corresponds to the operation voltage of the fabricated TFTs; however, the current density in the high-electric-field regime was one order lower of magnitude than those of the 30 and 45 min cases.
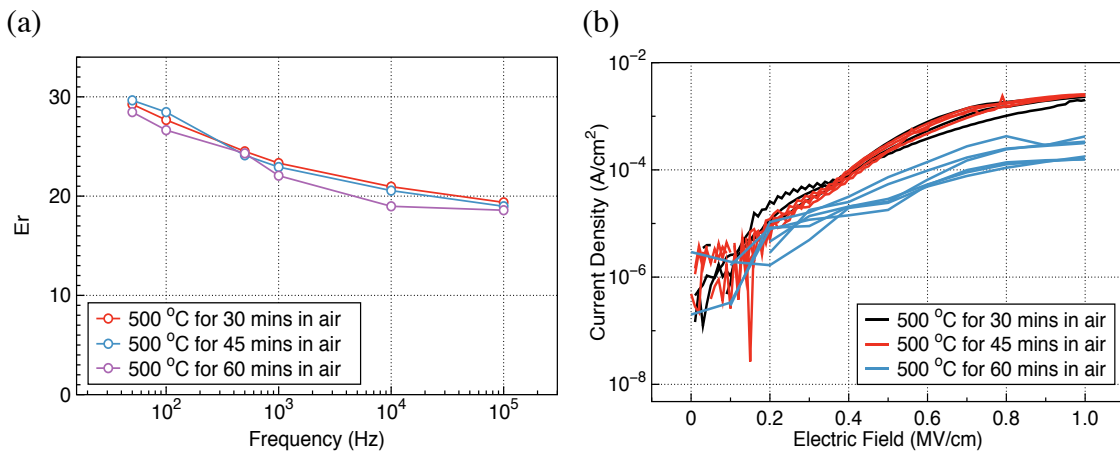
(a)   (b)

Figure 4.25 (a) Variance of a dielectric constant of printed ZrO_2 films at 500°C in air with different sintering process times. (b) Current density versus electric field curves of the printed ZrO_2 films as a function of the sintering process time.

4.6. All inkjet-printed SnO_2/ZrO_2 transistors
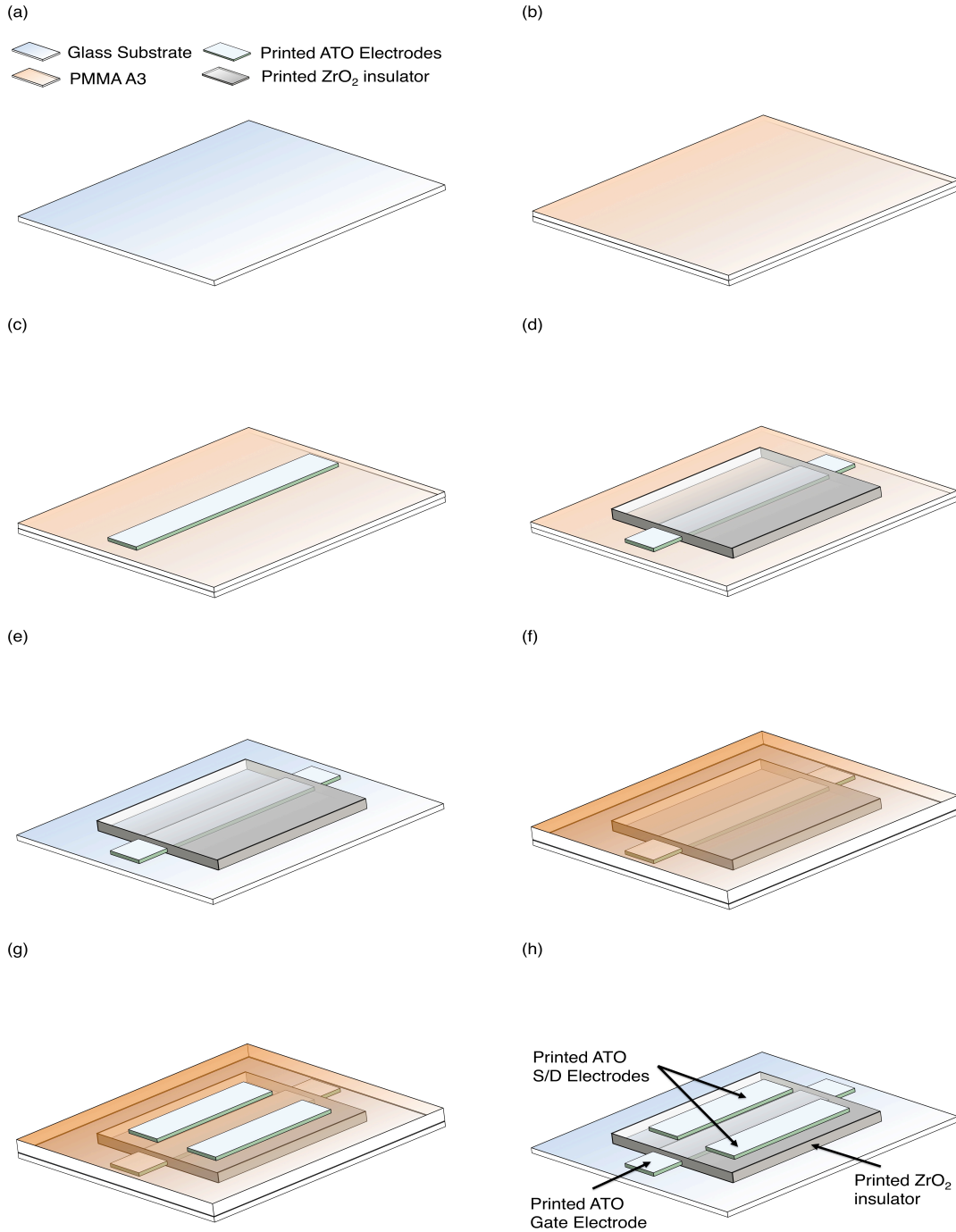
Figure 4.26 The fabrication flow of fully ink-jetted TFTs. (a) glass substrates. (b) PMMA buffer layers on the glass substrates. (c) and (d) printed ATO gate electrode and printed ZrO2 insulator on ATO gate electrode. (e) sintering process for conversion and removal of PMMA buffer layers. (f) second PMMA buffer layers. (g) printed coffee ring less source and grain ATO electrodes. (h) sintering process to make conductive ATO electrodes and remove the second PMMA buffer layer.

Figure 4.26 shows the fabrication flow of fully ink-jetted TFTs. Based on the aforementioned optimized conditions, uniform ATO electrodes for use as bottom-gate electrodes and uniform square ZrO_2 films on top of the ATO electrodes were fabricated on thin PMMA layers. After an 1 hour sintering process at 500 ℃ in air, second PMMA buffer layers were deposited on the ZrO_2 films to facilitate the formation of coffee ring less ATO source and drain electrodes. To make conductive ATO electrodes and remove the PMMA buffer layer, an additional sintering process was conducted at 500 ℃ for 15 mins in air. To increase the surface energy, a 5 mins UV/Ozone treatment was then used. Finally, the SnO_2 liquid phase precursors were ink-jetted on the previously formed ZrO_2 insulator layers between the source and drain electrodes. To convert into the SnO_2 semiconductor, a final sintering process was conducted at 400 ℃ for 5 mins in air. The cross-sectional profiles, optical images, and WYKO images of the fabricated TFTs and their electrical characteristics are presented in Figure 4.27. The fabricated TFTs exhibit conventional n-type TFT characteristics. To extract the mobility, the dielectric constant of ink-jetted ZrO_2 layer should be examined carefully. The dielectric constant exhibits an obvious decreasing trend with increasing frequency. Here, the dielectric constant value at low frequency (~50 Hz) was used to extract the mobility. The extracted mobility in saturation regime is 20 cm^2/Vs. The devices delivered an on/off current ratio of ~10^4 and a sub-threshold swing of 0.18 dec/V.
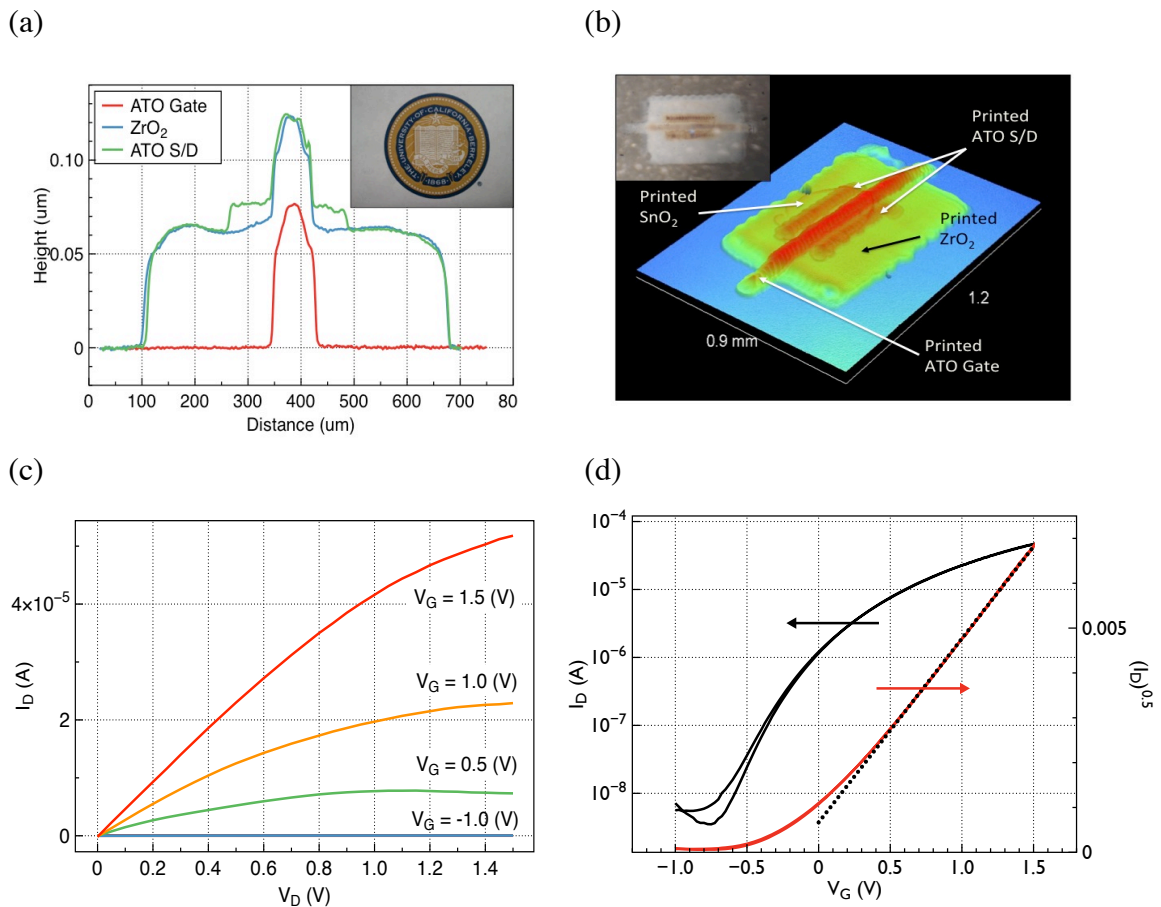
Figure 4.27 (a) The cross-sectional profiles of the fabricated TFTs. The inset shows the fabricated TFTs. (b) WYKO image of the TFT fabricated on glass substrates using a fully ink-jet printing system. The inset shows the optical image. Representative TFT characteristics: (b) I_d-V_d and (c) I_d-V_g (left axis) and $I_d^{0.5}$-V_g (right axis).

4.7. Summary

New approaches for fabricating fully inorganic TFTs via ink-jet printing were presented based on sol-gel processes. To produce all-printed electronics, stable jetting conditions must be established with the specific required condition to obtain uniform layers. A co-solvent system was employed to achieve these goals. We selected well-known chemical stabilizers in a sol-gel system, such as EG and MEA for use as high viscosity co-solvents. First, we started with low-viscosity major-phase solvents (ethanol dominant solvent) to generate stable single drops through inkjet printing. After impinging on the substrates, the major solvent was changed to a high-viscosity solvent (EG or MEA) with an increased boiling point (by raising the substrate temperature above the boiling point of ethanol) to prevent the coffee-ring effect. The remaining highly viscous solvent based inks reduced spreading speed on the more hydrophobic PMMA buffer layers and improved pattern definition as a result, including control of coffee ring formation. Based on these results, to produce uniform one- and two-dimensional layers, the drying time must be controlled to balance the dominance of the ink movement versus the drying process. To control drying time, the substrate temperature was controlled and the volume per unit area was varying by changing the drop spacing. For the first time, inorganic metal oxide-based TFTs were successfully fabricated on glass substrates using an all ink-jet printing system. The devices demonstrated a saturation mobility of 20 cm^{2}V^{-1}s^{-1}, an on/off current ratio of 10^4, a sub-threshold swing of ~0.18 V/decade and an operating voltage of less than 1.5 V.

4.8. References

[1] C. Terrier, J. P. Chatelon, R. Berfoan, and J. A. Roger, "Sb-doped SnO$_2$ transparent conducting oxide from the sol-gel dip-coating technique", *Thin Solid Films*, vol. 263, pp. 37-41, 1995.g

[2] V. Müller, M. Rasp, G. Štefanić, J. Ba, S. Günther, J. Rathousky, M. Niederberger, and D. Fattakhove-Rohlfing, "Highly conducting nanosized monodispersed antimony-doped tin oxide particles synthesized via nonaqueous sol-gel procedure", *Chem. Mater.*, vol. 29, pp. 5229-5236, 2009.

[3] G. D. Martin, S. D. Hoath, I. M. Hutchings, "Inkjet printing: the physics of manipulating liquid jets and drops," *J. Phys. Conf. Ser.*, vol.105, pp.012001, 2008.

[4] J. E. Fromm, "Numerical calculation of the fluid dynamics of drop-on-demand jets," *IBM J. Res. Dev.*, vol. 23, pp. 322-333, 1984.

[5] N. Reis, and B. Derby, "Ink jet deposition of ceramic suspensions: modeling and experiments of droplet formation," *MRS Symp. Proc.*, vol. 624, pp. 64-70, 2000.

[6] S. Schiaffino, and A. A. Sonin, "Molten droplet deposition and solidification at low Weber numbers," Phys. Fluides, vol. 9, pp. 3172-3187, 1997.

[7] D. Pesach, and A. Marmur, "Marangoni effects in the spreading of liquid mixtures on a solid," *Langmuir*, vol. 3, pp. 519-524, 1987.

[8] J. A. Lim, W. H. Lee, H. S. Lee, J. H. Lee, Y. D. Park, K. Cho, "Self organization of ink-jet-printed triisolropylsilylethynyl pentacene via evaporation-induced flows in a drying droplet," *Adv. Funct. Mater.*, vol. 18, pp. 229-234, 2008.

[9] X. Ryu, M. Shen, S. Ge, Z. Gan, and W. Cao, "Dielectric enhancement of sol-gel drived $BaTiO_3/SrTiO_3$ multilayered thin films," *Thin Solid Films*, vol. 406, pp. 113-117, 2002.

[10] Z. Habibah, K. A. Yusof, L. N. Ismail, R. A. Baker, and M. Rusop, "Sol-gel derived nano-magnesium oxide: Influence of drying temperature to the dielectric layer properties," *IOP Conf. Series: Materials Science and Engineering*, vol. 46, pp. 012006, 2013.

Chapter 5 Conclusions and Future Work

5.1. Conclusions

Firstly, we demonstrated that SnO_2 semiconductors are novel candidates for transparent electronics. To form SnO_2 layers without using conventional vacuum-based equipment, a sol-gel process was adapted and successfully employed, forming SnO_2 layers on different substrates. The fabricated SnO_2-based TFTs on SiO_2 substrates revealed conventional n-type transistor behavior and delivered a field-effect mobility in the saturation regime of ~ 1.5 cm^2/Vs. By adding NH_4OH, the prepared precursor solution exhibited gel-like characteristics. With this precursor, SnO_2 films were successfully formed below 200 °C. Compared to the standard solution, the gel-like phase delivered test devices with a 3X boost in saturation mobility (~ 5.0 cm^2/Vs) and improved sub-threshold swing without any degradation in I_{on}/I_{off}.

For realization of a high-k insulator, sol-gel-processed ZrO_2 films were employed. To improve the electrical characteristic of ZrO_2, a detailed study on sintering conditions was performed. ZrO_2 films that were sintered at 450 °C for 2 h in air exhibited reduced gate leakage current, increased breakdown voltage, and reduced dielectric constant dispersion. Using this material within a TFT gate stack, SnO_2 TFTs were fabricated. SnO_2 TFTs on ZrO_2 insulators revealed promising TFT performance. The field-effect mobility in the saturation regime was approximately 30 cm^2/Vs. The on/off current ratio was approximately 10^3. Excellent characteristics were obtained at operating voltages below 1.5 V. Because of the high-k ZrO_2 dielectric layer, the active channel layer accumulated at rather low gate voltages, and the interface trap density between ZrO_2 and SnO_2 was significantly reduced, as indicated by the reduction of the subthreshold swing from 5 to 0.3 V/decade.

Finally, to realize all ink-jet printed TFTs, we selected a sol-gel process, using Sb-doped SnO_2 for transparent source, drain, and gate electrodes. After conducting a sintering process at 500 °C in air, conductive ATO films were formed. The extracted sheet resistance was sufficiently low to enable the deployment of this material as a printed transparent contact in printed TFTs. Under optimized conditions, stable drops were generated with the aforementioned liquid phase precursors for SnO_2, ZrO_2, and Sb-doped SnO_2. In addition, we also introduced, for the first time, a strategy to inkjet print uniform layers based on the sol-gel process. After the addition of high viscosity solvents, such as EG and MEA, and with increased substrate temperatures, coffee-ring effect-free and multilayer, stacked TFT structures were successfully fabricated on glass substrates. These techniques will be useful for other types of applications, such as solar cells or transparent electrochromic systems, which require uniform, multilayer, stacked structures. Based on these approaches, for the first time, inorganic metal oxide-based TFTs were successfully fabricated on glass substrates using an all-ink jet printed approach. The devices demonstrated a saturation mobility of 20 cm^{2}V^{-1}s^{-1}, an on/off current ratio of 10^4, a subthreshold swing of $\sim$0.18 V/decade, and an operating voltage of

less than 1.5 V.   These thus deliver a dramatic improvement in the state of the art of printed and transparent electronis.

5.2. Future work

Sol-gel processed SnO_2/ZrO_2 thin film transistors have been produced in previous studies, and fabricated TFTs have revealed promising TFT characteristics. However, various issues remain. The device characteristics of metal oxide-based TFTs are strongly affected by the operation temperature and ambient conditions. Under vacuum, as the operation temperature increases, the field effect mobility and drain current are increased due to the generation of thermally activated free electrons and oxygen vacancies, which increases the free carrier population inside the system. In air, absorbed oxygen molecules form energy barriers between grain boundaries, which lowers the drain current and field effect mobility simultaneously. To minimize the chemical reaction of the surface of metal oxide semiconductors, a passivation layer should be created, and the associated process should be optimized. Another approach is to dope the main semiconductor to improve the stability of the system. While this has been demonstrated in various systems, significant work remains to be done to make this viable in sol-gel SnO_2. In addition, further printing characterization, modeling, and optimization remains to be done to enable the realization of smoother and higher quality films for better interface quality between the semiconductor and insulator.

The dielectric constant of a sol-gel ZrO_2 layer exhibits an obvious decrease with increase in the frequency due to dispersive effects. Nevertheless, although high temperatures and long sintering processes reduce the dielectric constant dispersion, frequency dependencies are still observed. An increase in the dielectric constant is determined by the polarization of the materials. In a sol-gel system, H_2O or OH groups in the films and other impurities result in electronic or ionic polarization, which results in a similar frequency dependency. To solve this issue, a longer process at higher temperature is proposed. Second, the sintering process should be conducted in O_2 to minimize these effects, or additional O_2 plasma or UV/Ozone processes are used to reduce the effects of uncombined metal anions.

Nevertheless, fabricated TFTs show promising DC TFT performance. Specifically, AC characteristics are also important to achieve integrated circuits. To improve AC performance, significant structural optimization and scaling remains to be performed. Channel length scaling should be pursued in this regard. In addition, the overlap area should be minimized. Second, further materials optimization to improve field effect mobility values is required.

When the channel length decreases, contact resistance factors should dominate; thus, we must select more conductive, Schottky barrier less materials. In this SnO_2/ZrO_2 system, Al electrodes (smaller work function) lead to better DC and AC TFT performance, compared to Au electrodes, which were used in herein. For inkjet-printed

systems, the aforementioned issues should also be considered. Ideally, ink-jet printed TFTs with a channel length of 1~2 um can be fabricated using state of the art printers. Unfortunately, the minimum width of the printed-ATO gate electrodes is approximately 100 um, resulting in significant overlap area between the gate and source/drain electrodes. To reduce the overlap area, narrower gate electrodes are required. To solve this issue, the volume of the drops can be reduced, resulting in the formation of more small and narrow features. Second, more conductive electrodes are required as well. Compared to metal electrodes, metal oxide electrodes such as ITOs, ATOs, and FTOs have larger resistivity and can more significantly degrade the performance of TFTs with shorter channel lengths.

Herein, promising semiconductor and insulator materials are described. Additionally, new strategies were introduced to realize all inkjet printed transistors. Uniform one- and two-dimensional films were formed with liquid phase sol-gel precursors by changing the primary solvent to one with a high viscosity and increasing the substrate temperature to reduce the movement of drops. Based on this strategy, fully printed TFTs without coffee rings were produced using inorganic solution based sol-gel precursor inks. As future work, the various issues identified above must be solved in order to produce stable and high performance TFTs.